

A Phase Field Model for the Evolution of Martensite Microstructures in Metastable Austenites

vom Fachbereich Maschinenbau und Verfahrenstechnik
der Technischen Universität Kaiserslautern
zur Verleihung des akademischen Grades
Doktor-Ingenieur (Dr.-Ing.)
genehmigte Dissertation

von
Dipl.-Ing. Regina Müller
aus Würzburg

Hauptreferent: Prof. Dr.-Ing. Ralf Müller
Korreferent: Jun.-Prof. Dr.-Ing. Marc-André Keip
Vorsitzender: Prof. Dr.-Ing. Eberhard Kerscher
Dekan: Prof. Dr.-Ing. Jörg Seewig

Tag der Einreichung: 26.08.2015
Tag der mündlichen Prüfung: 15.07.2016

Kaiserslautern, 2016

D 386

Herausgeber

Lehrstuhl für Technische Mechanik
Technische Universität Kaiserslautern
Gottlieb-Daimler-Straße
Postfach 3049
67653 Kaiserslautern

© Regina Müller

Ich danke der „Prof. Dr. Hans Georg und Liselotte Hahn Stiftung“ für die finanzielle Unterstützung bei der Drucklegung.

Druck

Technische Universität Kaiserslautern
Hauptabteilung 5/ Bau-Technik-Energie
Abteilung 5.6 Foto-Repro-Druck

Alle Rechte vorbehalten, auch das des auszugsweisen Nachdrucks, der auszugsweisen oder vollständigen Wiedergabe (Photographie, Mikroskopie), der Speicherung in Datenverarbeitungsanlagen und das der Übersetzung.

ISBN 978-3-942695-13-8

Vorwort

Die vorliegende Arbeit entstand während meiner Tätigkeit als wissenschaftliche Mitarbeiterin am Lehrstuhl für Technische Mechanik an der Technischen Universität Kaiserslautern.

An erster Stelle gilt mein besonderer Dank Herrn Prof. Dr.-Ing. Ralf Müller für die in jeder Hinsicht hervorragende Betreuung und Unterstützung, die entscheidend zum Gelingen dieser Arbeit beigetragen haben. Ich danke Herrn Jun.-Prof. Dr.-Ing. Marc-André Keip für die bereitwillige Übernahme des Korreferates und das damit verbundene Interesse an meiner Arbeit. Weiterhin bedanke ich mich bei Herrn Prof. Dr.-Ing. Eberhard Kerscher für die Übernahme des Vorsitzes.

Furthermore, I am very grateful to Prof. Kaushik Bhattacharya for his interest in my research and the fruitful discussions during my research visit at California Institute of Technology in Pasadena.

Meinen Kollegen am Lehrstuhl danke ich für die sehr angenehme und freundschaftliche Arbeitsatmosphäre sowie nicht nur fachliche Unterstützung bei so manchen Herausforderungen. Besonders hervorheben möchte ich meine Bürokollegin Frau Jun.-Prof. Dr.-Ing. Charlotte Kuhn, die mir wissenschaftlich mit Rat und Tat zur Seite stand und zusätzlich noch für den sportlichen Ausgleich im Lehrstuhl-Alltag sorgte.

Schließlich bedanke ich mich bei meinen Eltern und meinem Mann Georg für die bedingungslose Unterstützung, die unerschöpfliche Geduld und das unglaubliche Verständnis.

Würzburg, August 2016

Regina Müller

Zusammenfassung

Viele technisch relevante metallische Werkstoffe besitzen eine heterogene Mikrostruktur. Das makroskopische Materialverhalten ist das Resultat des Zusammenwirkens einer Vielzahl von Phasen und Strukturen, mit jeweils unterschiedlichen mechanischen Eigenschaften. Insbesondere die Gefügeentwicklung in metastabilen austenitischen Stählen unterliegt dem Einfluss verschiedener Mechanismen. In diesem Zusammenhang ist die martensitische Transformation hervorzuheben, bei der das Kristallgitter ausgehend von der metastabilen kubisch-flächenzentrierten austenitischen Phase in den kubisch-raumzentrierten Martensit, die stabile Phase, umklappt. Durch die Phasenumwandlung kommt es zu einer Volumenänderung sowie einer Gitterscherung, was zu einer Eigen- oder Transformationsverzerrung innerhalb des Martensits führt. Abhängig von der Richtung der Gitterscherung entstehen unterschiedliche martensitische Orientierungsvarianten, die sich in einer komplexen Mikrostruktur anordnen. Der Martensit wächst meist nadel- oder plattenförmig, wobei ein autokatalytischer Effekt beobachtet wird, d. h. eine Martensitplatte das Wachstum weiterer Platten induziert. Zusätzlich führt die Eigendehnung im Martensit auf der atomaren Skala zu einem Wandern von Versetzungen, die wiederum die Phasentransformation beeinflussen. Kontinuumsmechanisch werden solche Versetzungswanderungen als Plastizität erfasst. Darüber hinaus entstehen im austenitischen Stahl Mikrorisse die ebenfalls mit der martensitischen Transformation wechselwirken. In diesem Zusammenhang ist im Experiment die Bildung von Martensit an der Risspitze zu beobachten. Da der Martensit andere Materialeigenschaften als der Austenit aufweist, wirkt sich die Martensitbildung auf die Rissentwicklung aus.

Um zu einem besseren Verständnis der komplexen Zusammenhänge auf der Mikroebene von metastabilen austenitischen Stählen beizutragen, wird in dieser Arbeit ein Phasenfeldmodell für martensitische Transformationen vorgestellt. Das zweidimensionale Modell berücksichtigt zwei martensitische Orientierungsvarianten.

Im Rahmen des Phasenfeldansatzes gibt ein Ordnungsparameter die jeweils vorliegende Phase – Austenit oder Martensit – an. Im ersten Teil der vorliegenden Arbeit wird rein elastisches Materialverhalten angenommen. Die Kopplung der Materialeigenschaften an den Ordnungsparameter ermöglicht die Erfassung unterschiedlicher Werte für die verschiedenen Phasen. Zwischen den Phasen gewährleistet der Phasenfeldansatz einen stetigen Übergang der insbesondere für die numerische Umsetzung von Vorteil ist. Mit Hilfe von Kalibrierkonstanten wird

die Einstellung der Breite des Übergangsbereichs zwischen den Phasen mittels eines Modellparameters ermöglicht. Ein zweiter Modellparameter bestimmt die Grenzflächenenergie.

Die Metastabilität bzw. Stabilität des Systems wird durch ein Landaupolynom mit lokalen und globalen Minima modelliert, wobei die Koeffizienten des Polynoms die temperaturabhängige Energielandschaft festlegen. Im Rahmen dieser Arbeit werden zwei verschiedene Polynome vorgestellt die sich hinsichtlich der Berücksichtigung von zwei Martensitvarianten bezüglich des Ordnungsparameters unterscheiden. Ein Ansatz modelliert die beiden Varianten durch zwei Ordnungsparameter. Alternativ können die beiden Varianten mit einem einzelnen Ordnungsparameter modelliert werden, wenn das Polynom zwei geeignete globale Minima aufweist. Dieser Ansatz ist zwar betreffend der numerischen Umsetzung effizienter, führt allerdings bei der Mikrostrukturentwicklung zu Einschränkungen. Die Entwicklung der Mikrostruktur wird durch die Evolutionsgleichung des Ordnungsparameters beschrieben, wobei diesbezüglich von einer zeitabhängigen Ginzburg-Landau-Gleichung ausgegangen wird.

Um weitere Einflüsse auf die martensitische Transformation zu untersuchen, wird das elastische Phasenfeldmodell erweitert. Zunächst wird Versetzungswanderung im Rahmen der Kristallplastizität berücksichtigt. Dadurch können für die verschiedenen Phasen unterschiedliche Gleitsysteme verwendet werden. In einer zweiten Erweiterung erfolgt die Kopplung des bestehenden elastischen Modells an ein Phasenfeldmodell für Bruch. Hierbei erfolgt die Beschreibung des Rissfelds mittels einer Schädigungsvariablen, deren Entwicklung ebenso durch eine zeitabhängige Ginzburg-Landau-Gleichung beschrieben wird. Da es aufgrund der martensitischen Eigendehnung trotz einer globalen Zugbelastung zu lokalen Druckspannungen kommt, wird das Vorzeichen der lokalen Volumenänderung berücksichtigt. Auf diese Weise kann ein physikalisches Verhalten eines Risses unter Druckbelastung erreicht werden. Zusätzlich wird die Irreversibilität des Risswachstums modelliert.

Das Modell ist in das Finite Elemente Programm *FEAP* (*Finite Element Analysis Program*) implementiert. Bei mechanischen Finite-Elemente-Problemen werden die Einträge des Verschiebungsvektors als Knotenfreiheitsgrade erfasst. Für den Phasenfeldansatz wird neben den Verschiebungen zusätzlich der Ordnungsparameter als Knotenfreiheitsgrad berücksichtigt, sodass in jedem Knotenpunkt die vorliegende Phase berechnet wird. Zu den gekoppelten, nicht-linearen Feldgleichungen zählt neben der Evolutionsgleichung des Ordnungsparameters die Gleichgewichtsbedingung. Für die numerische Implementierung wird die jeweils schwache Form der Feldgleichungen diskretisiert. Die Lösung des Gleichungssystems erfolgt mit Hilfe des Newton-Raphson-Verfahrens, das eine Linearisierung der Gleichungen erfordert. Die Zeitabhängigkeit der Problemstellung benötigt eine Zeitintegration, die implizit mittels des Euler-Rückwärts-Verfahrens durchgeführt wird. Bezüglich

der Kristallplastizität erfolgt die Zeitintegration auf verschiedenen Ebenen: Die Lösung des Gleichungssystems und damit die Entwicklung des Ordnungsparameters als Knotenfreiheitsgrad finden global statt, während die Evolutionsgleichungen der Kristallplastizität am Integrationspunkt auf der Elementebene in Form eines Prädiktor-Korrektor-Verfahrens integriert werden.

Zunächst wird eine Kalibrierung des Finite-Elemente-Modells durch atomistische Simulationen vorgenommen. Diese stellen für reines Eisen bei einer Temperatur von $T = 100 \text{ K}$ sämtliche Materialparameter bereit. Anschließend erfolgt eine Validierung der Werte bei $T = 1300 \text{ K}$. Im nächsten Schritt wird mit Hilfe der Finite-Elemente-Simulationen der Einfluss der Volumenänderung sowie der Berücksichtigung mehrerer Orientierungsvarianten für austenitische Stähle analysiert. Diesbezüglich führt alleine die martensitische Eigendehnung zu einer Wanderung der Grenzfläche. Weiterhin lösen äußere mechanische Lasten die martensitische Umwandlung aus. Mit Hilfe des Phasenfeldmodells wird die Entwicklung der martensitischen Phasen mit unterschiedlichen Eigendehnungstensoren untersucht, wobei in diesem Zusammenhang auch energetische Betrachtungen während des Keimvorgangs und der Ausbreitung des Martensits analysiert werden. Die Simulationsergebnisse zeigen in Übereinstimmung mit Experimenten plattenförmige martensitische Strukturen.

Im Anschluss werden im Rahmen der Kristallplastizität für die unterschiedlichen Phasen verschiedene Gleitsysteme berücksichtigt und so der Zusammenhang zwischen plastischen Dehnungen und der Phasentransformation untersucht. Dabei verursacht die Transformationsdehnung plastische Deformationen. Gleichzeitig lösen plastische Verformungen die martensitische Transformation aus. Motiviert durch den Fertigungsprozess des kryogenen Drehens von metastabilen Austeniten wird zusätzlich eine, mit einer Wanderlast beaufschlagte, Oberfläche kristallplastisch modelliert. Hier stellt sich heraus, dass plastische Deformationen von der austenitischen an die martensitische Phase vererbt werden. Außerdem kann der autokatalytische Effekt, der im Zusammenhang mit der Bildung von martensitischen Platten beobachtet wird, mit plastischen Verformungen in Verbindung gebracht werden. Eine qualitative und quantitative Übereinstimmung der Simulationsergebnisse mit experimentellen Proben ist gegeben.

Um abschließend die Wechselwirkungen der martensitischen Transformation mit Rissen auf der Mikroebene zu analysieren, wird das vorgestellte Phasenfeldmodell für martensitische Transformationen mit einem Phasenfeldmodell für Bruch gekoppelt. Übereinstimmend mit experimentellen Beobachtungen bildet sich in den numerischen Simulationen Martensit an der Rissspitze und beeinflusst somit die Rissausbreitung. Gleichzeitig korrespondieren die Charakteristika der Simulationsergebnisse mit Mikroskopaufnahmen einer martensitischen Struktur. Sowohl bei der experimentellen als auch der berechneten Mikrostruktur treten

Risse ausschließlich im Martensit auf – entweder im Übergangsbereich zwischen den martensitischen Platten oder senkrecht zur Plattenrichtung.

Abstract

On the microlevel many metallic materials are composed of different structures with various mechanical properties, which affect the macroscopic mechanical behavior of the specimen. Especially the microstructure evolution of metastable austenitic steels is subjected to the influence of several phenomena. One important structural change is the martensitic transformation during which the crystal lattice changes from the metastable austenitic phase – with a face centered cubic lattice – to stable martensite with a body centered cubic lattice. The volume change and the lattice shear, which accompany the phase transition, lead to a transformation-induced eigenstrain or transformation strain within the martensitic phase. Depending on the lattice shear direction, different martensitic orientation variants arise which are combined to a complex microstructure. In experiments martensite is observed to grow in a lath- or plate-like shape in combination with an autocatalytic effect, i.e. one plate induces the formation of further martensitic plates. Additionally, the martensitic eigenstrain causes dislocation movement on the atomic scale, which also influences the evolution of phases. On the macroscale such a dislocation movement corresponds to plastic deformations. Moreover, microcracks are observed on the microlevel of austenitic steels interacting with the phase transformation. In this context martensite mainly forms at the crack tip, in turn affecting the crack path. In order to contribute to a better understanding of the complex formation of microstructure, in this thesis a two-dimensional phase field model for martensitic transformations, which considers two different martensitic orientation variants, is developed.

Within the phase field approach an order parameter is introduced to indicate whether the present phase is austenite or martensite. In the first part of the thesis an elastic material model is used while the different material properties of the phases are coupled to the order parameter. In this manner, the elastic properties can be considered individually for each phase. The order parameter interpolates smoothly between the phases, which is beneficial for the numerical implementation. By introducing calibration constants the width of the continuous transition zone between the phases can be controlled by a model parameter. With a second model parameter the interface energy is adjustable. The metastable and stable states of the system are modeled with help of a Landau polynomial, which has both local and global minima while the choice of the coefficients of the polynomial determines the temperature dependent energy landscape. In this thesis two different Landau polynomials are proposed to consider both martensite variants, differing in terms

of the order parameter. One approach takes two variants by two different order parameters into account. Alternatively, both variants can be considered by a single order parameter if the polynomial has two different global minima. Concerning the numerical implementation, the latter approach is more efficient. However, it imposes restrictions on the formation of the martensitic phase. Furthermore, the evolving microstructure is described by the evolution of the order parameter, which is assumed to follow the time-dependent Ginzburg-Landau equation.

The elastic phase field model is enhanced in two different ways to take further phenomena into account. First, dislocation movement is considered by a crystal plasticity setting. In this context, different slip systems for the different phases are included. Second, the elastic model for martensitic transformations is combined with a phase field model for fracture where a damage variable is related to fracture. In analogy to the order parameter, the evolution of the crack field is governed by a time-dependent Ginzburg-Landau equation. For this combined approach, there are some issues, which have to be considered. The eigenstrain within the martensite leads to both tensile and compressive loads. Therefore, the sign of the local volume change has to be taken into account to obtain physical results. In addition, to prevent the material from healing the irreversibility of a crack has to be ensured.

In order to perform numerical simulations the model is implemented into the finite element code *FEAP* (*Finite Element Analysis Program*). In a finite element scheme for mechanical problems, classically, the displacements are considered as nodal degrees of freedom. For the phase field approach, the order parameter is additionally taken as nodal degree of freedom, indicating the present phase in each nodal point. The set of non-linear coupled field equations is completed by the evolution equation(s) of the order parameter(s) and the equilibrium condition. For the numerical implementation, the weak forms of the field equations are discretized. Due to the non-linearity a Newton-Raphson scheme is applied to solve the system of equations, which requires a linearization of the equations. Additionally, integration in time is necessary to describe the temporal evolution of the microstructure. To ensure a robust performance the implicit Euler backward scheme is used. With regard to the time integration, special care has to be taken concerning the crystal plasticity setting. On the one hand, the order parameter evolves on a global level, where the system of equations is solved in each time step. On the other hand, there are evolution equations related to the crystal plastic material law, for which a backward Euler scheme in form of a predictor corrector method is applied on the element level at the integration point.

In a first step, the elastic finite element model is calibrated using atomistic simulations. Therefore, the parameters are identified by a molecular dynamics simulations for pure iron for the temperature $T = 100$ K and verified for

$T = 1300$ K. Subsequently, with the aid of numerical simulations the influence of the volume change and different orientation variants is investigated for considering the material data of austenitic steels. In this regard, the transformation-induced eigenstrain leads to interface motion without applying external loads. Furthermore, martensite is generated through defined mechanical loads acting on the metastable austenitic phase. By using the phase field model, the impact of a mechanical load history on the formation of the different martensitic phases with different transformation-induced eigenstrains is studied. In this context, the energy evolution during nucleation and growth of martensite is also considered. In the numerical simulations martensite is found to grow in a plate-like shape in accordance with experimental and other numerical studies.

In a next step the enhanced model with the crystal plasticity setting is employed. The relations between the phase transition and plastic deformations, which are calculated from the slip of different slip systems, are examined. The evolution of slip partially results from the transformation strain such that slip induced by the martensitic transformation is observed. On the other hand, the crystal plasticity also influences the formation of martensite. Furthermore, martensitic transformations in a crystal plastic material are studied at a loaded surface. The numerical setup is motivated by the process of cryogenic turning where due to the cooling the phase transition is triggered by the load of the turning tool. It turns out that the plastic deformations are inherited from austenite to martensite. Moreover, the resulting microstructure evolution reveals a link between the autocatalytic formation of martensitic plates and the plastic deformations. The simulation results qualitatively and quantitatively coincide with experimental observations.

Finally, with the aid of the combined phase field approach for martensitic transformations and damage the interactions between microcrack propagation and the formation of the martensitic phase are studied. Martensite forms in agreement with experimental observations at the crack tip and thus influences the crack formation. In addition, the main features of the numerical simulations are in accordance with micrographs of a martensitic structure, where the cracks arise exclusively in the martensite, either perpendicular to the martensitic plate direction or in the transition zone between the phases.

Contents

1	Introduction	1
1.1	Motivation and Background	1
1.2	Overview	2
2	Continuum Mechanics and Thermodynamics	5
2.1	Kinematics	5
2.2	Balance Equations	7
3	Martensitic Transformations	13
3.1	Characteristics of the Martensitic Transformation	13
3.2	Driving Mechanisms	16
4	An Elastic Phase Field Model for Martensitic Transformations	21
4.1	One-Dimensional Model	22
4.1.1	Motivation	22
4.1.2	Evolution Equation of the Order Parameter	23
4.1.3	Model Parameters	25
4.1.4	Interface Velocity	29
4.2	Phase Field Model for Multivariant Martensitic Transformations	31
4.2.1	Model Equations	32
4.2.2	Numerical Implementation	34
4.2.3	Input Parameters of Pure Iron from Atomistic Simulations	41
4.2.4	External Loads on a Two-Phase Beam	45
4.3	Metastable Austenites	46
4.3.1	Volumetric Eigenstrain and Orientation Variants	47
4.3.2	External Loads	52
5	An Enhanced Phase Field Model for Martensitic Transformations	59
5.1	An Alternative Separation Potential	59
5.2	Crystal Plasticity	65
5.2.1	Kinematics, Energetic Setting and Constitutive Laws	66
5.2.2	Local Time Integration Scheme	69
5.2.3	Numerical Examples	73
5.3	A Combined Phase Field Approach	86
5.3.1	Some Comments on Linear Elastic Fracture Mechanics	86
5.3.2	A Combined Phase Field Model	87
5.3.3	Numerical Examples	94

Contents

6	Conclusion and Outlook	99
6.1	Conclusion	99
6.2	Outlook	101
	Appendix A Derivatives Concerning the Numerical Implementation	105
	Bibliography	108

1 Introduction

1.1 Motivation and Background

In mechanical engineering the component surface is of particular importance. It strongly influences the component behavior since wear and cracks frequently initiate at the surface layer. Wear resistance and fatigue strength of a component are improved by a hardened surface. For ferrous metals this could be done by the martensitic transformation. Classically, the material is heated to obtain an austenitic crystal lattice. The subsequent cooling at a high cooling rate changes the crystal structure to the harder phase martensite. This surface treatment means an additional production step, which is costly, consuming time and energy. Alternatively, for sufficiently low temperatures, i.e. for temperatures below the martensite start temperature, the transformation from metastable austenite to stable martensite can also be triggered by plastic deformation of the specimen. This is exploited for manufacturing by cryogenic turning which motivates the present investigation. During the turning process the workpiece of metastable austenitic AISI 347 steel is cooled with carbon dioxide snow. In this way, the martensitic transformation is induced by the deformation of the turning tool at the component surface and surface hardening is obtained during the cutting. Hence, a single workstep results in the final shape of a workpiece including a hardened surface layer.

The turning at a cryogenic temperature induces different processes, which interact on the microscale of the material. First, there is the phase transformation from the face-centered cubic austenite to body-centered cubic martensite. The phase transition leads to a volume change and a lattice shearing, resulting in a transformation-induced eigenstrain within the martensitic phase. Depending on the shearing direction of the crystal lattice different orientation variants of martensite arise, which are combined to a complex microstructure. Furthermore, the martensitic transformation is accompanied by dislocation movement, which can be inherited from austenite to martensite. The plastic deformations lead to new nucleation sites for the martensitic phase, which results in an autocatalytic effect. Thus, plasticity plays a crucial role for the phase transformation. In addition, microcracks are observed on the microlevel of metastable austenites. In conjunction with the phase transformation, martensite mainly forms at the crack tip. This influences the crack propagation due to the eigenstrain acting in the martensite. On the other hand, the formation of the martensitic phase is affected by crack growth. The aim of this work is to contribute to a better understanding of these complex

1 Introduction

interactions with the aid of a numerical model.

Classically, a sharp interface between austenite and martensite is considered. This approach is applied e.g. by Cherkaoui et al. [1998], Cherkaoui and Berveiller [2000]. However, the tracking of those interfaces is numerically cumbersome. Alternatively, the phase field ansatz can be employed. Therein, an order parameter is introduced to indicate the present phase. The approach leads to a smooth transition zone between the phases. The properties of the phases are coupled to the order parameter such that these can be considered for each phase individually without dealing with discontinuities. The microstructure evolution is described by the evolution equation of the order parameter, which is known as the time-dependent Ginzburg-Landau equation. It is based on the thermodynamically consistent assumption that the rate of the order parameter is proportional to the variational derivative of the global free energy of the system with respect to the order parameter. A general overview on phase field modeling is given by Moelans et al. [2008] while Mamivand et al. [2013] provide a literature review of the past phase field modeling studies concerning the formation and growth of martensite. Chen et al. [1992], Wang and Khachaturyan [1997] introduced the first phase field models for martensitic transformations. These seminal works have been followed by many others, e.g. Artemev et al. [2000, 2001], Jin et al. [2001], Ahluwalia et al. [2004], Wang and Khachaturyan [2006], Zhang et al. [2007], Zhong and Zhu [2014]. In the following years enhanced models have been proposed. There are approaches which additionally consider dislocation dynamics e.g. Kundin et al. [2011] or plastic deformations, e.g. Guo et al. [2005], Richards et al. [2013]. All of them are based on Fourier transformation formalism. Yamanaka et al. [2008, 2009] use finite differences to solve the elasto-plastic field equations. For considering complicated boundary conditions or complex material laws, the finite element method is most effective. It is used, for example, by Levitas et al. [2010, 2013], Hildebrand and Miehe [2010, 2012], Roumi [2010], Yeddu et al. [2012], Malik et al. [2013].

1.2 Overview

In this thesis a phase field model for martensitic transformations is introduced which is implemented into the finite element code *FEAP* (*Finite Element Analysis Program*, Taylor [2014]). The order parameter is considered as additional nodal degree of freedom besides the mechanical displacements. The numerical realization of the phase field approach using finite elements is straightforward since the smooth transition zone circumvents dealing with discontinuities. Furthermore, the order parameter describes the distribution of the phases throughout the computation domain, so a laborious tracking of the interfaces is not necessary. With the aid of numerical simulations the single effects, which contribute to the microstructure formation, can be studied separately. In a first step the elastic field equations are

solved. Subsequently plastic deformations are taken into account within a crystal plasticity scheme. Finally, the interactions between the phase transformation and microcracks are studied by including a damage variable.

In particular, this work comprises of six chapters. Following the introduction, the most important continuum mechanical fundamentals, which are relevant for this thesis, are given in **Chapter 2**. These include the kinematic relations within the small strain context and the balance laws. Further simplifying assumptions are specified and the employed notation is introduced.

Chapter 3 summarizes the characteristics of the martensitic transformation. In this context also energetic considerations and driving mechanisms of the phase transition are taken into account.

In **Chapter 4** the phase field model for martensitic transformations is outlined. In the course of an initial motivation a one-dimensional model, including the model parameters, is presented. For the two-dimensional model the numerical implementation into a finite element scheme is discussed, followed by a parameter calibration, which uses information from atomistic simulations of pure iron. Additionally, the influence of the volume change during the phase transformation, the consideration of different martensite variants and external loads on the formation of the microstructure are investigated for metastable austenites.

Chapter 5 starts with the proposal of a numerically more efficient approach to consider different martensitic orientation variants. Subsequently, the model, which is introduced in Chapter 4, is enhanced such that plastic deformations can be taken into account by employing a crystal plasticity scheme. The numerical examples document the influence of the plastic deformations. Motivated by the process of cryogenic turning the phase transformation at a loaded surface is numerically studied and compared to experimentally obtained results. Finally, the model is combined with a phase field model for fracture, which allows a deeper insight into the interplay of martensitic transformations with damage.

The last **Chapter 6** concludes the thesis with a summary of the most important contributions. Additionally, open issues and future work are briefly discussed.

1 Introduction

2 Continuum Mechanics and Thermodynamics

In this chapter the basic relations concerning continuum mechanics and thermodynamics are presented. In the first section the concepts of kinematics describing the deformations of a material body are introduced while this work is limited to the geometrically linear theory. In Section 2.2 the balance equations for mass, momentum, angular momentum, energy and entropy are discussed so that eventually general constitutive equations can be deduced. Textbooks on this topic are e.g. Altenbach and Altenbach [1994], Gurtin et al. [2010], Haupt [2002], Holzapfel [2000], Becker and Gross [2002]. Furthermore, in Gross and Seelig [2007] an introduction with focus on fracture- and micromechanics is given.

2.1 Kinematics

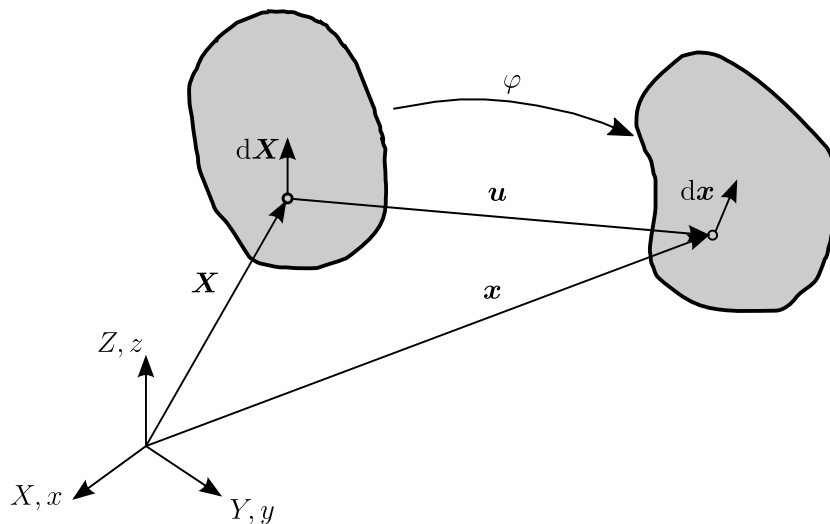


Figure 2.1: Deformation \mathbf{X} of a body \mathcal{B} .

The statements in this chapter refer to a *material body* \mathcal{B} with boundary $\partial\mathcal{B}$ in Euclidean space \mathbb{R}^3 , consisting of material points as shown in Figure 2.1. The spatial position of a *material point* χ in the *reference configuration* is given with \mathbf{X} . A *deformation* is described by the mapping $\mathbf{x} = \varphi(\mathbf{X}, t) : \mathcal{B} \rightarrow \mathbb{R}^3$ with $\mathbf{x}(\mathbf{X}, t)$

2 Continuum Mechanics and Thermodynamics

denoting the position of the material point χ in the *current* or *deformed configuration* for the time t . Below, \mathbf{X} is used to refer to the material point χ . The difference between the reference and the current configuration defines the *displacement vector*

$$\mathbf{u} = \mathbf{x} - \mathbf{X}. \quad (2.1)$$

The *velocity* of a material point is the material time derivative of \mathbf{x} (indicated by a superposed dot)

$$\mathbf{v} = \frac{d\mathbf{x}}{dt} = \frac{\partial \mathbf{x}(\mathbf{X}, t)}{\partial t} = \dot{\mathbf{x}}, \quad (2.2)$$

while the *acceleration* is defined to be the material time derivative of the velocity \mathbf{v}

$$\mathbf{a} = \frac{d\mathbf{v}}{dt} = \frac{\partial \mathbf{v}(\mathbf{X}, t)}{\partial t} = \dot{\mathbf{v}} = \ddot{\mathbf{x}} = \frac{d^2 \mathbf{x}}{dt^2}, \quad (2.3)$$

which is related to the local time derivative of \mathbf{v} with

$$\mathbf{a} = \frac{d}{dt} \mathbf{v}(\mathbf{x}(\mathbf{X}, t), t) = \frac{\partial \mathbf{v}(\mathbf{x}, t)}{\partial t} + \nabla \mathbf{v}(\mathbf{x}, t) \frac{\partial \mathbf{x}(\mathbf{X}, t)}{\partial t} = \frac{\partial \mathbf{v}}{\partial t} + (\nabla \mathbf{v}) \mathbf{v}. \quad (2.4)$$

The symbol $\nabla(\cdot)$ in Eq. (2.4) denotes the gradient $\text{grad}(\cdot)$. The *deformation gradient*

$$\mathbf{F} = \frac{\partial \varphi(\mathbf{X}, t)}{\partial \mathbf{X}} = \frac{\partial \mathbf{x}}{\partial \mathbf{X}} \quad (2.5)$$

is defined by the partial derivatives of a given deformation φ , i.e. \mathbf{F} is the Jacobian matrix of the mapping $\varphi(\mathbf{X}, t)$. In this work $\varphi(\mathbf{X}, t)$ is assumed to be invertible and orientation preserving leading to the non-vanishing determinant of the Jacobian

$$J = \det \mathbf{F} \neq 0. \quad (2.6)$$

Because the inverse \mathbf{F}^{-1} exists, the velocity gradient $\mathbf{L} = \nabla \dot{\mathbf{x}}$ is given by

$$\mathbf{L} = \dot{\mathbf{F}} \mathbf{F}^{-1}. \quad (2.7)$$

Using the deformation gradient \mathbf{F} and the displacement vector \mathbf{u} , the *displacement gradient* \mathbf{H} is written

$$\mathbf{F} = \frac{\partial \mathbf{x}}{\partial \mathbf{X}} = \frac{\partial (\mathbf{X} + \mathbf{u})}{\partial \mathbf{X}} = \mathbf{I} + \nabla \mathbf{u} = \mathbf{I} + \mathbf{H}, \quad (2.8)$$

where \mathbf{I} denotes the second order identity tensor. With the displacement gradient \mathbf{H}

a *line element* $d\mathbf{x}$ of the current configuration can be expressed as

$$d\mathbf{x} = d\mathbf{u} + d\mathbf{X} \quad (2.9)$$

$$= \frac{\partial \mathbf{u}}{\partial \mathbf{X}} d\mathbf{X} + d\mathbf{X} \quad (2.10)$$

$$= \mathbf{H} d\mathbf{X} + d\mathbf{X}. \quad (2.11)$$

For the definition of the strains the difference between the square of the line elements $ds^2 = d\mathbf{x} \cdot d\mathbf{x}$ and $dS^2 = d\mathbf{X} \cdot d\mathbf{X}$ is considered

$$ds^2 - dS^2 = [(\mathbf{H}d\mathbf{X} + d\mathbf{X}) \cdot (\mathbf{H}d\mathbf{X} + d\mathbf{X})] - d\mathbf{X} \cdot d\mathbf{X} \quad (2.12)$$

$$= d\mathbf{X}^T \cdot \underbrace{(\mathbf{H} + \mathbf{H}^T + \mathbf{H}^T \mathbf{H})}_{2\mathbf{E}} d\mathbf{X}. \quad (2.13)$$

The tensor $\mathbf{E} = \frac{1}{2}(\mathbf{H} + \mathbf{H}^T + \mathbf{H}^T \mathbf{H})$ denotes the *Green-Lagrange strain tensor* for finite strains. In this work only small displacement gradients with $|\mathbf{H}| \ll 1$ are considered. Thus, the third summand of \mathbf{E} is of higher order small and can be neglected, leading to the *linearized strain tensor*

$$\boldsymbol{\varepsilon} = \frac{1}{2}(\mathbf{H} + \mathbf{H}^T) = \frac{1}{2}(\boldsymbol{\nabla} \mathbf{u} + (\boldsymbol{\nabla} \mathbf{u})^T). \quad (2.14)$$

Within the geometrically linear small strain context, there is no distinction between reference and current configuration ($\mathbf{x} \rightarrow \mathbf{X}$).

The split of the linearized strain tensor into a *spherical* and a *deviatoric part* by

$$\boldsymbol{\varepsilon} = \underbrace{\frac{\text{tr}(\boldsymbol{\varepsilon})}{3} \mathbf{I}}_{\text{spherical part}} + \underbrace{\mathbf{e}}_{\text{deviatoric part}} \quad \text{with} \quad \mathbf{e} = \boldsymbol{\varepsilon} - \frac{\text{tr}(\boldsymbol{\varepsilon})}{3} \mathbf{I} \quad (2.15)$$

is for some problems beneficial. In the next step the balance equations are discussed.

2.2 Balance Equations

In this section the fundamental balance equations which are valid in continuum mechanics are introduced. Based on these, the use of the Coleman-Noll¹ procedure finally provides constitutive relations. For a start, the general form of a balance equation is given.

¹cf. Coleman and Noll [1963]

2 Continuum Mechanics and Thermodynamics

General Balance Equation

For the field quantity $\mathcal{V} = \int_{\mathcal{B}} \vartheta \, dv$ of a material body \mathcal{B} with outer normal vector \mathbf{n} along $\partial\mathcal{B}$, the *global form* of the *general balance equation*

$$\frac{d}{dt} \int_{\mathcal{B}} \vartheta \, dv = \int_{\partial\mathcal{B}} \boldsymbol{\ell}_{\vartheta}(\mathbf{x}, \mathbf{n}) \cdot \mathbf{n} \, da + \int_{\mathcal{B}} \rho_{\vartheta}(\mathbf{x}, t) \, dv + \int_{\mathcal{B}} \varsigma_{\vartheta}(\mathbf{x}, t) \, dv, \quad (2.16)$$

equates the temporal change of $\mathcal{V}(\mathbf{x}, t) = \int_{\mathcal{B}} \vartheta \, dv$ with the inward flux $\boldsymbol{\ell}_{\vartheta}$ of \mathcal{V} across the boundary $\partial\mathcal{B}$ per unit time and per unit boundary area $\partial\mathcal{B}$ in \mathbf{n} -direction, the production ρ_{ϑ} of \mathcal{V} in \mathcal{B} per unit time and per unit volume, and the supply ς_{ϑ} of \mathcal{V} in \mathcal{B} per unit time and per unit volume. Assuming ϑ to be continuously differentiable, the *Reynolds' transport theorem* is applied to the left-hand side of Eq. (2.16)

$$\frac{d}{dt} \int_{\mathcal{B}} \vartheta \, dv = \int_{\partial\mathcal{B}} \vartheta \mathbf{v} \cdot \mathbf{n} \, da + \int_{\mathcal{B}} \frac{\partial \vartheta}{\partial t} \, dv. \quad (2.17)$$

Converting the surface integrals results in the *local form* of the balance equation

$$\frac{\partial \vartheta}{\partial t} = \operatorname{div}(\boldsymbol{\ell}_{\vartheta} - \vartheta \mathbf{v}) + \rho_{\vartheta} + \varsigma_{\vartheta} \quad (2.18)$$

for each point \mathbf{x} of \mathcal{B} for all times.

Conservation of Mass

The *conservation of mass* is deduced from the general balance equation with $\mathcal{V} = m(\mathbf{x}, t) = \int_{\mathcal{B}} \rho \, dv$, where $\vartheta = \rho$ is the *mass density*. Assuming that the mass of a material volume does not change in time yields $\rho_{\rho} = \varsigma_{\rho} = 0$ and $\boldsymbol{\ell}_{\rho} = \mathbf{0}$ and the local form of mass balance is

$$\frac{\partial \rho}{\partial t} + \operatorname{div}(\rho \mathbf{v}) = \frac{d\rho}{dt} + \rho \operatorname{div} \mathbf{v} = 0. \quad (2.19)$$

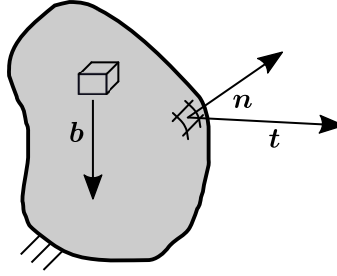
Linear Momentum Balance and Angular Momentum Balance

Considering the material body \mathcal{B} in Figure 2.2, subjected to the *surface traction vector* $\mathbf{t}(\mathbf{x}, \mathbf{n}, t)$ acting on the boundary $\partial\mathcal{B}$ and the *body force density* $\mathbf{b}(\mathbf{x}, t)$ per unit mass of \mathcal{B} , the *total linear momentum* is defined $\mathbf{L} = \mathcal{V} = m \mathbf{v} = \int_{\mathcal{B}} \rho \mathbf{v} \, dv$ and

Newton's second law reads

$$\frac{d}{dt} \int_{\mathcal{B}} \rho \mathbf{v} \, dv = \int_{\partial\mathcal{B}} \mathbf{t} \, da + \int_{\mathcal{B}} \rho \mathbf{b} \, dv, \quad (2.20)$$

which is the global form of the *linear momentum balance*. The linear momentum is


 Figure 2.2: Material body \mathcal{B} .

a vector quantity, which requires adapting the general quantities correspondingly. Comparing Eq. (2.20) with the general balance equation (2.16) in vector format identifies the flux density in \mathbf{n} -direction with $\mathbf{f}_{\rho v} \mathbf{n} \triangleq \mathbf{t}(\mathbf{x}, \mathbf{n}, t)$ and the supply density with the volume force $\mathfrak{s}_{\rho v} \triangleq \rho \mathbf{b}(\mathbf{x}, t)$. Since the linear momentum is a conserved quantity, the production density $\rho_{\rho v} = 0$. With use of *Cauchy's theorem*

$$\mathbf{t} = \boldsymbol{\sigma}^T \mathbf{n} \quad (2.21)$$

for the *Cauchy stress tensor* $\boldsymbol{\sigma}$, and the mass balance in Eq. (2.19), inserting the above densities in Eq. (2.18) in vector format yields the local form of the linear momentum balance

$$\rho \mathbf{a} = \operatorname{div} \boldsymbol{\sigma}^T + \rho \mathbf{b}. \quad (2.22)$$

In an analogous manner the local form of the *angular momentum balance* is derived, resulting in the symmetry of the Cauchy stress tensor

$$\boldsymbol{\sigma} = \boldsymbol{\sigma}^T. \quad (2.23)$$

With the acceleration \mathbf{a} assumed to be zero for all \mathbf{x} and in absence of volume forces, the linear momentum balance in Eq. (2.22) reduces with considering Eq. (2.23) to the *equilibrium condition*

$$\operatorname{div} \boldsymbol{\sigma} = \mathbf{0}. \quad (2.24)$$

Energy Balance - First Law of Thermodynamics

The *first law of thermodynamics* is the *balance of energy*, postulating the equivalence of the rate of *external mechanical* and *thermal work* to the change in total energy. The effect of other non-mechanical energies is neglected in this thesis. The total energy of a material body \mathcal{B} is composed of the *kinetic energy* $\int_{\mathcal{B}} \rho \frac{|\mathbf{v}|^2}{2} dv$ and the *internal energy* $\int_{\mathcal{B}} \rho u dv$ with the specific internal energy per unit mass u . A change of energy is effected by the energy supply, resulting from the mechanical part, which

2 Continuum Mechanics and Thermodynamics

is the power of the external forces

$$P = \int_{\partial\mathcal{B}} \mathbf{t} \cdot \mathbf{v} \, da + \int_{\mathcal{B}} \rho \mathbf{b} \cdot \mathbf{v} \, dv, \quad (2.25)$$

the heat supply $Q = \int_{\partial\mathcal{B}} \mathbf{q}_{\text{th}} \cdot \mathbf{n} \, da + \int_{\mathcal{B}} \rho r \, dv$ with the scalar heat radiation r , and the heat conduction \mathbf{q}_{th} , where a positive sign corresponds to heat supply across the boundary $\partial\mathcal{B}$, i.e.

$$\frac{d}{dt} \int_{\mathcal{B}} \left(\frac{|\mathbf{v}|^2}{2} + u \right) \rho \, dv = \int_{\partial\mathcal{B}} [(\boldsymbol{\sigma} \mathbf{n}) \cdot \mathbf{v} - \mathbf{q}_{\text{th}} \cdot \mathbf{n}] \, da + \int_{\mathcal{B}} (\rho \mathbf{b} \cdot \mathbf{v} + \rho r) \, dv. \quad (2.26)$$

The comparison of the global form of the energy balance in Eq. (2.26) with Eq. (2.16) yields for $\vartheta_e \triangleq \rho \frac{|\mathbf{v}|^2}{2} + \rho u$ the flux density in \mathbf{n} -direction $\boldsymbol{\ell}_e \cdot \mathbf{n} \triangleq \mathbf{q}_{\text{th}} \cdot \mathbf{n} + (\boldsymbol{\sigma} \mathbf{n}) \cdot \mathbf{v}$, the supply $\delta_{\vartheta} \triangleq \rho r + \rho \mathbf{b} \cdot \mathbf{v}$. Since the energy is a conserved quantity $p_e = 0$. Inserting these quantities in Eq. (2.18) results with the mass balance in Eq. (2.19), the linear momentum balance in Eq. (2.22), and the symmetry of $\boldsymbol{\sigma}$, in the local form of energy balance

$$\rho \frac{du}{dt} = -\text{div} \mathbf{q}_{\text{th}} + \boldsymbol{\sigma} : \nabla \mathbf{v} + \rho r. \quad (2.27)$$

Balance of Entropy - Second Law of Thermodynamics

The global form of the *balance of entropy* states the equivalence of the temporal change of entropy to the sum of the entropy supply and the entropy production. Using the following quantities, $\vartheta_s \triangleq \rho s$, where s is the *specific entropy* per unit mass; $\boldsymbol{\ell}_s \triangleq \phi_s$ is the entropy flux; $p_s \triangleq \rho p_s$, where p_s is the specific entropy production per unit mass; and $\delta_s \triangleq \rho z_s$, where z_s the specific entropy supply per unit mass, the local form of the entropy balance reads

$$\rho \frac{ds}{dt} = -\text{div} \phi_s + \rho (p_s + z_s). \quad (2.28)$$

The *second law of thermodynamics* postulates a non-negative entropy production, providing the entropy inequality

$$p_s \geq 0, \quad (2.29)$$

which has to be obeyed by every admissible thermodynamic process for each time t for all material points x . For thermodynamic processes close to equilibrium the entropy flux and the entropy supply can be approximated by

$$\phi_s = \frac{\mathbf{q}_{\text{th}}}{T} \quad \text{and} \quad z_s = \frac{r}{T}, \quad (2.30)$$

where T is an *absolute temperature*. Inserting these approximations together with the entropy balance in Eq. (2.28) into Eq. (2.29) results in the *Clausius-Duhem inequality*

$$\rho \frac{ds}{dt} + \operatorname{div} \frac{\mathbf{q}_{\text{th}}}{T} - \rho \frac{r}{T} = \rho p_s \geq 0, \quad (2.31)$$

which can be recast with the energy balance in Eq. (2.27) to

$$\rho (T\dot{s} - \dot{u}) - \frac{1}{T} \nabla T \cdot \mathbf{q}_{\text{th}} + \boldsymbol{\sigma} : \mathbf{L} \geq 0. \quad (2.32)$$

With the symmetry of the Cauchy stress tensor $\boldsymbol{\sigma}$ considered, the last term of Eq. (2.32) is within the small strain context equivalent to $\boldsymbol{\sigma} : \dot{\boldsymbol{\varepsilon}}$. Following the procedure proposed in Coleman and Noll [1963] and Coleman and Gurtin [1967], the introduction of the *Helmholtz free energy* per unit mass with

$$\psi^* = u - Ts, \quad \dot{\psi}^* = \dot{u} - \dot{T}s - T\dot{s}, \quad (2.33)$$

enables to rewrite Eq. (2.32) into

$$\boldsymbol{\sigma} : \dot{\boldsymbol{\varepsilon}} - \rho \left(\dot{\psi}^* + s\dot{T} \right) - \frac{1}{T} \mathbf{q}_{\text{th}} \cdot \nabla T \geq 0. \quad (2.34)$$

It is assumed that a material point \mathbf{x} is characterized by $\psi = \hat{\psi}(\boldsymbol{\varepsilon}, T)$, where $\psi = \rho \psi^*$ is the Helmholtz free energy per unit volume, leading to

$$\dot{\psi} = \frac{\partial \psi}{\partial \boldsymbol{\varepsilon}} : \dot{\boldsymbol{\varepsilon}} + \frac{\partial \psi}{\partial T} \dot{T}, \quad (2.35)$$

which is inserted into Eq. (2.34)

$$\left(\boldsymbol{\sigma} - \frac{\partial \psi}{\partial \boldsymbol{\varepsilon}} \right) : \dot{\boldsymbol{\varepsilon}} + \left(-\rho s - \frac{\partial \psi}{\partial T} \right) \dot{T} - \frac{1}{T} \mathbf{q}_{\text{th}} \cdot \nabla T \geq 0. \quad (2.36)$$

Since the inequality in Eq. (2.36) has to be fulfilled for all rates of $\boldsymbol{\varepsilon}$ and T the constitutive relations

$$\boldsymbol{\sigma} = \frac{\partial \psi}{\partial \boldsymbol{\varepsilon}} \quad \text{and} \quad -\rho s = \frac{\partial \psi}{\partial T} \quad (2.37)$$

can be deduced and the heat conduction inequality

$$\mathbf{q}_{\text{th}} \cdot \nabla T \leq 0 \quad (2.38)$$

remains which is e.g. satisfied by *Fourier's law* $\mathbf{q}_{\text{th}} = -\boldsymbol{\lambda} \nabla T$ with the symmetric, positive-definite conductivity tensor $\boldsymbol{\lambda}$.

In the following isothermal conditions are assumed, i.e.

$$\dot{T} = 0, \quad \nabla T = 0 \quad (2.39)$$

2 Continuum Mechanics and Thermodynamics

reducing the Clausius-Duhem inequality to

$$\boldsymbol{\sigma} : \dot{\boldsymbol{\varepsilon}} - \dot{\psi} \geq 0. \quad (2.40)$$

Coleman and Noll [1963] and Coleman and Gurtin [1967] exploit this in terms of internal variables, which is not in the focus of the present modeling and thus not discussed here.

3 Martensitic Transformations

In Chapter 2 the relations concerning continuum mechanics and thermodynamics are formulated for a material body without further specifications. Here, some thermodynamic aspects concerning the phase transition between austenite and martensite are given. Previously, the characteristics of the martensitic transformation are discussed. Textbooks on that topic are e.g. Porter and Easterling [1992], Pereloma and Edmonds [2012], Bhattacharya [2003] and Khachaturyan [2008]. On the microlevel of metastable austenitic steels, besides the phase transition also dislocation movement and microcracks are observed. At the end of this chapter some information on these competing mechanisms is given. In the context of the martensitic transformation also plastic deformations and damage are studied in this work.

3.1 Characteristics of the Martensitic Transformation

In metallurgy, any product of a diffusionless phase transformation is called *martensite*. A diffusionless transformation, where the movement of the atoms is less than the interatomic spacing, takes place when time is insufficient for a diffusion controlled process. The martensitic phase transition is an abrupt change of the crystal lattice which transforms, e.g. in austenitic stainless steels, from *face centered cubic* (fcc) austenite to *body centered cubic* (bcc) α' -martensite. The model introduced

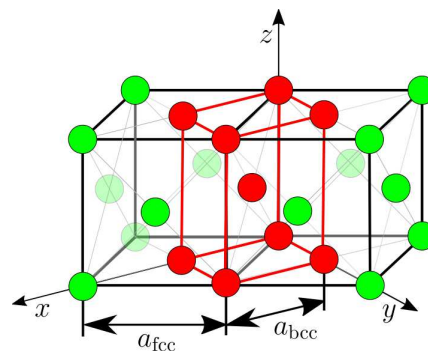


Figure 3.1: Schematic illustration of the Bain correspondence for martensite in steels.

by Bain [1924] intuitively visualizes this transition. Figure 3.1 schematically shows the *Bain correspondence*, where a preexisting bcc unit cell, marked in red, is defined within two austenitic fcc cells, marked in green. To obtain the martensitic bcc cell, a deformation of the preexisting bcc cell is necessary. Within the small strain context,

3 Martensitic Transformations

this deformation is described by the *Bain strain tensor* \mathbf{B} and can be derived from Figure 3.1 using the lattice parameters of austenite and martensite, a_{fcc} and a_{bcc} , respectively,

$$\mathbf{B} = \begin{bmatrix} \frac{a_{\text{bcc}} - \frac{a_{\text{fcc}}}{\sqrt{2}}}{\frac{a_{\text{fcc}}}{\sqrt{2}}} & 0 & 0 \\ 0 & \frac{a_{\text{bcc}} - \frac{a_{\text{fcc}}}{\sqrt{2}}}{\frac{a_{\text{fcc}}}{\sqrt{2}}} & 0 \\ 0 & 0 & \frac{a_{\text{bcc}} - a_{\text{fcc}}}{a_{\text{fcc}}} \end{bmatrix}. \quad (3.1)$$

The lattice mismatch between austenite and martensite leads to an *eigenstrain* within the martensitic phase, which is illustrated in Figure 3.2. A region of an austenitic continuum (depicted in green) is cut out. In this stress-free state, the region is undergoing a phase change according to the Bain strain or, more generally, the transformation strain or eigenstrain ϵ^0 , transforming the region into the martensitic phase (depicted in red). For reinserting the region into the austenitic continuum, its original shape is restored by applying stress. When the austenitic matrix with the martensitic inclusion is relaxed both matrix and inclusion are deformed. This reduces the elastic energy, which is introduced by the eigenstrain within the martensitic phase. Yet, after the relaxation there are still stresses acting in the continuum although no external load is applied.

An experimentally observed feature of the martensitic transformation is the presence of a *habit plane*, an undistorted and unrotated plane between the phases austenite and martensite, see e.g. Pereloma and Edmonds [2012], Zhang and Kelly [2009]. The habit plane is postulated by the phenomenological crystallographic theories on the martensitic transformation, which have been developed independently from each other by Wechsler et al. [1953], Bowles and Mackenzie [1954]. Mathematically speaking, this requires the transformation path to be described by an invariant plane transformation strain tensor ϵ^0 . Considering small deformations, for a given transformation strain tensor ϵ^0 with the principal strains or eigenvalues $\epsilon_I, \epsilon_{II}, \epsilon_{III}$ with $\epsilon_I \leq \epsilon_{II} \leq \epsilon_{III}$ and the eigenvectors e_I, e_{II}, e_{III} the invariant plane strain condition is

$$\epsilon_I \leq 0, \quad \epsilon_{II} = 0, \quad \epsilon_{III} \geq 0. \quad (3.2)$$

If Eq. (3.2) is satisfied by the transformation strain tensor ϵ^0 , there are two invariant planes with the normal vectors

$$\mathbf{n}_{+/-}^\epsilon = \pm \frac{\sqrt{-\epsilon_I}}{\sqrt{2(\epsilon_{III} - \epsilon_I)}} \mathbf{e}_I + \frac{\sqrt{\epsilon_{III}}}{\sqrt{2(\epsilon_{III} - \epsilon_I)}} \mathbf{e}_{III}. \quad (3.3)$$

3.1 Characteristics of the Martensitic Transformation

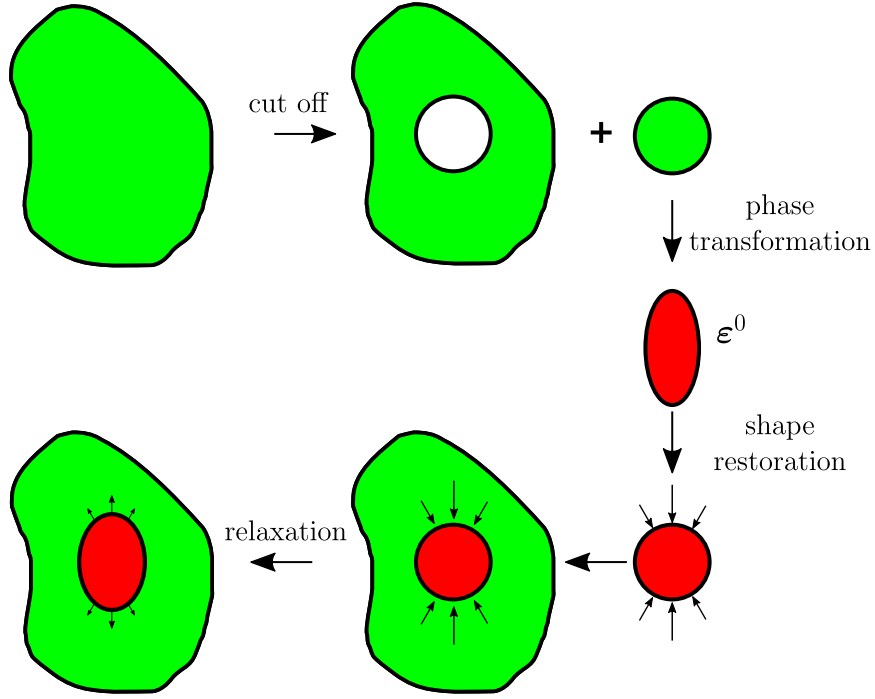


Figure 3.2: The lattice mismatch leads to an eigenstrain within the martensitic phase, Khachaturyan [2008].

The vectors $\mathbf{n}_{+/-}^{\epsilon}$ indicate the normal direction of the habit plane and will be referred to as *habit plane normal directions*. The invariant plane strain condition corresponding to the *Hadamard jump condition* ensures the kinematic compatibility, i.e. a coherent interface between the phases, see Bhattacharya [2003]. Eshelby [1957] shows that the elastic energy of an infinitely thin oblate spheroid shaped inclusion could be reduced to zero if the eigenstrain ϵ^0 satisfies the invariant plane strain condition. This agrees not only with the experimentally observed habit plane but also with the martensite morphologies, often designated as plate- or disc-like, which is exemplary shown in Figure 3.3(b).

Generally, the eigenstrain tensor ϵ^0 is an invariant plane strain consisting of an eigenshear $\epsilon_{\text{shear}}^0$ in habit plane direction and a volume change ϵ_{vol}^0 perpendicular to the habit plane (see Zhang and Kelly [2009]). Depending on the shear direction, there are different martensitic orientation variants. This work is limited to two dimensions, assuming plane strain conditions. Hence, two different orientation variants (see Figure 3.3(a)) are taken into account with the eigenstrain tensors

$$\epsilon_1^0 = \begin{bmatrix} \epsilon_{\text{vol}}^0 & \epsilon_{\text{shear}}^0 & 0 \\ \epsilon_{\text{shear}}^0 & \epsilon_{\text{vol}}^0 & 0 \\ 0 & 0 & 0 \end{bmatrix}, \quad \epsilon_2^0 = \begin{bmatrix} \epsilon_{\text{vol}}^0 & -\epsilon_{\text{shear}}^0 & 0 \\ -\epsilon_{\text{shear}}^0 & \epsilon_{\text{vol}}^0 & 0 \\ 0 & 0 & 0 \end{bmatrix}. \quad (3.4)$$

3 Martensitic Transformations

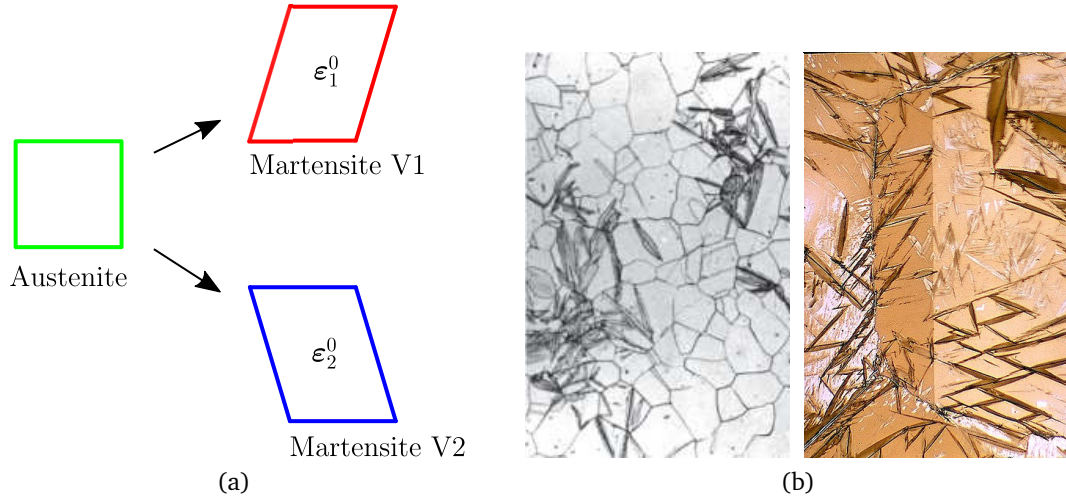


Figure 3.3: (a) Orientation variants of the martensitic phase. (b) Austenitic grains with martensite growing in a plate-like shape, Rios and Guimarães [2008], KTH Stockholm [2015].

The eigenvalues of ϵ_1^0 and ϵ_2^0 are given by

$$\epsilon_{I_1} = \epsilon_{I_2} = \epsilon_{\text{vol}}^0 - \epsilon_{\text{shear}}^0, \quad \epsilon_{II_1} = \epsilon_{II_2} = 0, \quad \epsilon_{III_1} = \epsilon_{III_2} = \epsilon_{\text{vol}}^0 + \epsilon_{\text{shear}}^0 \quad (3.5)$$

and satisfy the invariant plane strain condition in Eq. (3.2) if $\epsilon_{\text{shear}}^0 \geq \epsilon_{\text{vol}}^0$, or in the words of Cohen et al. [1979], if the phase transformation is deviatoric dominant. However, Eq. (3.2) is only satisfied by the transformation strain tensor for the two-dimensional case. For three dimensions it is fulfilled by the difference between the transformation strain tensors $\Delta\epsilon^0 = \epsilon_1^0 - \epsilon_2^0$, which stems from a martensite-martensite interface, with the eigenvalues

$$\epsilon_{I_\Delta} = -2 \epsilon_{\text{shear}}^0, \quad \epsilon_{II_\Delta} = 0, \quad \epsilon_{III_\Delta} = 2 \epsilon_{\text{shear}}^0. \quad (3.6)$$

This explains the experimentally observed twin related formation of martensite. An interested reader is referred to Bhattacharya [2003].

3.2 Driving Mechanisms

To look at the martensitic transformation from a thermodynamic point of view, a system with the Helmholtz free energy ψ , consisting of the different solid phases austenite and martensite is considered. A change from one phase into another will take place if the new phase is a more stable state of the system, i.e. the phase transition corresponds to a change towards the equilibrium. From the second law of

thermodynamics it can be derived¹ that for a given temperature T and a given strain tensor ε , the Helmholtz free energy ψ of a system has a minimum in an equilibrium state, i.e.

$$d\psi = 0. \quad (3.7)$$

Here, particularly the martensitic transformation in metastable austenitic stainless steels is in the focus. At room temperature, metastable austenites have due to their chemical composition an austenitic crystal structure. This corresponds to the metastable state, which is shown in Figure 3.4(a). The free energy ψ of a metastable

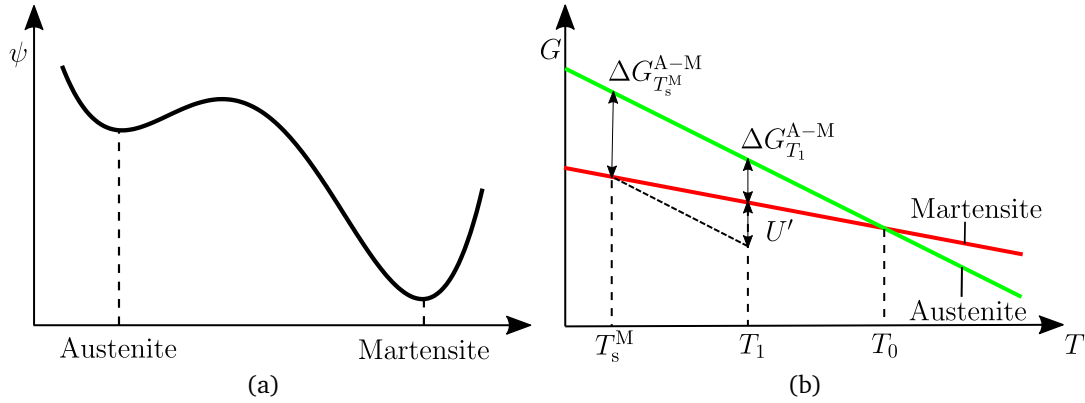


Figure 3.4: (a) Schematic variation of Helmholtz free energy with crystal structure for a fixed temperature. (b) Chemical free energies of austenite and martensite as a function of temperature, Tamura [1982].

austenitic steel is plotted as a function of the atom configurations of the system. For austenite, ψ has a local minimum indicating an equilibrium state, which satisfies Eq. (3.7). However, there is a more stable configuration 'martensite' where ψ has a global minimum. The austenitic configuration therefore corresponds to a *metastable* equilibrium, and the martensitic phase consequently to a *stable* equilibrium. From Figure 3.4(a) it becomes obvious that for the phase transformation from austenite to martensite activation energy is necessary to overcome the barrier between the minima. This activation energy is temperature dependent, which can be seen in Figure 3.4(b), showing schematically the chemical free energies of austenite (green curve) and martensite (red curve) as functions of temperature. For the *equilibrium temperature* T_0 the free energies of both phases are identical. For temperatures lower than T_0 martensite is the stable, austenite the metastable phase. At the *martensite start temperature* T_s^M the martensitic phase starts to grow by cooling, associated with the chemical driving force $\Delta G_{T_s^M}^{A-M}$. For a temperature T_1 (between T_s^M and T_0) the chemical driving force $\Delta G_{T_1}^{A-M}$ is insufficient to trigger the phase transformation. However, the mechanical energy U , which results from applied stress, can provide the necessary activation energy. Depending on the activation,

¹see e.g. Guggenheim [1967]. According to Fischer et al. [1994] the work potential pV is replaced by $-\sigma : \varepsilon$, cf. Chapter 2 of this work

3 Martensitic Transformations

there is a distinction between *thermally* and *mechanically induced martensite*.

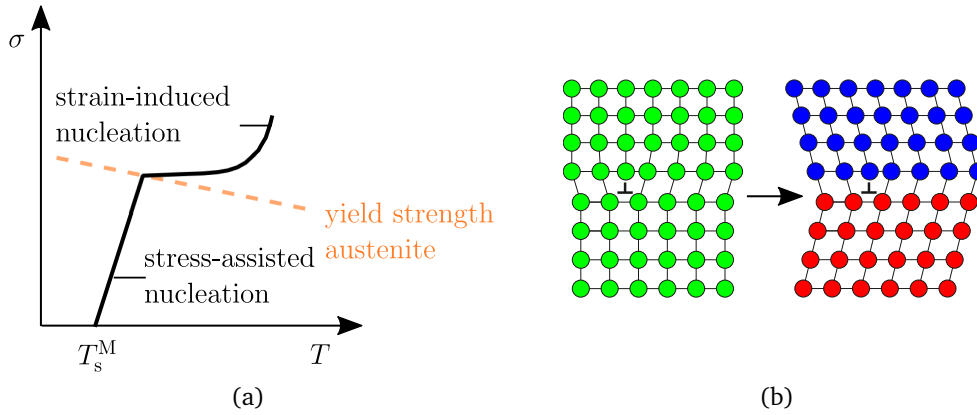


Figure 3.5: (a) Stress-assisted and strain-induced nucleation of martensite, see Olson and Cohen [1972]. (b) Austenitic lattice (green) is transformed to martensite (red and blue) while the dislocation indicated by \perp is inherited between the phases.

Concerning the latter which will be focused in the following, there are two different mechanisms to trigger the martensitic transformation. This can be seen in Figure 3.5(a), showing the stress dependent transformation path as a function of temperature. Below the martensite start temperature T_s^M , the phase transformation occurs spontaneously at preexisting nuclei. At higher temperatures the *stress-assisted nucleation* is initiated by the additional mechanical energy U in the form of applied stress, see the black line in Figure 3.5(a). If the applied stress exceeds the austenitic yield strength, which is indicated by an orange dashed line in Figure 3.5(a), the necessary stress increases less with respect to the temperature since plastic strain introduces new catalyzing defects leading to a *strain-induced nucleation*, see Olson and Cohen [1972, 1976]. Since the plastic deformations affect the stresses, plasticity and phase transformations can interact not only through the kinetics but also through the stresses. Thus, plastic deformations, resulting from dislocation movement, which accompanies the martensitic transformation, play an important role for the phase transition.

For the model introduced in this work, plastic deformations are taken into account. Regarding the phase transformation, it is assumed that the plastic deformation can be inherited from the austenitic to the martensitic phase. The assumption is motivated by Figure 3.5(b), which shows a dislocation in the austenite. This dislocation is supposed not to vanish due to the phase transformation to martensite, resulting in a dislocation in the martensitic phase, which is inherited from the austenite. Furthermore, the martensitic phase is harder, more brittle and has a higher yield strength than austenite, see e.g. Skorupski et al. [2014].

Additionally, microcracks are observed on the microscale of austenitic stain-

3.2 Driving Mechanisms

less steels. This is illustrated in Figure 3.6, showing a micrograph with cracks in an austenite-martensite microstructure. It can be seen that the microcracks appear



Figure 3.6: Micrograph of microcracks arising in plate-shaped martensite, Marder et al. [1970].

exclusively in the martensite, both in the transition zone between two plates and perpendicular to the plate directions. So, obviously the martensitic phase influences the fracture process.

In the next chapter a continuum phase field model for martensitic transformations is introduced which considers the above discussed characteristics. With the aid of the model the complex interactions between the different mechanisms on the microscale of metastable steels are studied.

3 *Martensitic Transformations*

4 An Elastic Phase Field Model for Martensitic Transformations

In this chapter a continuum model for martensitic transformations is introduced. The interested reader is also referred to Fischer et al. [1994], where the continuum mechanical aspects of phase transformations in solids are discussed, giving rise to different model approaches. In Reisner et al. [1998] the strain induced martensitic transformation is described via a thermodynamic transformation criterion, while in Bartel and Hackl [2008], Bartel et al. [2011] the concept of energy relaxation is applied and the evolution equations are derived from inelastic properties. Assuming an infinitely sharp interface between the phases the martensitic transformation is micromechanically modeled with the concept of moving boundaries in Cherkaoui et al. [1998], Cherkaoui and Berveiller [2000]. However, the numerical realization of this approach is generally difficult, e.g. problems arise due to the tracking of the interfaces. These can be circumvented by regularizing the discontinuities within the phase field approach, which introduces an order parameter. The evolution of the order parameter is described with the time-dependent Ginzburg-Landau equation. Based on Chen et al. [1992] and Wang and Khachaturyan [1997], several phase field models dealing with the martensitic transformation are proposed, differing in the numerical realization. Jin et al. [2001], Artemev et al. [2000], Ahluwalia et al. [2004] are exemplary works using fast Fourier transformation for the numerical solution. Alternatively finite differences e.g. Yamanaka et al. [2008] or finite elements e.g. Hildebrand and Miehe [2010, 2011], Levitas et al. [2010], Yeddu et al. [2012], Malik et al. [2013], Levitas et al. [2013], Schmitt et al. [2013a,c] are applied.

In the following chapter a phase field model for martensitic transformations is introduced, considering the characteristics of the phase transition, which are outlined in Chapter 3. In Section 4.1, the basic equations and the model parameters are given for the one-dimensional case. Subsequently, in Section 4.2 the parameters are calibrated for pure iron by comparison with atomistic simulations. Therefore, the model is extended to two dimensions and implemented into a finite element scheme, which is also discussed briefly. Finally, in Section 4.3, metastable austenitic steels are considered to study the impact of the volumetric eigenstrain, the necessity of different orientation variants and the influence of external loads on the formation of the microstructure.

4.1 One-Dimensional Model

First, the phase field approach is motivated using a basic one-dimensional example. On this basis, the evolution equation of the order parameter is derived applying a thermodynamically consistent continuum theory. By introducing calibration constants the model parameters are subsequently identified.

4.1.1 Motivation

In order to introduce the phase field concept an indefinitely extended one-dimensional continuum as depicted in Figure 4.1(a) is considered. The body consists of the phases austenite and martensite, which differ in their crystal structure and are separated by an interface \mathcal{S} at $x = 0$. The present phase is indicated by an order parameter $\varphi(x) \in [0, 1]$, where $\varphi = 0$ corresponds to austenite and $\varphi = 1$ to martensite, resulting in a discontinuous function

$$\varphi(x) = \begin{cases} 0 & x < 0 \\ 1 & x \geq 0 \end{cases}, \quad (4.1)$$

which is plotted in dependence of x in Figure 4.1(b). It is often cumbersome to deal with discontinuities especially regarding the numerical realization. The difficulties can be circumvented by using the smooth interpolation

$$\varphi(x) = \frac{1}{2} \left[\tanh \left(\frac{2x}{\ell} \right) + 1 \right], \quad (4.2)$$

see Hildebrand and Miehe [2010], McFadden et al. [1993]. The plot of this function

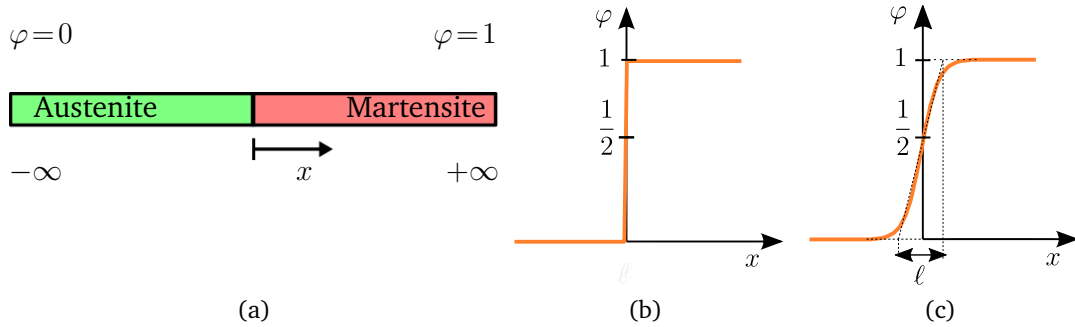


Figure 4.1: (a) Indefinitely extended two phase one-dimensional continuum. (b) Discontinuous change of the order parameter. (c) Smooth change of the order parameter.

in Figure 4.1(c) shows that the length of the transition zone between $\varphi = 0$ and $\varphi = 1$ corresponds to the parameter ℓ since

$$\varphi'(x) = \frac{1}{\ell} \left[1 - \tanh^2 \left(\frac{2x}{\ell} \right) \right] \Big|_{x=0} = \frac{1}{\ell} \quad \text{with} \quad \langle \cdot \rangle' = \frac{d\langle \cdot \rangle}{dx}. \quad (4.3)$$

Concerning the phase field ansatz it is interesting to note that Eq. (4.2) solves the partial differential equation

$$\varphi''(x) = \frac{32}{\ell^2} \varphi(x) \left(\varphi(x) - \frac{1}{2} \right) \left(\varphi(x) - 1 \right), \quad (4.4)$$

$$\Leftrightarrow \frac{16}{\ell} \left(\varphi^3(x) - \frac{3}{2} \varphi^2(x) + \frac{1}{2} \varphi(x) \right) - \frac{\ell}{2} \varphi''(x) = 0, \quad (4.5)$$

which can be identified as the Euler-Lagrange equation

$$\frac{\partial \tilde{\psi}}{\partial \varphi} - \frac{d}{dx} \frac{\partial \tilde{\psi}}{\partial \varphi'} = 0 \quad (4.6)$$

of the variational problem

$$\int_{-\infty}^{+\infty} \delta \tilde{\psi} \, dx = 0 \quad \text{with} \quad \tilde{F} = \int_{-\infty}^{+\infty} \tilde{\psi} \, dx, \quad \tilde{\psi} = \frac{16}{\ell} \underbrace{\left(\frac{1}{4} \varphi^4 - \frac{1}{2} \varphi^3 + \frac{1}{4} \varphi^2 \right)}_{\tilde{f}(\varphi)} + \frac{\ell}{4} (\varphi')^2, \quad (4.7)$$

see also Hildebrand [2013]. In Eq. (4.7), the quantity \tilde{F} could be interpreted as the total free energy of the one-dimensional continuum in Figure 4.1(a), which is the volume integral of the local free energy density $\tilde{\psi}$, consisting of a double well polynomial function $\tilde{f}(\varphi)$ and a gradient term. For this one-dimensional example the elastic energy is not taken into account. The static problem can be extended to moving interfaces, which is shown in the next paragraph.

4.1.2 Evolution Equation of the Order Parameter

To consider propagating interfaces, an evolution equation for the order parameter is required, which is derived in this section. Therefore, an arbitrary body \mathcal{B} as depicted in Figure 2.1 is regarded. According to the thermodynamically consistent continuum theory proposed by Fried and Gurtin [1993, 1994], Gurtin [1996] a *microforce system* is introduced, consisting of the *vector stress* $\boldsymbol{\xi}$, the *internal and external* (scalar) *body forces* Π and γ , respectively. The microstresses and the microforces obey the *microforce balance* in global and local form

$$\int_{\partial \mathcal{B}} \boldsymbol{\xi} \cdot \mathbf{n} \, da - \int_{\mathcal{B}} (\Pi + \gamma) \, dv = 0, \quad \text{div } \boldsymbol{\xi} + \Pi + \gamma = 0. \quad (4.8)$$

4 An Elastic Phase Field Model for Martensitic Transformations

The microforces¹ account for the work associated with changes in the order parameter φ . Hence, the terms $\int_{\partial\mathcal{B}} \boldsymbol{\xi} \cdot \mathbf{n} \dot{\varphi} \, da$ and $\int_{\mathcal{B}} \gamma \dot{\varphi} \, dv$ have to be considered for the power of external forces P in Eq. (2.25), entering the energy balance in Eq. (2.26) and eventually appear in the Clausius Duhem inequality in Eq. (2.40)

$$\dot{\psi} - \boldsymbol{\sigma} : \dot{\boldsymbol{\varepsilon}} - \boldsymbol{\xi} \cdot \nabla \dot{\varphi} + \Pi \dot{\varphi} \leq 0, \quad (4.9)$$

where the local form of the microforce balance in Eq. (4.8) has been used. Furthermore, the order parameter and its gradient are added to the list of variables of the Helmholtz free energy $\psi = \hat{\psi}(\boldsymbol{\varepsilon}, \varphi, \nabla \varphi)$ and its time derivative can be calculated accordingly

$$\dot{\psi} = \frac{\partial \psi}{\partial \boldsymbol{\varepsilon}} : \dot{\boldsymbol{\varepsilon}} + \frac{\partial \psi}{\partial \varphi} \dot{\varphi} + \frac{\partial \psi}{\partial \nabla \varphi} \cdot \nabla \dot{\varphi}. \quad (4.10)$$

Inserting Eq. (4.10) into the Clausius Duhem inequality in Eq. (4.9) yields

$$\left(\frac{\partial \psi}{\partial \boldsymbol{\varepsilon}} - \boldsymbol{\sigma} \right) : \dot{\boldsymbol{\varepsilon}} + \left(\frac{\partial \psi}{\partial \nabla \varphi} - \boldsymbol{\xi} \right) \cdot \nabla \dot{\varphi} + \left(\Pi + \frac{\partial \psi}{\partial \varphi} \right) \dot{\varphi} \leq 0. \quad (4.11)$$

Requiring the fulfillment of Eq. (4.11) for any given rates of $\boldsymbol{\varepsilon}$, φ , $\nabla \varphi$ results in the constitutive relations

$$\boldsymbol{\sigma} = \frac{\partial \psi}{\partial \boldsymbol{\varepsilon}}, \quad \boldsymbol{\xi} = \frac{\partial \psi}{\partial \nabla \varphi}, \quad (4.12)$$

and the following remaining inequality

$$\underbrace{\left(\Pi + \frac{\partial \psi}{\partial \varphi} \right)}_{\Pi^{\text{dis}}} \dot{\varphi} \leq 0, \quad (4.13)$$

with $\Pi^{\text{dis}} = \hat{\Pi}^{\text{dis}}(\boldsymbol{\varepsilon}, \varphi, \nabla \varphi)$. According to Gurtin [1996], the most general form of Π^{dis} consistent with Eq. (4.13) is

$$\Pi^{\text{dis}} = -\beta \dot{\varphi}, \quad (4.14)$$

with the scalar mobility parameter $\beta \geq 0$. Choosing a constant mobility parameter and inserting the above derived quantities

$$\boldsymbol{\xi} = \frac{\partial \psi}{\partial \nabla \varphi} \quad \Pi = -\frac{\partial \psi}{\partial \varphi} - \beta \dot{\varphi} \quad (4.15)$$

into the local microforce balance in Eq. (4.8) yields in absence of external microforces ($\gamma = 0$)

$$\beta \dot{\varphi} = \text{div} \frac{\partial \psi}{\partial \nabla \varphi} - \frac{\partial \psi}{\partial \varphi} = -\frac{\delta \psi}{\delta \varphi}, \quad (4.16)$$

¹The forces are designated as "micro" since the change in order parameter is associated with atom configurations on the microscale.

the time-dependent Ginzburg-Landau equation (TDGL). It describes the evolution of the order parameter φ to be proportional to the variational derivative of ψ with respect to φ . Since for equilibrium states $\frac{\delta\psi}{\delta\varphi} = 0$, this equation characterizes the relaxation towards equilibrium. Inserting the local free energy density $\tilde{\psi}$ of the one-dimensional continuum given in Eq. (4.7) into Eq. (4.16) yields

$$-\beta\dot{\varphi} = \left[\frac{16}{\ell} \left(\varphi^3 - \frac{2}{3}\varphi^2 + \frac{1}{2}\varphi \right) - \frac{\ell}{2}\varphi'' \right], \quad (4.17)$$

where the right-hand side of Eq. (4.17) corresponds to the Euler-Lagrange equation of the static variational problem in Eq. (4.5) which is solved in Section 4.1.1. Taking the motivating example of Section 4.1.1 as a starting point, the basic equations of the phase field model are given in the following.

4.1.3 Model Parameters

The local free energy density $\tilde{\psi}$ of the one-dimensional continuum depicted in Figure 4.1(a) is given in Eq. (4.7) in terms of a double well potential and a gradient term

$$\tilde{\psi} = \underbrace{\frac{16}{\ell} \left(\frac{1}{4}\varphi^4 - \frac{1}{2}\varphi^3 + \frac{1}{4}\varphi^2 \right)}_{\tilde{\psi}^{\text{sep}}} + \underbrace{\frac{\ell}{4}\varphi'^2}_{\tilde{\psi}^{\text{grad}}}. \quad (4.18)$$

In the context of phase field modeling $\tilde{\psi}$ is also designated as the *phase field potential*. In a more general way, the terms in Eq. 4.18 are reformulated using the *phase separation potential* $\tilde{\psi}^{\text{sep}} = \kappa_{\text{sep}} \frac{G}{L} f(\varphi)$ and the *gradient energy density* $\tilde{\psi}^{\text{grad}} = \frac{1}{2} \kappa_{\text{grad}} G L \varphi'^2$. Analogously to the parameter ℓ in Eq. (4.18), the parameter L appears in both terms. The model parameters are introduced below. With $\tilde{\psi}^{\text{sep}}$ and $\tilde{\psi}^{\text{grad}}$ the evolution equation of the order parameter reads

$$\dot{\varphi} = -\frac{1}{\beta} \left[\frac{\partial\psi}{\partial\varphi} - \left(\frac{\partial\psi}{\partial\varphi'} \right)' \right] = -\frac{1}{\beta} \left(\kappa_{\text{sep}} \frac{G}{L} \frac{\partial f}{\partial\varphi} - \kappa_{\text{grad}} G L \varphi'' \right). \quad (4.19)$$

To allow the model to account for stable and metastable states, the double well function in Eq. (4.18) is replaced by the Landau polynomial

$$f(\varphi) = D + \frac{A}{2}\varphi^2 - \frac{B}{3}\varphi^3 + \frac{C}{4}\varphi^4, \quad (4.20)$$

proposed by Yamanaka et al. [2008]. The plot of $f(\varphi)$ in Figure 4.2(a) shows a local minimum, corresponding to a metastable state and a global minimum, corresponding to a stable state. Here, the coefficients A , B , C and D are chosen such that the local minimum is at $\varphi = 0$ and the global minimum at $\varphi = 1$. This models the metastable phase austenite and the stable phase martensite, respectively. For the

4 An Elastic Phase Field Model for Martensitic Transformations

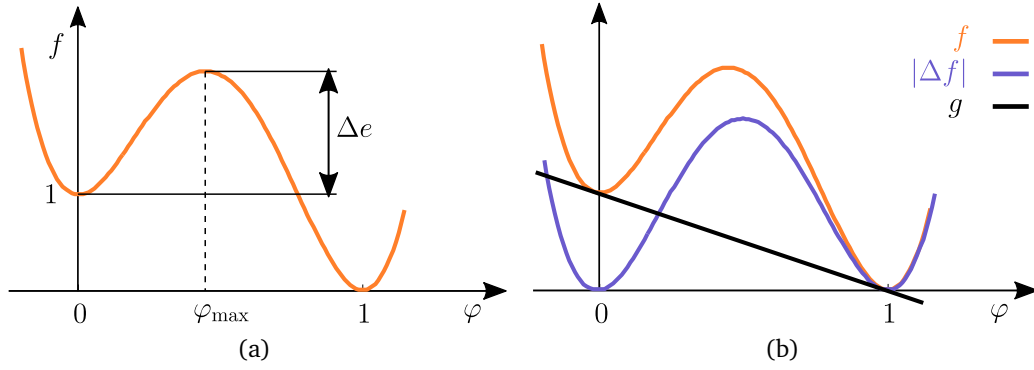


Figure 4.2: (a) Landau polynomial $f(\varphi)$ with the energy barrier Δe . (b) For a uniquely defined Σ_{if} , a symmetric reference state $|\Delta f|$ is necessary.

change of $\varphi = 0$ to $\varphi = 1$, the system has to overcome an energy barrier

$$\Delta e = f(\varphi_{\max}) - f(0) \quad \text{with} \quad \varphi_{\max} = \underset{\varphi \in [0,1]}{\operatorname{argmax}} f(\varphi), \quad (4.21)$$

which is indicated in Figure 4.2(a). Since the energy landscape depends on temperature, the coefficients are temperature dependent, too. For $T < T_0$ martensite is the stable phase which is ensured by $D = 1$, $B = 3A + 12$ and $C = 2A + 12$. For $T > T_0$ the relations $D = 0$, $B = 3A - 12$ and $C = 2A - 12$ lead to a global minimum at $\varphi = 0$.

In order to still be able to control the width of the interface by the parameter L , the calibration constants κ_{sep} and κ_{grad} are introduced, based on the works of Cahn and Hilliard [1958], Schrade et al. [2008, 2013]. For the sake of clarity, only temperatures below the equilibrium temperature T_0 are considered since the procedure for $T > T_0$ is the same. Starting point is an indefinitely extended one-dimensional continuum consisting of two phases as shown in Figure 4.1(a). In terms of the parameters G , L and the constants κ_{sep} , κ_{grad} the global free energy F of the system reads

$$F(\varphi, \varphi') = \int_{-\infty}^{+\infty} \psi(\varphi, \varphi') \, dx = \int_{-\infty}^{+\infty} \left(\kappa_{\text{sep}} \frac{G}{L} f(\varphi) + \frac{1}{2} \kappa_{\text{grad}} G L (\varphi')^2 \right) \, dx. \quad (4.22)$$

The approach results in G corresponding to the specific interface energy Σ_{if} between the phases, where Σ_{if} is the difference of the actual free energy of the system and the free energy of the system for a single phase, per interface area. However, the asymmetric Landau polynomial $f(\varphi)$ results in different free energies for a single phase, depending on whether austenite or martensite is present. Hence, for a unique definition of Σ_{if} , a standard equilibrium state of the phases

4.1 One-Dimensional Model

$|\Delta f(\varphi)| = |f(\varphi) - g(\varphi)|$ with $g(\varphi) = 1 - \varphi$ is defined.² The plot of the functions in Figure 4.2(b) shows that $|\Delta f|$ is a symmetric function with two equal minima. For small values of A , there is an intersection of f and g so that the absolute value of Δf is used to ensure minimal values of $|\Delta f| = 0$ for $\varphi = 0$ and $\varphi = 1$. However, this adjustment implicates slightly inaccurate results for small values of A .

With the symmetric reference state $|\Delta f|$ taken into account, the specific interface energy of the system can be uniquely described

$$\Sigma_{\text{if}} = \int_{-\infty}^{+\infty} \left(\kappa_{\text{sep}} \frac{G}{L} |\Delta f(\varphi)| + \frac{1}{2} \kappa_{\text{grad}} G L (\varphi')^2 \right) dx = \int_{-\infty}^{+\infty} \check{\psi} dx. \quad (4.23)$$

Since a one-dimensional problem is considered, the interface area does not appear in Eq. (4.23). For equilibrium states, Σ_{if} is minimal such that the Euler-Lagrange equation can be applied on the integrand³ in Eq. (4.23),

$$\check{\psi} - \varphi' \frac{\partial \check{\psi}}{\partial \varphi'} = 0, \quad (4.24)$$

$$\kappa_{\text{sep}} \frac{G}{L} |\Delta f| - \frac{1}{2} \kappa_{\text{grad}} G L (\varphi')^2 = 0 \quad \rightsquigarrow \quad \varphi' = \frac{1}{L} \sqrt{2 \frac{\kappa_{\text{sep}}}{\kappa_{\text{grad}}} |\Delta f|}. \quad (4.25)$$

In analogy to Section 4.1.1, where the length of the transition zone is given by the parameter ℓ , Eq. (4.25.2) is evaluated for the position of the interface $x = x_{\text{if}}$ which is defined with $x_{\text{if}} := \{x \mid \varphi(x) = 0.5\}$ and equated with $\frac{1}{L}$,

$$\left. \frac{d\varphi}{dx} \right|_{x_{\text{if}}} = \frac{1}{L} \sqrt{2 \frac{\kappa_{\text{sep}}}{\kappa_{\text{grad}}} |\Delta f(\varphi(x_{\text{if}}))|} \stackrel{!}{=} \frac{1}{L}. \quad (4.26)$$

In a second equation the parameter G is identified with the interface energy

$$\Sigma_{\text{if}} = \int_{-\infty}^{+\infty} \check{\psi} dx = G \sqrt{2 \kappa_{\text{sep}} \kappa_{\text{grad}}} \int_0^1 \sqrt{|\Delta f|} d\varphi \stackrel{!}{=} G, \quad (4.27)$$

where Eq. (4.25.1) has been inserted to calculate $\check{\psi}$ while the integral is transformed using Eq. (4.25.2). To calculate the calibrations constants κ_{sep} and κ_{grad} , Eq. (4.26) and Eq. (4.27) are recast,

$$\kappa_{\text{grad}} = 2 \kappa_{\text{sep}} |\Delta f(\varphi(x_{\text{if}}))|, \quad \kappa_{\text{sep}} \kappa_{\text{grad}} = \frac{1}{2} \left(\int_0^1 \sqrt{|\Delta f|} d\varphi \right)^{-2}, \quad (4.28)$$

²For $T > T_0$, the function $g(\varphi) = \varphi$ has to be considered.

³Since $\check{\psi}$ does not explicitly dependent on x , the Euler-Lagrange equation can be written in the stated way, cf. Margenau and Murphy [1965].

4 An Elastic Phase Field Model for Martensitic Transformations

resulting in the calibration constants

$$\kappa_{\text{sep}} = \left(2\sqrt{|\Delta f(\varphi(x_{\text{if}}))|} \int_0^1 \sqrt{|\Delta f|} d\varphi \right)^{-1}, \quad \kappa_{\text{grad}} = \frac{\sqrt{|\Delta f(\varphi(x_{\text{if}}))|}}{\int_0^1 \sqrt{|\Delta f|} d\varphi}, \quad (4.29)$$

which depend on the Landau polynomial $f(\varphi)$.

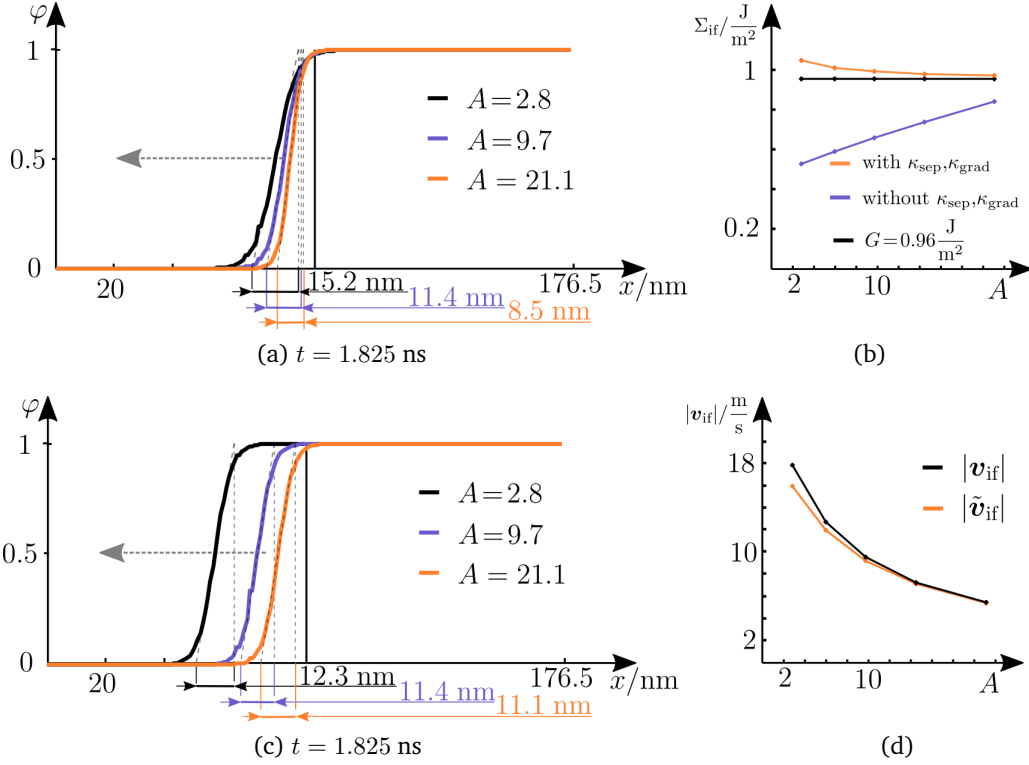


Figure 4.3: Plot of $\varphi(x)$ for different values of A , (a) without and (c) with considering κ_{sep} , κ_{grad} . (b) Interface energy density in comparison with G . (d) Interface velocities depending on A .

To illustrate the impact of the calibration constants, the evolution equation (4.19) is solved for a one-dimensional continuum consisting of two continuous phases (cf. Figure 4.1(a)) with a length of 176.5 nm, using the parameters $G = 0.96 \frac{\text{J}}{\text{m}^2}$, $L = 10 \text{ nm}$ and the mobility constant $\beta = 0.238 \frac{\text{Ns}}{\text{m}^2}$. Isothermal conditions are assumed where $T < T_0$ such that martensite is the stable phase, and thus, the interface propagates to the left. Indicating the interface position for $t = 0$ with a solid black line, Figure 4.3(a) shows the resulting interface profiles $\varphi(x)$ at $t = 1.825 \text{ ns}$ for $A = [2.8, 9.7, 21.1]$ where the calibration constants κ_{sep} and κ_{grad}

are not considered.⁴ The interface width increases with a decreasing coefficient A . Additionally, the purple curve Figure 4.3(b) shows that the specific interface energy Σ_{if} calculated according to Eq. (4.23) is varying strongly for the different values of A . Since the interface energy is a material parameter it should be considered as input data of the model, which is difficult to realize with Σ_{if} depending on the coefficient A . Similarly, the interface width should be known, especially when the problem is solved numerically using the finite element approach, which requires to resolve the interface region by several elements. For the results shown in Figure 4.3(c), the calibration constants are calculated according to Eq. (4.29). Despite the wide range of A this leads to almost constant values of the interface width which corresponds to the parameter L . Furthermore, Figure 4.3(b) indicates that interface energy (orange curve) fits the parameter G (black curve). This behavior is not unique to the given parameter set and can also be observed for different choices of the parameters L and G .

4.1.4 Interface Velocity

With the parameter L describing the interface width, an approximation of the interface velocity \tilde{v}_{if} can be calculated making use of the chain rule

$$\dot{\varphi}\Big|_{x_{\text{if}}} = \frac{d\varphi}{dx_{\text{if}}} \frac{dx_{\text{if}}}{dt} \approx \frac{1}{L} \dot{x}_{\text{if}} \rightsquigarrow \tilde{v}_{\text{if}} := L \dot{\varphi}\Big|_{x_{\text{if}}} \quad (4.30)$$

where $\dot{\varphi}\Big|_{x_{\text{if}}}$ is evaluated using the evolution equation (4.19) with $\varphi\Big|_{x_{\text{if}}} = 0.5$

$$\dot{\varphi}\Big|_{x_{\text{if}}} = -\frac{1}{\beta} \left(\kappa_{\text{sep}} \frac{G}{L} \underbrace{\frac{\partial f}{\partial \varphi}\Big|_{\varphi=0.5}}_{\pm \frac{3}{2}} - \underbrace{\kappa_{\text{grad}} G L \varphi''\Big|_{x=0}}_{\approx 0} \right). \quad (4.31)$$

In Eq. (4.31) the second term in brackets is neglected with reference to the analytical solution in Eq. (4.2). Inserting $\varphi = 0.5$ into the derivative of the Landau polynomial with respect to the order parameter yields $\frac{\partial f}{\partial \varphi}\Big|_{\varphi=0.5} = \pm \frac{3}{2}$ independent of A because of the temperature dependent definitions of the coefficients B and C . The negative sign holds for $T < T_0$, the positive sign for for $T > T_0$. This results with Eq. (4.30.2) in the interface velocity

$$\tilde{v}_{\text{if}} = \begin{cases} -\frac{3}{2} \frac{\kappa_{\text{sep}} G}{\beta} & T < T_0 \\ \frac{3}{2} \frac{\kappa_{\text{sep}} G}{\beta} & T > T_0 \end{cases}. \quad (4.32)$$

⁴The plots of the Landau polynomial $f(\varphi)$ for the corresponding values of A can be seen in Figure 4.9(a) designated with $T = 100$ K, $T = 300$ K and $T = 500$ K.

4 An Elastic Phase Field Model for Martensitic Transformations

The sign in Eq. (4.32) is in accordance with the results in Figure 4.3(c), where the interface propagates in negative x -direction for $T < T_0$.

Alternatively, the interface velocity of a phase field model can be calculated using *configurational forces*, which were originally introduced by Eshelby [1951]. Within the theory of configurational forces, driving forces on material inhomogeneities are derived by energetic considerations and thus can be applied to analyze material defects. For more detailed informations the reader is referred to textbooks on this topic, e.g. Kienzler and Herrmann [2000], Gurtin [2000], Müller [2005]. In Kuhn [2013], the concept of configurational forces is extensively discussed in the context of phase field modeling, providing a better insight into the energetic driving mechanisms of the evolution of the phases. Here, the approach is picked up to calculate the interface velocity and hence is briefly introduced. Differing from Eshelby's approach that is described e.g. in Kanninen [1970], in this work instead of the elastic energy density, the phase field potential ψ is considered. The phase field potential is assumed to depend on the order parameter φ , its gradient φ' and the location of the interface x^{if} , i.e. $\psi = \hat{\psi}(\varphi, \varphi', x^{\text{if}})$. Furthermore, the free energy ψ does not depend explicitly on x since no inhomogeneities are considered. Thus, differentiation of ψ with respect to x yields

$$\begin{aligned} \psi' &= \frac{\partial\psi}{\partial\varphi}\varphi' + \frac{\partial\psi}{\partial\varphi'}\varphi'' + \frac{\partial\psi}{\partial x^{\text{if}}}(x^{\text{if}})' \quad \text{where} \quad \frac{\partial\psi}{\partial\varphi'}\varphi'' = \left(\frac{\partial\psi}{\partial\varphi'}\varphi'\right)' - \left(\frac{\partial\psi}{\partial\varphi'}\right)'\varphi' \\ \psi' &= \left[\frac{\partial\psi}{\partial\varphi} - \left(\frac{\partial\psi}{\partial\varphi'}\right)'\right]\varphi' + \left(\frac{\partial\psi}{\partial\varphi'}\right)' + \frac{\partial\psi}{\partial x^{\text{if}}}(x^{\text{if}})' \quad \text{with Eq. (4.19.1)} \\ \psi' &= -\dot{\varphi}\beta\varphi' + \left(\frac{\partial\psi}{\partial\varphi'}\right)' + \frac{\partial\psi}{\partial x^{\text{if}}}(x^{\text{if}})'. \end{aligned} \quad (4.33)$$

Equation (4.33) may be rewritten as the *configurational force balance*

$$\Sigma' + g = 0, \quad \text{with} \quad \Sigma = \psi - \frac{\partial\psi}{\partial\varphi'}\varphi' \quad \text{and} \quad g = \underbrace{\dot{\varphi}\beta\varphi'}_{= g^{\text{dis}}} - \underbrace{\frac{\partial\psi}{\partial x^{\text{if}}}(x^{\text{if}})'}_{= g^{\text{if}}} \quad (4.34)$$

where Σ is the *generalized Eshelby stress* and g the *generalized configurational volume force* for this one-dimensional setting. To calculate the interface velocity for the one-dimensional continuum in Figure 4.1(a) according to Kuhn [2013], the dissipative part of the configurational force is defined as

$$G^{\text{dis}} = \int_{-\infty}^{+\infty} -g^{\text{dis}} \, dx = \int_{-\infty}^{+\infty} -\dot{\varphi}\beta\varphi' \, dx. \quad (4.35)$$

The phase transition is described by the smooth approximation of the interface $\varphi(x, t)$, which is assumed to propagate unchanged with its initial profile φ_0 ,

4.2 Phase Field Model for Multivariant Martensitic Transformations

i.e. $\varphi(x, t) = \varphi_0(x - l(t))$, with $l(t)$ describing the interface position at time t , see Figure 4.4. Computing the time derivative

$$\dot{\varphi}(x, t) = \frac{d\varphi}{dt} = \frac{d}{dx}\varphi(x - l(t))\frac{d}{dt}(x - l(t)) = -\varphi' l' := -\varphi' \dot{x}_{\text{if}}, \quad (4.36)$$

yields after the multiplication with $-\beta\varphi'$ and subsequent integration over the length of the one-dimensional continuum

$$\dot{x}_{\text{if}} = v_{\text{if}} = \frac{G^{\text{dis}}}{\int_{-\infty}^{+\infty} \beta(\varphi')^2 dx}. \quad (4.37)$$

When the phase field problem is solved, all quantities in Eq. (4.37) are known and the interface velocity can be computed easily. Alternatively, this could be done more costly in the course of post processing by tracking the interface position.

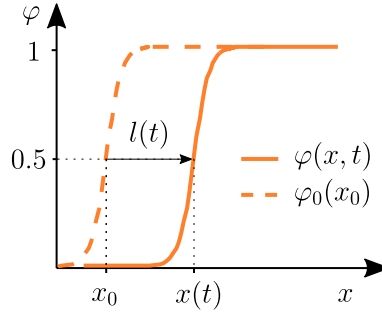


Figure 4.4: The initial interface profile φ_0 is assumed to propagate unchanged through the beam.

In Figure 4.3(d) the approximation of the interface velocity $|\tilde{v}^{\text{if}}|$, calculated according to Eq. (4.32) (orange curve), and $|v^{\text{if}}|$, which is determined using the dissipative part of the configurational forces according to Eq. (4.37) (black curve), are plotted with regard to the coefficient A . It can be seen, that $|\tilde{v}^{\text{if}}|$ and $|v^{\text{if}}|$ are in good agreement, confirming properly chosen calibration constants. For both curves the interface velocity increases for a decreasing coefficient A , which corresponds to a smaller energy barrier (cf. Figure 4.9(a)). In the next step, information from atomistic simulations is included to calibrate the mobility constant β .

4.2 Phase Field Model for Multivariant Martensitic Transformations

In this section the model parameters are determined according to results from molecular dynamic (MD) simulations. In a first step this is done for pure iron.

4 An Elastic Phase Field Model for Martensitic Transformations

In the future, the MD simulations will be extended to iron-carbon systems, where eventually further alloying elements will be considered and material parameters for metastable austenitic steels could be deduced. This thesis proposes a general approach to calibrate the mobility parameter β using information from atomistic simulation of pure iron according to the work of Schmitt et al. [2013c]. The model equations, which are extended to the two-dimensional case, are discussed in Section 4.2.1 followed by the numerical implementation with finite elements in Section 4.2.2, based on Schmitt et al. [2012, 2013a]. In Section 4.2.3 the parameters are determined with the aid of MD simulations, while in Section 4.2.4 the impact of an external load on the evolution of the martensitic phase is touched briefly.

4.2.1 Model Equations

In order to enable the cooperation with atomistic simulations, the one-dimensional model is extended to two dimensions. To write the model equations more generally, two martensitic orientation variants are considered. Thus, a second order parameter is introduced, where $\varphi_1 = \varphi_2 = 0$ for the austenitic phase and $\varphi_1 = 1$ for the first and $\varphi_2 = 1$ for the second martensitic variant. Including even more martensite variants is straightforward, cf. Schmitt et al. [2013c]. As far as possible, φ_i with $i = 1, 2$ is used instead of φ_1 and φ_2 for the sake of clarity. In Section 3.1 the crucial role of the elastic energy in the context of the martensitic transformations is discussed. It is therefore included in the local energy of the system and the linearized strain tensor $\boldsymbol{\varepsilon}$ enters the list of variables

$$\psi(\boldsymbol{\varepsilon}, \varphi_i, \nabla \varphi_i) = W(\boldsymbol{\varepsilon}, \varphi_i) + \psi^{\text{grad}}(\nabla \varphi_i) + \psi^{\text{sep}}(\varphi_i) \quad (4.38)$$

with

$$W(\boldsymbol{\varepsilon}, \varphi_i) = \frac{1}{2} [\boldsymbol{\varepsilon} - \boldsymbol{\varepsilon}_\varphi^0(\varphi_i)] : \mathbf{C}(\varphi_i) [\boldsymbol{\varepsilon} - \boldsymbol{\varepsilon}_\varphi^0(\varphi_i)]. \quad (4.39)$$

The elastic energy density W considers the transformation-induced eigenstrain $\boldsymbol{\varepsilon}_\varphi^0(\varphi_i)$ which arises due to the crystallographic misfit of the austenitic and the martensitic phases. The eigenstrain tensor $\boldsymbol{\varepsilon}_\varphi^0$ and the elasticity tensor \mathbf{C} depend linearly on the order parameters φ_1, φ_2

$$\boldsymbol{\varepsilon}_\varphi^0(\varphi_1, \varphi_2) = \varphi_1 \boldsymbol{\varepsilon}_1^0 + \varphi_2 \boldsymbol{\varepsilon}_2^0, \quad \mathbf{C}(\varphi_1, \varphi_2) = \mathbf{C}_A + \varphi_1(\mathbf{C}_{M_1} - \mathbf{C}_A) + \varphi_2(\mathbf{C}_{M_2} - \mathbf{C}_A). \quad (4.40)$$

With the lattice parameters known from MD, the eigenstrain $\boldsymbol{\varepsilon}_i^0$ of the martensitic phases is calculated using the Bain model. Assuming plane strain conditions, the eigenstrain tensor of the first variant results from the geometrical relations in the x - z -plane of Figure 3.1. A rotation of the coordinate system in Figure 3.1 by 90°

4.2 Phase Field Model for Multivariant Martensitic Transformations

yields eigenstrain tensor of the second variant,

$$\boldsymbol{\varepsilon}_1^0 = \begin{bmatrix} \frac{\sqrt{2}a_{\text{bcc}} - a_{\text{fcc}}}{a_{\text{fcc}}} & 0 \\ 0 & \frac{a_{\text{bcc}} - a_{\text{fcc}}}{a_{\text{fcc}}} \end{bmatrix}, \quad \boldsymbol{\varepsilon}_2^0 = \begin{bmatrix} \frac{a_{\text{bcc}} - a_{\text{fcc}}}{a_{\text{fcc}}} & 0 \\ 0 & \frac{\sqrt{2}a_{\text{bcc}} - a_{\text{fcc}}}{a_{\text{fcc}}} \end{bmatrix}. \quad (4.41)$$

In Eq. (4.38), the gradient term and the separation potential for the two-dimensional case read

$$\psi^{\text{grad}} = \frac{1}{2} \kappa_{\text{grad}} G L \sum_{i=1}^2 |\nabla \varphi_i|^2, \quad \psi^{\text{sep}} = \kappa_{\text{sep}} \frac{G}{L} f(\varphi_i), \quad (4.42)$$

with the Landau polynomial $f(\varphi_1, \varphi_2)$ extended to two martensitic orientation variants

$$f(\varphi_1, \varphi_2) = D + \frac{A}{2} (\varphi_1^2 + \varphi_2^2) - \frac{B}{3} (\varphi_1^3 + \varphi_2^3) + \frac{C}{4} (\varphi_1^2 + \varphi_2^2)^2. \quad (4.43)$$

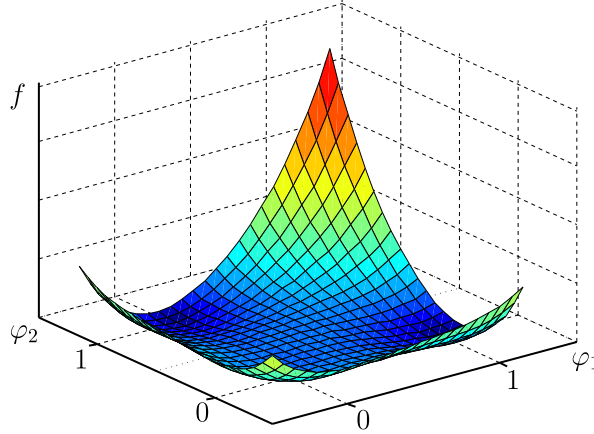


Figure 4.5: Landau polynomial $f(\varphi_i) = f(\varphi_1, \varphi_2)$

The plot of $f(\varphi_1, \varphi_2)$ in Figure 4.5 shows two absolute minima of value 0 at $(1, 0)$ and $(0, 1)$ corresponding to the stable phases for $T < T_0$, the first and the second martensitic variant, respectively. The local minimum of value 1 at $(0, 0)$ corresponds to the metastable austenitic phase. Thus, the energy landscape of the separation potential ensures that in each point only a single phase occurs.

To describe the evolution of each order parameter, two TDGL equations are necessary, where the variational derivatives of the phase field potential ψ in

4 An Elastic Phase Field Model for Martensitic Transformations

Eq. (4.38) with respect to φ_1 and φ_2 yield

$$\beta \dot{\varphi}_i = -\frac{\delta\psi}{\delta\varphi_i} = -\frac{\partial W}{\partial\varphi_i} - G \left(\frac{\kappa_{\text{sep}}}{L} \frac{\partial f}{\partial\varphi_i} - \kappa_{\text{grad}} L \Delta\varphi_i \right). \quad (4.44)$$

Since the elastic energy density enters the phase field potential ψ , the mechanical quantities come into play. These have to satisfy the balance of linear momentum in Eq. (2.22) which reduces to the equilibrium condition

$$\text{div } \boldsymbol{\sigma} = \mathbf{0} \quad (4.45)$$

for the Cauchy stress tensor $\boldsymbol{\sigma}$ if inertia effects and volume forces are neglected. The stresses are given by the constitutive relation in Eq. (4.12) with

$$\boldsymbol{\sigma} = \frac{\partial\psi}{\partial\boldsymbol{\varepsilon}} = \mathbb{C}(\varphi_i) (\boldsymbol{\varepsilon} - \boldsymbol{\varepsilon}_\varphi^0(\varphi_i)). \quad (4.46)$$

Since \mathbb{C} and $\boldsymbol{\varepsilon}^0$ depend on the order parameters, Eq. (4.44) and Eq. (4.45) represent a coupled non-linear time dependent boundary value problem. It is completed by the boundary conditions for the stresses and the displacements

$$\boldsymbol{\sigma} \mathbf{n} = \mathbf{t}^* \quad \text{on } \partial V_t, \quad (4.47)$$

$$\mathbf{u} = \mathbf{u}^* \quad \text{on } \partial V_u, \quad (4.48)$$

while concerning the order parameter

$$\xi_i^* = 0 \quad \text{on } \partial V, \quad \text{with } \boldsymbol{\xi}_i \cdot \mathbf{n} = \xi_i^* \quad (4.49)$$

is considered. The micro stresses $\boldsymbol{\xi}_i$ in Eq. (4.49) are defined according to Section 4.1.2 with $\boldsymbol{\xi}_i = \frac{\partial\psi}{\partial\nabla\varphi_i} = \kappa_{\text{grad}} G L \nabla\varphi_i$. To solve Eqs. (4.44), (4.45) the finite element method is employed, where the numerical implementation is discussed in the following section.

4.2.2 Numerical Implementation

In the literature, several approaches are proposed to solve the field equations of a phase field model for martensitic transformations. Chen et al. [1992] and Wang and Khachaturyan [1997], who introduced the first phase field models for martensitic transformations, used the fast Fourier transformation (FFT) formalism, which was also used in numerous further works, for example Jin et al. [2001], Artemev et al. [2000], Ahluwalia et al. [2004]. Under certain circumstances, e.g. the mechanical equilibrium can be solved very efficiently in Fourier space, see also the work of Hu and Chen [2001]. However, for considering complicated boundary conditions or complex material laws, especially with phase dependent material properties, the finite element method is more flexible. In the context of phase field modeling of

4.2 Phase Field Model for Multivariant Martensitic Transformations

the martensitic transformation it is applied for example by Hildebrand and Miehe [2011], Levitas et al. [2010], Yeddu et al. [2012], Malik et al. [2013], Levitas et al. [2013], Schmitt et al. [2013a]. Another alternative to solve the field equations is the finite difference method, see e.g. Yamanaka et al. [2008].

In the present work the finite element approach is employed, where this subsection summarizes the most important details concerning the numerical implementation of the model introduced above. For further background information on the finite element method the reader is referred to various textbooks e.g. Hughes [2000], Zienkiewicz and Taylor [2000], Wriggers [2001].

The phase field model is implemented into the finite element code FEAP with the displacements \mathbf{u} and the order parameters φ_1 and φ_2 as nodal degrees of freedom. Starting point for the numerical implementation are the field equations (4.44) and (4.45) with the corresponding boundary conditions. The scalar product of the field equations with arbitrary test functions $\delta\mathbf{u}$ and $\delta\varphi_i$ and the subsequent integration by parts over the volume V of the computation domain yields the *weak formulation* of the problem

$$\int_V \underbrace{(\nabla\delta\mathbf{u})^T : \boldsymbol{\sigma}}_{\delta\boldsymbol{\varepsilon} : \boldsymbol{\sigma}} dv = \int_{\partial V_i} \delta\mathbf{u} \cdot \mathbf{t}^* da, \quad (4.50)$$

and

$$\int_V - \left[\delta\varphi_i \beta \dot{\varphi}_i + \nabla\delta\varphi_i \cdot \boldsymbol{\xi}_i + \delta\varphi_i \left(\frac{\partial W}{\partial\varphi_i} + G \frac{\kappa_{\text{sep}}}{L} \frac{\partial f}{\partial\varphi_i} \right) \right] dv = 0, \quad \text{with } i = 1, 2. \quad (4.51)$$

For the spatial discretization the continuous volume V is divided into N_e *finite elements*, each of them occupying a domain Ω_e

$$V \approx V^h = \bigcup_{e=1}^{N_e} \Omega_e \quad (4.52)$$

where the element size corresponds to the mesh parameter h . The assembly operator \bigcup describes the assembly of the system. According to the *isoparametric concept*, the nodal degrees of freedom \mathbf{u} , φ_i and the geometry \mathbf{x} are approximated element by element by the same shape functions N_I of node I , where n_{el} is the total number of nodes per element,

$$\underline{\mathbf{u}}^h = \sum_{I=1}^{n_{\text{el}}} N_I \hat{\mathbf{u}}_I, \quad \varphi_i^h = \sum_{I=1}^{n_{\text{el}}} N_I \hat{\varphi}_{iI}, \quad \underline{\mathbf{x}}^h = \sum_{I=1}^{n_{\text{el}}} N_I \hat{\mathbf{x}}_I. \quad (4.53)$$

In Eq. (4.53) the approximated quantities have a superscript $(\cdot)^h$ while nodal quantities are indicated with a superposed hat ($\hat{\cdot}$). The *shape functions*, which interpolate

4 An Elastic Phase Field Model for Martensitic Transformations

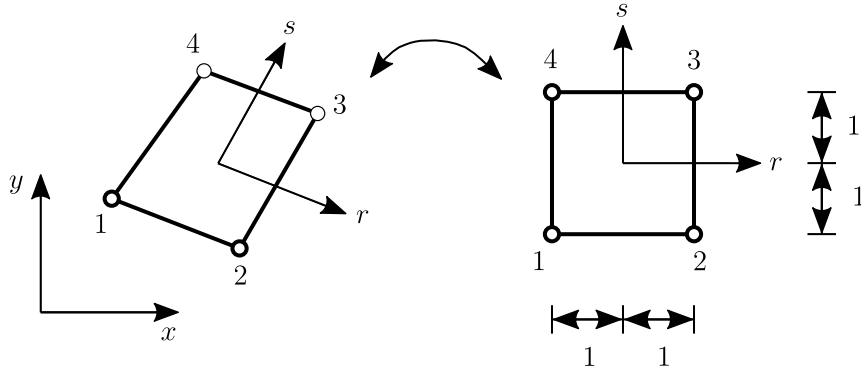


Figure 4.6: Isoparametric quadrilateral four-node element.

between the nodal values, are defined on a reference element $\bar{\Omega}_e$ in a r - s -coordinate system. In this work quadrilateral elements with $n_{el} = 4$ and bilinear shape functions

$$N_I(r, s) = \frac{1}{4} (r^2 + r_I r) (s^2 + s_I s) \quad (4.54)$$

are used where r_I and s_I are the local coordinates of node I corresponding to the right-hand side of Figure 4.6. Details on the computation of shape functions and derivatives can be found in any textbook on the finite element method, see for example Hughes [2000], Zienkiewicz and Taylor [2000], Wriggers [2001].

With introducing the two-dimensional differential operator matrices

$$\underline{\mathbf{B}}_I^u = \begin{bmatrix} N_{I,x} & 0 \\ 0 & N_{I,y} \\ N_{I,y} & N_{I,x} \end{bmatrix} \quad \text{and} \quad \underline{\mathbf{B}}_I^{\varphi_i} = \begin{bmatrix} N_{I,x} \\ N_{I,y} \end{bmatrix}, \quad (4.55)$$

the discretizations of the gradient quantities read

$$\underline{\boldsymbol{\varepsilon}}^h = \sum_{I=1}^{n_{el}} \underline{\mathbf{B}}_I^u \hat{\mathbf{u}}_I, \quad \underline{\nabla} \varphi^h = \sum_{I=1}^{n_{el}} \underline{\mathbf{B}}_I^{\varphi_i} \hat{\varphi}_{iI} \Rightarrow \underline{\boldsymbol{\xi}}_i^h = \kappa_{\text{grad}} GL \sum_{I=1}^{n_{el}} \underline{\mathbf{B}}_I^{\varphi_i} \hat{\varphi}_{iI}. \quad (4.56)$$

In Eq. (4.56) *Voigt notation* is applied for $\boldsymbol{\varepsilon}$ and $\boldsymbol{\xi}_i$, i. e.

$$\underline{\boldsymbol{\varepsilon}} = (\varepsilon_{xx}, \varepsilon_{yy}, 2\varepsilon_{xy})^T, \quad \underline{\boldsymbol{\xi}}_i = \kappa_{\text{grad}} GL (\varphi_{i,x}, \varphi_{i,y})^T, \quad (4.57)$$

4.2 Phase Field Model for Multivariant Martensitic Transformations

which is marked by the underline. The test functions and their gradients are discretized accordingly

$$\begin{aligned}\underline{\delta \mathbf{u}}^h &= \sum_{I=1}^{n_{\text{el}}} N_I \delta \hat{\mathbf{u}}_I, & \underline{\delta \boldsymbol{\varepsilon}}^h &= \sum_{I=1}^{n_{\text{el}}} \underline{\mathbf{B}}_I^u \delta \hat{\mathbf{u}}_I, \\ \underline{\delta \varphi}_i^h &= \sum_{I=1}^{n_{\text{el}}} N_I \delta \hat{\varphi}_{iI}, & \underline{\nabla \delta \varphi}_i^h &= \sum_{I=1}^{n_{\text{el}}} \underline{\mathbf{B}}_I^{\varphi_i} \delta \hat{\varphi}_{iI}.\end{aligned}\quad (4.58)$$

Applying the discretizations in Eqs. (4.53), (4.56), (4.58) to Eqs. (4.50),(4.51) allows constructing the approximations of the global weak forms by assembling the equations of all elements

$$\bigcup_{e=1}^{N_e} \sum_{I=1}^{n_{\text{el}}} (\underline{\delta \mathbf{u}}^h)^T \underbrace{\left[- \int_{\Omega_e} (\underline{\mathbf{B}}_I^u)^T \underline{\boldsymbol{\sigma}}^h \, dv + \int_{\partial \Omega_e \cap \partial \Omega_t} N_I \underline{\mathbf{t}}^{*h} \, da \right]}_{\underline{\mathbf{R}}_{e,I}^u} = 0 \quad (4.59)$$

$$\bigcup_{e=1}^{N_e} \sum_{I=1}^{n_{\text{el}}} \underline{\delta \varphi}_i^h \underbrace{\left[- \int_{\Omega_e} N_I \beta \dot{\varphi}_i^h \, dv - \int_{\Omega_e} \underline{\mathbf{B}}_I^{\varphi_i T} \underline{\boldsymbol{\xi}}_i^h \, dv - \int_{\Omega_e} N_I \left(\frac{\partial W^h}{\partial \varphi_i} + G \frac{\kappa_{\text{sep}}}{L} \frac{\partial f}{\partial \varphi_i} \right) \, dv \right]}_{\underline{\mathbf{R}}_{e,I}^{\varphi_i}} = 0. \quad (4.60)$$

The terms in squared brackets in Eq. (4.59) and Eq. (4.60) define the element residuals of node I

$$\underline{\mathbf{R}}_{e,I}^u = - \int_{\Omega_e} (\underline{\mathbf{B}}_I^u)^T \underline{\boldsymbol{\sigma}}^h \, dv + \int_{\partial \Omega_e \cap \partial \Omega_t} N_I \underline{\mathbf{t}}^{*h} \, da \quad (4.61)$$

$$\underline{\mathbf{R}}_{e,I}^{\varphi_i} = - \int_{\Omega_e} N_I \beta \dot{\varphi}_i^h \, dv - \int_{\Omega_e} \underline{\mathbf{B}}_I^{\varphi_i T} \underline{\boldsymbol{\xi}}_i^h \, dv - \int_{\Omega_e} N_I \left(\frac{\partial W^h}{\partial \varphi_i} + G \frac{\kappa_{\text{sep}}}{L} \frac{\partial f}{\partial \varphi_i} \right) \, dv. \quad (4.62)$$

To obtain the *element residuals* $\underline{\mathbf{R}}_e$ the corresponding nodal residuals are combined in a vector. For the quadrilateral element with $n_{\text{el}} = 4$, it reads

$$\underline{\mathbf{R}}_e = \begin{bmatrix} \underline{\mathbf{R}}_{e,1} \\ \underline{\mathbf{R}}_{e,2} \\ \underline{\mathbf{R}}_{e,3} \\ \underline{\mathbf{R}}_{e,4} \end{bmatrix} \quad \text{with} \quad \underline{\mathbf{R}}_{e,I} = \begin{bmatrix} \underline{\mathbf{R}}_{e,I}^u \\ \underline{\mathbf{R}}_{e,I}^{\varphi_i} \end{bmatrix}. \quad (4.63)$$

4 An Elastic Phase Field Model for Martensitic Transformations

As Eq. (4.59) and Eq. (4.60) must hold for arbitrary test functions the terms in squared brackets have to vanish, leading to the *residual equation*

$$\underline{\mathbf{R}}(\hat{\underline{\mathbf{d}}}, \hat{\underline{\mathbf{d}}}) = \bigcup_{e=1}^{N_e} \underline{\mathbf{R}}_e \stackrel{!}{=} \underline{\mathbf{0}}. \quad (4.64)$$

In Eq. (4.64), $\underline{\mathbf{R}} = \underline{\mathbf{R}}(\hat{\underline{\mathbf{d}}}, \hat{\underline{\mathbf{d}}})$ is the global residual vector which depends on the *nodal degrees of freedom* given by the global vector

$$\hat{\underline{\mathbf{d}}} = \begin{bmatrix} \hat{\underline{\mathbf{d}}}_1 \\ \vdots \\ \hat{\underline{\mathbf{d}}}_{N_n} \end{bmatrix} \quad \text{with} \quad \hat{\underline{\mathbf{d}}}_K = \begin{bmatrix} \hat{\underline{\mathbf{u}}}_K \\ \hat{\varphi}_{iK} \end{bmatrix}, \quad (4.65)$$

where the subscript $K = 1, \dots, N_n$ is the global node number.

In order to solve the residual equation (4.64) in each time step for $\hat{\underline{\mathbf{d}}}, \hat{\underline{\mathbf{d}}}$ an implicit time integration scheme is used. The discretization in time according to the *backward Euler method* yields for the time step t_n the relation

$$\hat{\underline{\mathbf{d}}} = \frac{\hat{\underline{\mathbf{d}}}_{n+1} - \hat{\underline{\mathbf{d}}}_n}{\Delta t}, \quad (4.66)$$

where $\hat{\underline{\mathbf{d}}}(t_n)$ is abbreviated with $\hat{\underline{\mathbf{d}}}_n$. For computing the solution $\hat{\underline{\mathbf{d}}}_{n+1}$, the *Newton-Raphson method* is applied which requires the linearization of the residual equation (4.64)

$$\underline{\mathbf{R}}^{(m+1)}(\hat{\underline{\mathbf{d}}}, \hat{\underline{\mathbf{d}}}) \approx \underline{\mathbf{R}}^{(m)}(\hat{\underline{\mathbf{d}}}, \hat{\underline{\mathbf{d}}}) + \underbrace{\frac{\partial \underline{\mathbf{R}}(\hat{\underline{\mathbf{d}}}, \hat{\underline{\mathbf{d}}})}{\partial \hat{\underline{\mathbf{d}}}} \Big|^{(m)}}_{-\underline{\mathbf{S}}^{(m)}} \Delta \hat{\underline{\mathbf{d}}}^{(m)} = \underline{\mathbf{0}}, \quad (4.67)$$

where the superscript $(\cdot)^{(m)}$ denotes the iteration step of the Newton-Raphson method. For the sake of clarity the time step index $(\cdot)_n$ is suppressed for not converged values. Quantities without the iteration superscript $(\cdot)^{(m)}$ represent converged values. With the definition of the *system matrix* $\underline{\mathbf{S}}^{(m)} = -\frac{\partial \underline{\mathbf{R}}(\hat{\underline{\mathbf{d}}}, \hat{\underline{\mathbf{d}}})}{\partial \hat{\underline{\mathbf{d}}}} \Big|^{(m)}$ the equation, which is solved, reads

$$\underline{\mathbf{S}}^{(m)} \Delta \hat{\underline{\mathbf{d}}}^{(m)} = \underline{\mathbf{R}}^{(m)}(\hat{\underline{\mathbf{d}}}^{(m)}, \hat{\underline{\mathbf{d}}}^{(m)}). \quad (4.68)$$

4.2 Phase Field Model for Multivariant Martensitic Transformations

while the solution is obtained by the subsequent algorithm

$$\begin{aligned}
 & \hat{\underline{d}}^{(0)} = \hat{\underline{d}}_n \\
 & \left. \begin{array}{l} \text{solve } \underline{\mathbf{R}}^{(m)} = \underline{\mathbf{S}}^{(m)} \Delta \hat{\underline{d}}^{(m)} \\ \text{update } \hat{\underline{d}}^{(m+1)} = \hat{\underline{d}}^{(m)} + \Delta \hat{\underline{d}}^{(m)} \end{array} \right\} \text{ until } \underline{\mathbf{R}}(\hat{\underline{d}}^{(m+1)}) \leq \text{TOL} \quad (4.69) \\
 & \Rightarrow \hat{\underline{d}}_{n+1} = \hat{\underline{d}}^{(m+1)}.
 \end{aligned}$$

Because the residual $\underline{\mathbf{R}}$ depends on $\underline{\mathbf{d}}$, $\hat{\underline{d}}$ the chain rule applies for the system matrix $\underline{\mathbf{S}}$

$$\underline{\mathbf{S}} \Delta \hat{\underline{d}} = - \underbrace{\frac{\partial \underline{\mathbf{R}}(\hat{\underline{d}})}{\partial \hat{\underline{d}}}}_{-\underline{\mathbf{K}}} \Delta \hat{\underline{d}} - \underbrace{\frac{\partial \underline{\mathbf{R}}(\hat{\underline{d}})}{\partial \hat{\underline{d}}}}_{-\underline{\mathbf{D}}} \underbrace{\frac{\partial \hat{\underline{d}}}{\partial \hat{\underline{d}}}}_{\frac{1}{\Delta t}} \Delta \hat{\underline{d}}, \quad (4.70)$$

$$\rightsquigarrow \underline{\mathbf{S}} = \underline{\mathbf{K}} + \frac{1}{\Delta t} \underline{\mathbf{D}}. \quad (4.71)$$

Within the finite element scheme the *stiffness matrix* $\underline{\mathbf{K}}$ and the *damping matrix* $\underline{\mathbf{D}}$ are calculated on the element level. The entries of the *element stiffness matrix* $\underline{\mathbf{K}}_{IJ,e}$ are given by

$$\underline{\mathbf{K}}_{IJ,e} = - \frac{\partial \underline{\mathbf{R}}_I}{\partial \hat{\underline{d}}_J} = \begin{bmatrix} \underline{\mathbf{K}}_{IJ,e}^{uu} & \underline{\mathbf{K}}_{IJ,e}^{u\varphi_1} & \underline{\mathbf{K}}_{IJ,e}^{u\varphi_2} \\ \underline{\mathbf{K}}_{IJ,e}^{\varphi_1 u} & \underline{\mathbf{K}}_{IJ,e}^{\varphi_1 \varphi_1} & \underline{\mathbf{K}}_{IJ,e}^{\varphi_1 \varphi_2} \\ \underline{\mathbf{K}}_{IJ,e}^{\varphi_2 u} & \underline{\mathbf{K}}_{IJ,e}^{\varphi_2 \varphi_1} & \underline{\mathbf{K}}_{IJ,e}^{\varphi_2 \varphi_2} \end{bmatrix}, \quad \text{with } I, J = 1, 2, \dots, n_{\text{el}} \quad (4.72)$$

where the matrix entries are calculated with

$$\begin{aligned}
 \tilde{\underline{\sigma}}_i^h &= \frac{\partial \underline{\mathbf{C}}}{\partial \varphi_i} (\underline{\boldsymbol{\varepsilon}}^h - \underline{\boldsymbol{\varepsilon}}_\varphi^0) \\
 \underline{\sigma}_i^{0,h} &= \underline{\mathbf{C}} \frac{\partial}{\partial \varphi_i} (\underline{\boldsymbol{\varepsilon}}^h - \underline{\boldsymbol{\varepsilon}}_\varphi^0) \quad (4.73)
 \end{aligned}$$

4 An Elastic Phase Field Model for Martensitic Transformations

as follows (for $i, j = 1, 2$)

$$\begin{aligned}
\underline{\mathbf{K}}_{IJ,e}^{uu} &= \frac{\partial \underline{\mathbf{R}}_{I,e}^u}{\partial \hat{\underline{\mathbf{d}}}_J} = \int_{\Omega_e} (\underline{\mathbf{B}}_I^u)^T \underline{\mathbf{C}} \underline{\mathbf{B}}_J^u \, dv \\
\underline{\mathbf{K}}_{IJ,e}^{u\varphi_i} &= \frac{\partial \underline{\mathbf{R}}_{I,e}^u}{\partial \hat{\varphi}_{i,J}} = \int_{\Omega_e} (\underline{\mathbf{B}}_I^u)^T \left(\tilde{\underline{\boldsymbol{\sigma}}}_i^h + \underline{\boldsymbol{\sigma}}_i^{0,h} \right) N_J \, dv \\
\underline{\mathbf{K}}_{IJ,e}^{\varphi_i u} &= \frac{\partial \underline{\mathbf{R}}_{I,e}^{\varphi_i}}{\partial \hat{\underline{\mathbf{d}}}_J} = \int_{\Omega_e} N_J \left(\tilde{\underline{\boldsymbol{\sigma}}}_i^h + \underline{\boldsymbol{\sigma}}_i^{0,h} \right) \underline{\mathbf{B}}_I^u \, dv \\
\underline{\mathbf{K}}_{IJ,e}^{\varphi_i \varphi_i} &= \frac{\partial \underline{\mathbf{R}}_{I,e}^{\varphi_i}}{\partial \hat{\varphi}_{i,J}} = \int_{\Omega_e} \kappa_{\text{grad}} G L (\underline{\mathbf{B}}_I^{\varphi_i})^T \underline{\mathbf{B}}_J^{\varphi_i} \, dv + \\
&\quad \int_{\Omega_e} N_I \left((\underline{\boldsymbol{\varepsilon}}_i^0)^T \left(\underline{\boldsymbol{\sigma}}_i^{0,h} + 2\tilde{\underline{\boldsymbol{\sigma}}}_i^h \right) + \kappa_{\text{sep}} \frac{G}{L} \frac{\partial^2 f}{\partial \varphi_i^2} \right) N_J \, dv \\
\underline{\mathbf{K}}_{IJ,e}^{\varphi_i \varphi_j} &= \frac{\partial \underline{\mathbf{R}}_{I,e}^{\varphi_i}}{\partial \hat{\varphi}_{j,J}} = \int_{\Omega_e} N_I \left(\tilde{\underline{\boldsymbol{\sigma}}}_i^h (\underline{\boldsymbol{\varepsilon}}_i^0 + \underline{\boldsymbol{\varepsilon}}_j^0) + \underline{\boldsymbol{\varepsilon}}_j^0 \underline{\boldsymbol{\sigma}}_i^{0,h} + \kappa_{\text{sep}} \frac{G}{L} \frac{\partial^2 f}{\partial \varphi_i \varphi_j} \right) N_J \, dv \quad (i \neq j).
\end{aligned}$$

The symmetry of the stiffness matrix arises due to the underlying variational principle. Furthermore, the entries of the *element damping matrix* $\underline{\mathbf{D}}_{IJ,e}$ read

$$\underline{\mathbf{D}}_{IJ,e} = -\frac{\partial \underline{\mathbf{R}}_{I,e}}{\partial \hat{\underline{\mathbf{d}}}_J} = \int_{\Omega_e} \begin{bmatrix} 0 & 0 & 0 & 0 \\ 0 & 0 & 0 & 0 \\ 0 & 0 & \beta N_I N_J & 0 \\ 0 & 0 & 0 & \beta N_I N_J \end{bmatrix} \, dv, \quad (4.74)$$

with $I, J = 1, 2, \dots, n_{\text{el}}$.

Using *Gauß quadrature* the integrals over the element domains are solved numerically in the parameter space of the reference element Ω_e . This requires the transformation of the integral

$$\int_{\Omega_e} \mathbf{G}(\mathbf{x}) \, dv = \int_{-1}^1 \int_{-1}^1 \overline{\mathbf{G}}(r, s) \det \mathbf{J}_e(r, s) \, dr \, ds. \quad (4.75)$$

4.2 Phase Field Model for Multivariant Martensitic Transformations

The Jacobian matrix \mathbf{J}_e links the line elements of the physical coordinates \mathbf{x} to the line elements of the r - s -coordinate system

$$\begin{bmatrix} N_{I,r} \\ N_{I,s} \end{bmatrix} = \underbrace{\begin{bmatrix} \frac{\partial x}{\partial r} & \frac{\partial y}{\partial s} \\ \frac{\partial x}{\partial r} & \frac{\partial y}{\partial s} \end{bmatrix}}_{\mathbf{J}_e} \begin{bmatrix} N_{I,x} \\ N_{I,y} \end{bmatrix}. \quad (4.76)$$

For the numerical integration Eq. (4.75) is approximated with

$$\int_{-1}^1 \int_{-1}^1 \overline{\mathbf{G}}(r, s) \det \mathbf{J}_e(r, s) \, dr \, ds \approx \sum_{q=1}^{n_q} \overline{\mathbf{G}}(r_q, s_q) \det \mathbf{J}_e(r_q, s_q) w_q, \quad (4.77)$$

where w_q are the weights and r_q, s_q are the coordinates of the Gaussian points to evaluate the term.

4.2.3 Input Parameters of Pure Iron from Atomistic Simulations

In the following, the parameters for the implemented phase field model are chosen, based on the results of the atomistic simulations of pure iron for two different temperatures $T_1 = 100$ K and $T_2 = 1300$ K. Due to the potential which is applied for the MD simulations the equilibrium temperature $T_0 = 825$ K is considered. Hence, T_0 is far away from both T_1 and T_2 . For the determination of the parameters only a single martensitic orientation variant with the order parameter φ is used, as the atomistic simulations do not distinguish between different martensite variants. With the atomic volumes given by MD for austenite and martensite, the lattice constants can be calculated due to the cubic crystal structures of both phases. For simplicity, the considerably small temperature dependence of the atomic volumes is neglected. With the lattice constants, the eigenstrain tensor ϵ^0 is determined according to Eq. (4.41) with

$$\epsilon^0 = \begin{bmatrix} -0.2217 & 0.0 \\ 0.0 & 0.1007 \end{bmatrix}. \quad (4.78)$$

Using the elastic constants of the austenite- and martensite-lattices resulting from MD simulations, effective Lamé parameters are calculated in agreement with Pimpinelli and Villain [1998]

$$\bar{\lambda} = \frac{1}{5}(\mathbb{C}_{11} + 4\mathbb{C}_{12} - 2\mathbb{C}_{33}), \quad \bar{\mu} = \frac{1}{5}(\mathbb{C}_{11} - \mathbb{C}_{12} + 3\mathbb{C}_{33}) \quad (4.79)$$

4 An Elastic Phase Field Model for Martensitic Transformations

which eventually yield the effective isotropic elasticity tensors in Voigt notation for the austenitic and the martensitic phase, respectively,

$$\bar{\mathbb{C}}_A = \begin{bmatrix} 221\,880 & 149\,840 & 0 \\ 149\,840 & 221\,880 & 0 \\ 0 & 0 & 36\,030 \end{bmatrix} \text{ MPa,}$$

$$\bar{\mathbb{C}}_M = \begin{bmatrix} 292\,700 & 106\,250 & 0 \\ 106\,250 & 292\,700 & 0 \\ 0 & 0 & 93\,220 \end{bmatrix} \text{ MPa.}$$

The characteristic interface energy density is calculated atomistically by Wang and Urbassek [2013] with $G = 0.96 \frac{\text{J}}{\text{m}^2}$. The parameter $L = 10 \text{ nm}$, is chosen sufficiently large, such that the transition zone can be resolved by several elements. In order to determine the coefficients A , B , C and D of the Landau polynomial in Eq. (4.43), the energy per atom is evaluated for the states the atom occupies during the martensitic transformation with MD simulations for $T_1 = 100 \text{ K}$ and $T_2 = 1300 \text{ K}$. These data are plotted in Figure 4.7, (black crosses) with the order parameter φ on the abscissa. The curves are normalized, such that the ordinate-value $f = 1$ for the local minimum. Thus, the black curve resulting from MD simulations corresponds to the Landau polynomial in Eq. (4.43) with $\varphi_1 = \varphi$, $\varphi_2 = 0$. Using least-square method (orange curves in Figure 4.7), the coefficients A , B , C and D are determined. For $T_1 = 100 \text{ K}$ ($T_1 < T_0$) the coefficient $D = 1$, while the orange curve in

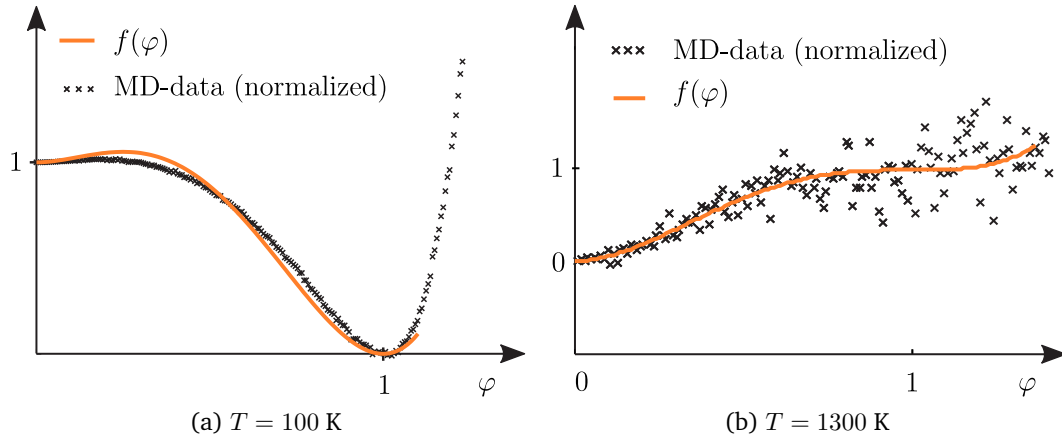


Figure 4.7: Normalized energy barrier resulting from MD (black crosses) with Landau polynomial $f(\varphi)$ (orange curve).

Figure 4.7(a) yields $A = 2.8$. The relations $B = 3A + 12 = 20.4$, $C = 2A + 12 = 17.6$ ensure the local minimum at $\varphi = 0$ and the global minimum at $\varphi = 1$, which corresponds to the metastable phase austenite and the stable phase martensite, respectively. The calibration constants are calculated according to Eq. (4.29) with $\kappa_{\text{sep}} = 2.637$ and $\kappa_{\text{grad}} = 1.450$. In order to determine the mobility parameter β ,

4.2 Phase Field Model for Multivariant Martensitic Transformations

these input data are used to simulate a two phase continuum with a length of 176.5 nm, discretized with 200 uniform elements in horizontal direction. The initial

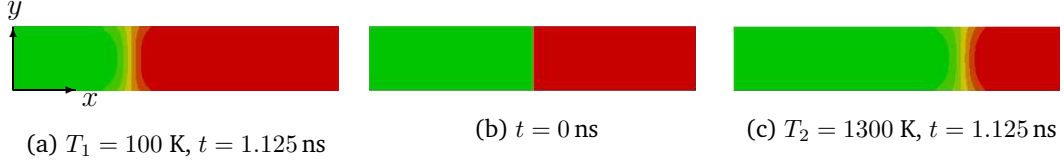


Figure 4.8: Interface motion of a two-phase beam (green: austenite, red: martensite).
 (b) Initial configuration. (a) $T_1 = 100$ K. (c) $T_2 = 1300$ K.

configuration can be seen in Figure 4.8(b): The left half of the beam is austenitic, depicted in green, the right half martensitic, depicted in red. The boundaries of the computation domain are stress free i.e. no external loads are applied. To avoid the rigid body movement, the bottom left corner is fixed in both the horizontal and vertical directions, and the bottom right corner is fixed in vertical direction. For $T_1 = 100$ K, Figure 4.7(a) indicates that martensite is the energetically more favorable stable phase. Concerning the energy of the initial configuration depicted in Figure 4.8(b), the eigenstrain ϵ^0 of the martensitic phase increases the elastic energy of the system while austenite has a contribution resulting from the separation potential ψ^{sep} . Additionally, the interface between the phases contributes to the gradient energy density ψ^{grad} . Hence, the system minimizes the global total energy by shifting the interface continuously to the left, where the eigenstrain within the martensite leads to a slightly curved interface (see Figure 4.8(a)). For the final state, a purely martensitic material, the total energy density $\psi = 0$. There is no contribution to the gradient energy density ψ^{grad} since there is no interface. In all points the order parameter $\varphi = 1$ such that the separation potential $\psi^{\text{sep}} = 0$ all over the computation domain. Furthermore, for a purely martensitic beam, the eigenstrain is compensated on the macroscopic level, leading to the elastic energy $W = 0$.

The velocity of the propagating interface is calculated according to Eq. (4.37) where the discretization of the configurational forces is discussed in Kuhn and Müller [2010], Kuhn [2013]. In this context, the comparison of the result obtained by Eq. (4.37) and the interface velocity derived by tracking the interface has ensured that the influence of the interface curvature is negligibly small. The interface velocity is scaled by the mobility parameter β , which is in Eq. (4.44) indirectly proportional to the time derivative of the order parameter $\dot{\varphi}$. In the next step, the mobility parameter β is calibrated such that the interface velocity v_{if} of the simulation is in accordance with the interface velocity given by MD simulations $v_{\text{if}}^{\text{MD}} = 24.2 \frac{\text{m}}{\text{s}}$. This is the case for $\beta = 0.238 \frac{\text{Ns}}{\text{m}^2}$.

This procedure is repeated for the temperature $T_2 = 1300$ K ($T_2 > T_0$). The energy per atom during the martensitic transformation is indicated with black crosses in Figure 4.7(b). It shows, that for $T_2 = 1300$ K austenite is the stable

4 An Elastic Phase Field Model for Martensitic Transformations

and martensite the metastable phase. The orange curve in Figure 4.7(b), resulting from the least square method, yields $A = 11.81$ while for $T_2 > T_0$ $D = 0$, $B = 3A - 12 = 23.43$ and $C = 2A - 12 = 11.62$. According to Eq. (4.29) the calibration constants are determined with $\kappa_{\text{sep}} = 2.164$ and $\kappa_{\text{grad}} = 2.408$. With these input data, again the two-phase beam, shown in Figure 4.8(b), is employed as initial configuration with no external loads applied. Using the same mobility parameter $\beta = 0.238 \frac{\text{Ns}}{\text{m}^2}$ than for the above simulation (for $T_1 = 100$ K), the resulting interface velocity for $T_2 = 1300$ K is $v_{\text{if}} = 29.33 \frac{\text{m}}{\text{s}}$. This value fits the velocity obtained from MD simulations $v_{\text{if}}^{\text{MD}} = 26.0 \frac{\text{m}}{\text{s}}$, which is interpreted as verification of the mobility constant β . As a result, for this simulation the mobility constant β hardly depends on the temperature.

Due to this finding a temperature dependent phase field potential for pure iron is introduced. Atomistic simulation results provide the energy per atom for the

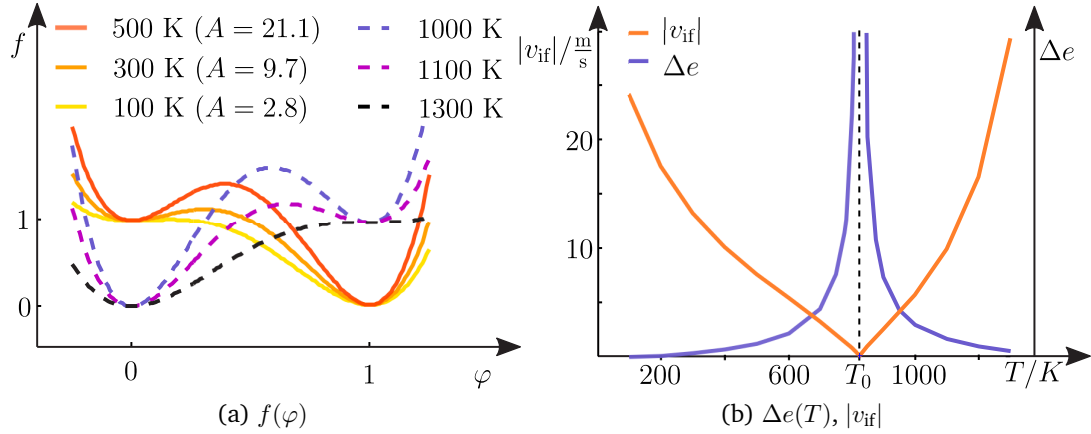


Figure 4.9: (a) Landau polynomial f for different temperatures. (b) Interface velocity and energy barrier as functions of temperature.

transformation path for several temperatures. Using these data the coefficients A and D in the Landau polynomial f in Eq. (4.43) are introduced as functions of the temperature T such that f can be calculated for a given T . Details concerning the determination of these functions are given in Schmidt [2015]. In Figure 4.9(a), the Landau polynomial f is plotted for some selected temperatures T . It can be seen that the energy barrier Δe increases when T approaches the equilibrium temperature at $T_0 = 825$ K. With increasing distance to T_0 the energy barrier gets smaller. This can also be seen in Figure 4.10, where f is plotted in dependence of both T and the order parameter φ . The relation between the energy barrier Δe and the temperature is clarified by Figure 4.9(b), where the purple curve shows Δe as a function of T . Since for the equilibrium temperature T_0 there is no spontaneous phase transition the energy barrier Δe achieves a very high value. To evaluate the influence of the temperature dependent Landau polynomial $f(\varphi, T)$ on the interface velocity, the two phase beam, depicted in Figure 4.8(b), is considered and v_{if} is

4.2 Phase Field Model for Multivariant Martensitic Transformations

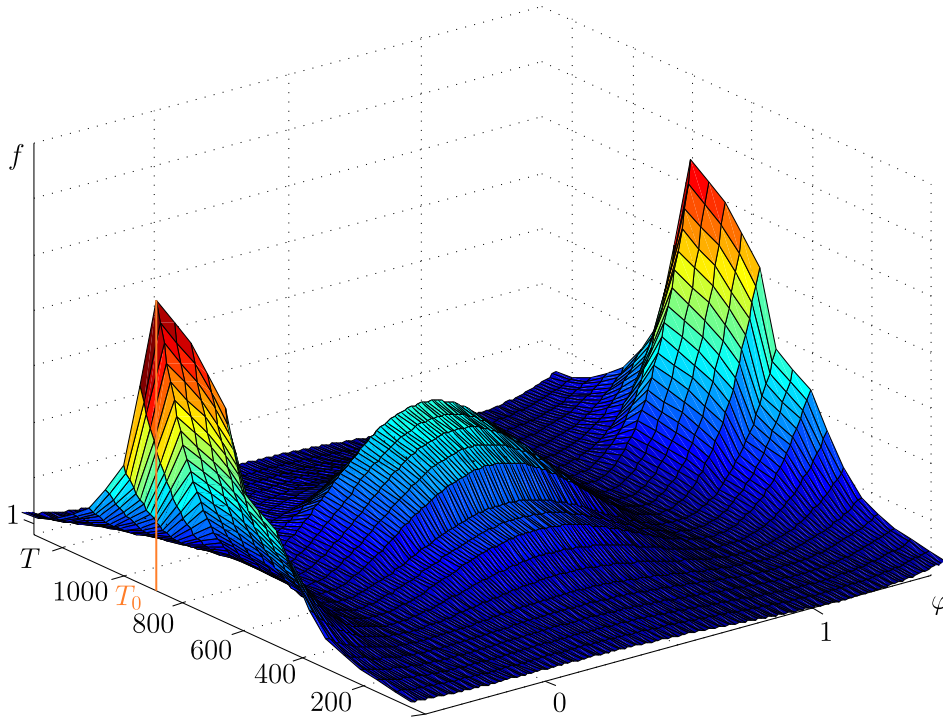


Figure 4.10: Landau polynomial $f(\varphi, T)$.

calculated for several temperatures. The resulting orange curve in Figure 4.9(b) shows the absolute value of v_{if} as a function of T^5 which is in agreement with the purple curve in Figure 4.9(b): A high energy barrier leads to a low interface velocity and vice versa. Hence, the energy barrier is an important feature characterizing the phase transition.

4.2.4 External Loads on a Two-Phase Beam

The material parameters derived for pure iron at $T = 100$ K are used to examine the correlation between an external load and the interface velocity. Therefore, the beam with the initial configuration depicted in Figure 4.8(b) is considered.

The eigenstrain ε^0 according to Eq. (4.78) corresponds to pressure in horizontal direction and tension in vertical direction. When the eigenstrain ε^0 is supported by applying pressure $\sigma^a = -23$ MPa in horizontal direction of the beam, the interface velocity $|v_{\text{if}}| = 25.1 \frac{\text{m}}{\text{s}}$ is higher than with no load applied (see above $|v_{\text{if}}| = 24.2 \frac{\text{m}}{\text{s}}$). In analogy, applying tension $\sigma^a = 23$ MPa in horizontal direction,

⁵For $T < T_0$ the interface propagates to the left resulting in a negative sign of v_{if} .

4 An Elastic Phase Field Model for Martensitic Transformations

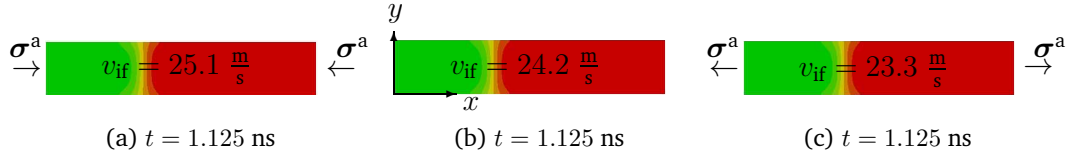


Figure 4.11: Interface motion for a two-phase beam with external load, green: austenite, red: martensite.

which works against the eigenstrain ε^0 , leads to a lower velocity $|v_{\text{if}}| = 23.3 \frac{\text{m}}{\text{s}}$. Thus, depending on the eigenstrain ε^0 , external loads affect the interface velocity v_{if} .

In the following, the influence of the transformation strain ε^0 is studied more detailed. Since the focus of this work is the material behaviour of metastable austenites, the material parameters of AISI 347 are taken into account. For future work, the cooperation with MD simulations is promoted. The proposed procedure could be repeated with considering further alloying elements for atomistic simulations such that the material parameters of steel are approximated.

4.3 Metastable Austenites

The mobility constant $\beta = 0.238 \frac{\text{Ns}}{\text{m}^2}$, which is calibrated in the previous section for pure iron, is used to investigate the processes on the microlevel of metastable austenitic steels. Here, temperatures below the equilibrium temperature are focused. Due to the cooling with carbon dioxide snow during the process of cryogenic turning a maximum temperature of the workpiece of about $T = 350$ K is obtained. This is far away from the equilibrium temperature T_0 of AISI 347 which lies between 800 K and 1200 K. Concerning the coefficients in the Landau polynomial in Eq. (4.43) this yields $D = 1$. So far, for AISI 347 no data from atomistic simulation are available. The value $A = 5.16$ is chosen which corresponds to the energy barrier of pure iron for about $T \approx 175$ K. With $A = 5.16$, the coefficients B and C can be calculated with $B = 3A + 12 = 27.48$ and $C = 2A + 12 = 22.32$. Using Eq. (4.29) the calibration constants are determined with $\kappa_{\text{sep}} = 2.114$ and $\kappa_{\text{grad}} = 1.474$. Hence, the parameter $L = 3.5$ nm controls the width of the transition zone. In comparison to the material parameters of pure iron, a smaller value is chosen since the model should be able to resolve the fine microstructures of austenitic steels. Furthermore, the parameter $G = 0.1 \frac{\text{J}}{\text{m}^2}$ corresponds to the interface energy density. This value lies within the range of the free energy densities of other phase field models, e.g. Schrade et al. [2009]. For the elasticity constants of austenite, the values of the comparable mono-crystalline AISI 316 according to Ledbetter [1985], Skorupski et al. [2014] are applied where the coordinate system of the proposed tensor is rotated by 45° . Quantities of the rotated coordinate system are indicated with $(\cdot)^*$.

Martensite is assumed to be ten percent stiffer than austenite

$$\underline{\mathbf{C}}_A^* = \begin{bmatrix} 2.87 & 0.53 & 0 \\ 0.53 & 2.87 & 0 \\ 0 & 0 & 1.17 \end{bmatrix} 10^5 \text{ MPa}, \quad \underline{\mathbf{C}}_M^* = 1.1 \mathbf{C}_A^*. \quad (4.80)$$

Two different martensitic orientation variants are considered by using the order parameters φ_1 and φ_2 . For the eigenstrain tensors of the two variants, Yamanaka et al. [2008] propose

$$\boldsymbol{\varepsilon}_1^0 = \begin{bmatrix} \varepsilon_{\text{vol}}^0 & -0.1 \\ -0.1 & \varepsilon_{\text{vol}}^0 \end{bmatrix}, \quad \boldsymbol{\varepsilon}_2^0 = \begin{bmatrix} \varepsilon_{\text{vol}}^0 & 0.1 \\ 0.1 & \varepsilon_{\text{vol}}^0 \end{bmatrix}, \quad (4.81)$$

where Yamanaka and coworkers assume $\varepsilon_{\text{vol}}^0 = 0$. Rotating the coordinate system of the eigenstrain tensor by 45° yields

$$\boldsymbol{\varepsilon}_1^{0*} = \begin{bmatrix} \varepsilon_{\text{vol}}^0 + 0.1 & 0 \\ 0 & \varepsilon_{\text{vol}}^0 - 0.1 \end{bmatrix}, \quad \boldsymbol{\varepsilon}_2^{0*} = \begin{bmatrix} \varepsilon_{\text{vol}}^0 - 0.1 & 0 \\ 0 & \varepsilon_{\text{vol}}^0 + 0.1 \end{bmatrix}. \quad (4.82)$$

The volumetric eigenstrain $\varepsilon_{\text{vol}}^0$ is specified below. For the simulations in this section the rotated $(\cdot)^*$ -coordinate system is used for the eigenstrain- and elasticity tensors.

The eigenvalues for the eigenstrain tensor in Eq. (4.82) are given in Eq. (3.5) while the eigenvectors coincide with the coordinate axes in Figure 4.12. This results with Eq. (3.3) in the habit plane normal directions for an austenite-martensite-interface

$$\mathbf{n}_{1\pm}^{\varepsilon^*} = \frac{1}{\sqrt{0.2}} \begin{bmatrix} -\sqrt{0.1 + \varepsilon_{\text{vol}}^0} \\ \pm\sqrt{0.1 - \varepsilon_{\text{vol}}^0} \end{bmatrix}, \quad \mathbf{n}_{2\pm}^{\varepsilon^*} = \frac{1}{\sqrt{0.2}} \begin{bmatrix} \pm\sqrt{0.1 - \varepsilon_{\text{vol}}^0} \\ -\sqrt{0.1 + \varepsilon_{\text{vol}}^0} \end{bmatrix}. \quad (4.83)$$

With the eigenvalues in Eq. (3.6) the habit plane normal directions for a martensite-martensite interface read according to Eq. (3.3)

$$\mathbf{n}_+^{\Delta\varepsilon^*} = \frac{1}{\sqrt{2}} \begin{bmatrix} -1 \\ -1 \\ 0 \end{bmatrix}, \quad \mathbf{n}_-^{\Delta\varepsilon^*} = \frac{1}{\sqrt{2}} \begin{bmatrix} 1 \\ -1 \\ 0 \end{bmatrix}. \quad (4.84)$$

4.3.1 Volumetric Eigenstrain and Orientation Variants

In a first example a quadratic matrix with an edge length of $a = 176.5$ nm is modeled, discretized with 200×200 uniform elements. The size and the discretization of the computation domain is henceforth applied unless otherwise specified. The initial configuration is depicted in Figure 4.12: The austenitic matrix contains a single circular nucleus (with a diameter of $0.2a$) of variant 1 martensite, where

4 An Elastic Phase Field Model for Martensitic Transformations

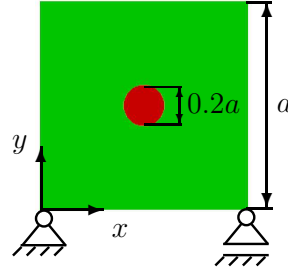


Figure 4.12: Initial configuration and boundary conditions. Austenite: green, martensite: red.

$\varphi_1 = 1$. The circular shape does not predetermine a growing direction of the martensite.

The resulting evolution of the martensitic phase with no external loads applied can be seen in Figure 4.13. In the following, austenite is depicted in green ($\varphi_1 = \varphi_2 = 0$), the first martensitic orientation variant in red ($\varphi_1 = 1$) and the second variant in blue ($\varphi_2 = 1$). The nucleus increases the elastic energy density W

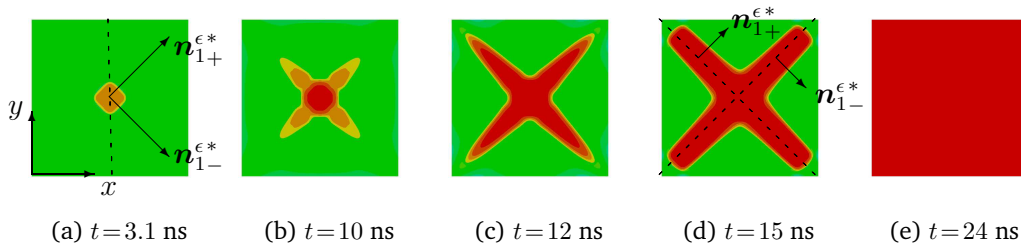


Figure 4.13: Austenitic (green) matrix with preexisting circular nucleus. Evolution of the martensitic phase (martensite 1: red) for $\epsilon_{\text{vol}}^0 = 0$.

due to the eigenstrain ϵ^0 within the martensite. Therefore, Figure 4.13(a) shows the nucleus initially shrinking i.e. $\varphi_1 \rightarrow 0$ in the area of the nucleus. This decreases the eigenstrain and thus the elastic energy density. Yet, concerning the energy contribution of the separation potential the martensitic phase is more favourable because of the global minimum of the Landau polynomial at $\varphi_1 = 1$. The subsequent microstructure evolution depends on which part of the local energy ψ is minimized. If the size of the nucleus is too small, the nucleus vanishes (which minimizes the elastic energy), resulting in a purely austenitic matrix. The critical size of the nucleus depends on the energy barrier i.e. on the temperature. For a higher energy barrier a bigger nucleus is necessary, cf. Schmitt et al. [2013a]. Here, the nucleus is above the critical size. The system starts to minimize the separation potential instead of the elastic energy, leading to a growing nucleus. Furthermore, the eigenstrain turns the circular nucleus into a square (see Figure 4.13(a)). The plane interface between the phases fits to the normal directions $\mathbf{n}_{1+}^{\epsilon^*}$ and $\mathbf{n}_{1-}^{\epsilon^*}$ of the habit planes, which are indicated in Figure 4.13(a), forming a right angle. The

4.3 Metastable Austenites

vectors $\mathbf{n}_{1+}^{\epsilon^*}$ and $\mathbf{n}_{1-}^{\epsilon^*}$ result from evaluating Eq. (4.83) with $\epsilon_{\text{vol}}^0 = 0$. Starting from the nucleus the martensite grows diagonally in the $\mathbf{n}_{1+}^{\epsilon^*}$ - and $\mathbf{n}_{1-}^{\epsilon^*}$ -directions. When it has propagated through the matrix, it broadens in habit plane normal directions which finally results in a continuous variant 1 martensite phase, corresponding to the local energy density $\psi = 0$, (see Section 4.2). The second martensitic orientation variant is not built.

In the next step the volumetric eigenstrain $\epsilon_{\text{vol}}^0 = 0.04$ is considered which accounts for the volume change due to the phase transformation. The resulting evolution of the phases for the same initial configuration (depicted in Figure 4.12) is shown in Figure 4.14. In comparison to the results in Figure 4.13 (with $\epsilon_{\text{vol}}^0 = 0$),

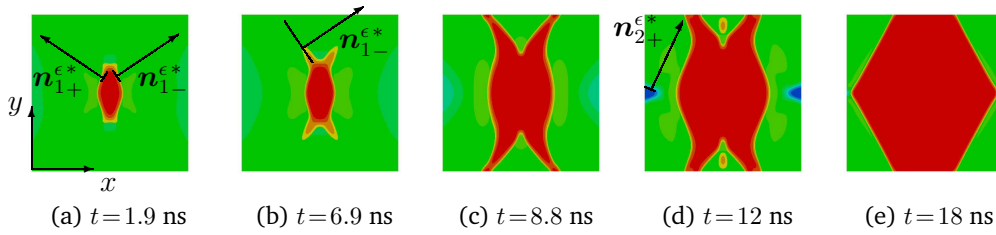


Figure 4.14: Austenitic (green) matrix with preexisting circular nucleus. Evolution of the martensitic phases (martensite 1: red, martensite 2: blue) for $\epsilon_{\text{vol}}^0 = 0.04$.

the volumetric eigenstrain $\epsilon_{\text{vol}}^0 = 0.04$ changes the eigenvalues of ϵ^0 leading to new habit plane normal directions $\mathbf{n}_{1+}^{\epsilon^*}$ and $\mathbf{n}_{1-}^{\epsilon^*}$ which are indicated in Figure 4.14(a). With the direction of the interface in accordance with $\mathbf{n}_{1+}^{\epsilon^*}$ and $\mathbf{n}_{1-}^{\epsilon^*}$, the variant 1 martensite nucleus starts to grow in a plate-like shape. This shape of the martensitic inclusion minimizes the elastic energy density in agreement with the work of Eshelby [1957]. Furthermore, the formation of plate-shaped martensite is experimentally observed. So evidently, the volumetric part of the eigenstrain tensor ϵ^0 should be taken into account for modeling the martensitic transformation. In the following, the evolving martensite splits up into a cross-like structure such that the new martensitic plates evolve in $\mathbf{n}_{1+}^{\epsilon^*}$ and $\mathbf{n}_{1-}^{\epsilon^*}$ -directions. When the plates have propagated through the matrix, it is deformed according to the eigenstrain ϵ_1^{0*} of the variant 1 martensite. The dominant shear part of ϵ_1^{0*} corresponds to compression parallel to the vertical edges and tension parallel to the horizontal edges of the quadratic specimen. This deformation is compensated by the eigenstrain of the second martensitic variant corresponding to compression in horizontal direction and tension in vertical direction. This can be seen in Figure 4.14(d) where the habit plane normal directions of variant 2 martensite $\mathbf{n}_{2+}^{\epsilon^*}$ and $\mathbf{n}_{2-}^{\epsilon^*}$ are indicated, too. In the following time steps, the second variant retreats due to the growing variant 1 plate. Eventually a continuous phase of the first martensitic orientation variant remains.

For comparison, in Figure 4.15 the simulation results are shown, starting from

4 An Elastic Phase Field Model for Martensitic Transformations

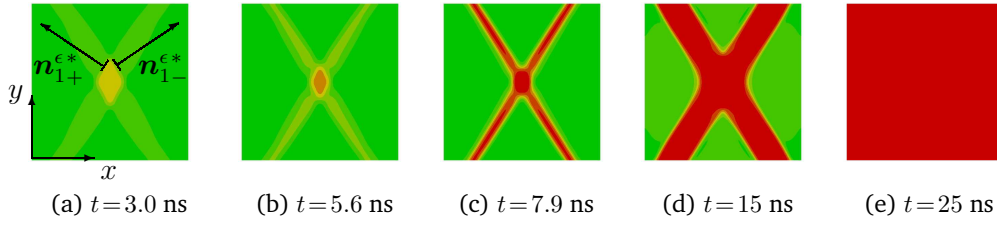


Figure 4.15: Austenitic (green) matrix with preexisting circular nucleus, single variant considered. Evolution of the martensitic phase (red) for $\epsilon_{\text{vol}}^0 = 0.04$.

the initial configuration in Figure 4.12, with only the first martensitic orientation variant considered. In Figure 4.15(a) the nucleus decreases more than in Figure 4.14(a), since in the above simulation martensite 2 forms besides the variant 1 nucleus which reduces the initial elastic energy due to the opposite signs of $\epsilon_{\text{shear}1}^0$ and $\epsilon_{\text{shear}2}^0$. For the two-dimensional case, this initial formation of the second variant does not nucleate but rebuilds after some time steps and is therefore not visible in Figure 4.14(a). Although, it leads to the fact that for considering two variants the martensitic phase nucleates at a smaller initial inclusion. In Figure 4.15(b) two diagonal slim strips of martensite are built in accordance with the calculated habit plane normal directions $\mathbf{n}_{1+}^{\epsilon^*}$ and $\mathbf{n}_{1-}^{\epsilon^*}$. The subsequent broadening of the martensitic formation results in a purely martensite 1 specimen.

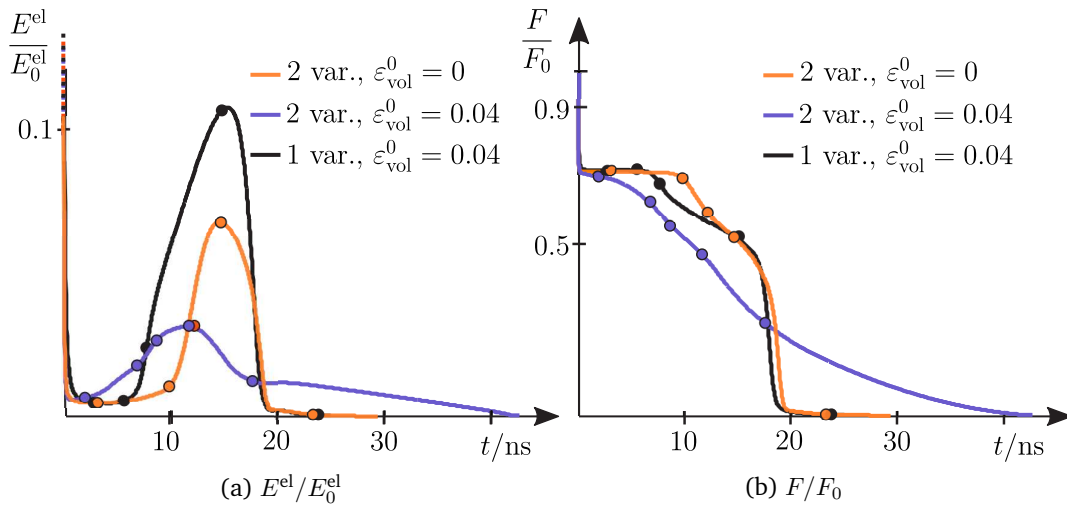


Figure 4.16: Evolution of the global energies E^{el} , F , referring to the global energy of the initial configuration E_0^{el} , F_0 .

Figure 4.16(a) shows the evolution of the global elastic energy $E^{\text{el}} = \int_V W \, dv$ for the above simulations with $\epsilon_{\text{vol}}^0 = 0$ (orange curve), with $\epsilon_{\text{vol}}^0 = 0.04$ for two variants (purple curve) and $\epsilon_{\text{vol}}^0 = 0.04$ for a single variant (black curve), referring to the global elastic energy of the initial configuration E_0^{el} (with $\epsilon_{\text{vol}}^0 = 0.04$). The

time steps of the microstructures depicted in Figures 4.13, 4.14 and 4.15 are marked with circles. The elastic energy density W is part of the local energy density in Eq. (4.38). Due to the eigenstrain of the circular nucleus the elastic energy at $t = 0$ is very high for all three simulations. It is considerably reduced by the initial relaxation of the system (which is illustrated in Figure 3.2). For further reduction of the high elastic energy the nucleus initially shrinks in all three simulations, leading to a minimum for the curves in Figure 4.16(a). After the minimum the orange curve ($\varepsilon_{\text{vol}}^0 = 0$) increases with a small slope. The martensitic phase nucleates as in the area of the nucleus the order parameter recovers, i.e. $\varphi \rightarrow 1$. After approximately 10 ns the orange curve increases strongly when the martensite starts to grow in diagonal directions (cf. Figure 4.13(b)), which coincide with the habit plane normal directions. These correspond to the main shear directions of ε^0 . The peak of the orange curve is reached when the martensitic plates have grown in diagonal direction through the specimen. As a result, the matrix is consequently deformed almost homogeneously by the pure shear strain within the martensite, which reduces the elastic energy in the following. During the broadening of the plates, the elastic energy decreases until $E^{\text{el}} = 0$ corresponding to a purely martensite 1 matrix.

The black curve (single variant) has a higher maximum since the additionally considered volumetric eigenstrain $\varepsilon_{\text{vol}}^0 = 0.04$ increases the elastic energy. The changed habit plane normal directions cause that the growing directions of the martensite do no longer coincide with the diagonal directions of the specimen. When the plates have propagated through the matrix there are still high stresses besides the martensitic formation. The elastic energy keeps on increasing until the plates have broadened almost to the corners of the specimen, which finally allows the compensation of the eigenstrain (cf. Figure 4.15(d)).

The purple curve increases first after the minimum because initially both variants are formed. The smaller slope between the first two circles (from 1.9 ns to 6.9 ns) corresponds to the martensite growing in a plate like shape (cf. Figure 4.14(a)). The branching of the initial plate increases the slope until the martensitic phase reaches the boundary, which is marked by a circle at $t = 8.8$ ns (cf. Figure 4.14(c)). Then the plates broaden in habit plane normal directions while the purple curve obtains the maximum when the second variant forms. This reduces in the following the total deformation and thus the elastic energy. For $t = 18$ ns the slope of the curve decreases. In this regard, Figure 4.14(e) shows that, due to the growing variant 1 plate, the martensite 2 has vanished. Thus, the formation of the second variant contributes to the energy reduction of the system. Despite the higher eigenstrain the purple curve has the lowest maximum of the three curves.

For $\varepsilon_{\text{vol}}^0 = 0$ the second variant is not built. The habit plane normal directions form a right angle such that these coincide with the habit plane normal directions of the second variant. Hence, variant 2 martensite can only be formed in

4 An Elastic Phase Field Model for Martensitic Transformations

the same direction or perpendicular to variant 1. This is a restriction compared to the habit plane normal directions corresponding to $\varepsilon_{\text{vol}}^0 = 0.04$: Both pairs $\mathbf{n}_{1+}^{\varepsilon^*}$, $\mathbf{n}_{1-}^{\varepsilon^*}$ and $\mathbf{n}_{2+}^{\varepsilon^*}$, $\mathbf{n}_{2-}^{\varepsilon^*}$ show different angles leading to more possibilities for an energy minimizing microstructure.

Figure 4.16(b) shows the total global energy $F = \int_V \psi \, dv$ as a function of simulation time. During the formation of the microstructures for $t < 20$ ns the purple curve (both variants, $\varepsilon_{\text{vol}}^0 = 0.04$) is below the black and the orange curves (single variant and $\varepsilon_{\text{vol}}^0 = 0$). Since all simulations start from the same initial configuration in Figure 4.12, this indicates that for these examples considering the volume change and two orientation variants minimizes the energy most effectively. The large interface areas of the microstructures in Figure 4.15(d) and Figure 4.13(d) cause the eventual steeper decrease of the black and the orange curve. The broadening of these structures results quicker in a purely martensitic specimen than the formation in Figure 4.14(e).

Evidently, the volume change and multiple orientation variants are crucial for modeling the martensitic transformation. Henceforth, two martensite variants and $\varepsilon_{\text{vol}}^0 = 0.04$ are considered.

4.3.2 External Loads

During the process of cryogenic turning the workpiece is exposed to high mechanical loads. Next, the influence of homogeneous load cases on the microstructure evolution is studied, starting with tension in horizontal direction. In Figure 4.17(a)

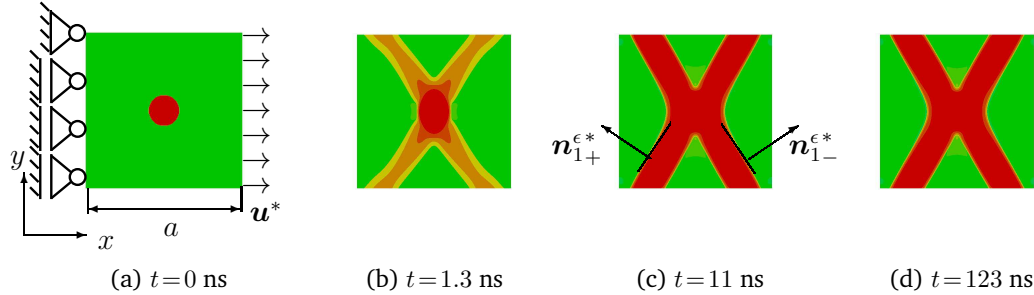


Figure 4.17: Austenitic (green) specimen with martensite 1 nucleus. Evolution of the martensitic phases (martensite 1: red, martensite 2: blue) for applying tension in horizontal direction.

the corresponding Dirichlet boundary conditions are illustrated together with the initial configuration, a circular martensite 1 nucleus in an austenitic matrix. During the simulation time, $u_x^* = 0.05a$ is held constant. The resulting microstructure is depicted in Figures 4.17(b)-(d). The external load corresponds to the eigenshear of the first variant. Thus, due to the load, martensite 1 is induced much faster compared to the above simulations without load applied. The load increases

the elastic energy, which can be reduced by the cross-formation of martensite 1 depicted in Figure 4.17(c). A further broadening of the plates would lead to higher deformations, increasing the elastic energy. Therefore, this microstructure remains unchanged and the second variant is not built. The vectors $\mathbf{n}_{1+}^{\epsilon^*}$, $\mathbf{n}_{1-}^{\epsilon^*}$ are indicated in Figure 4.17(c), showing that these are not influenced by the homogeneous loading since the difference between the states of strain of the austenitic matrix and the martensitic inclusions is still the same than without load applied.

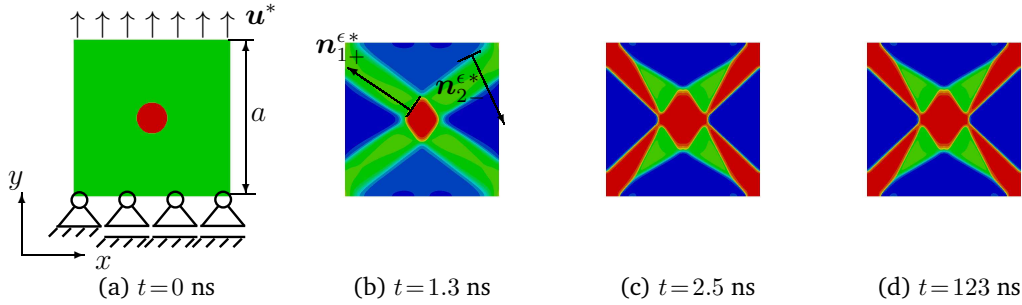
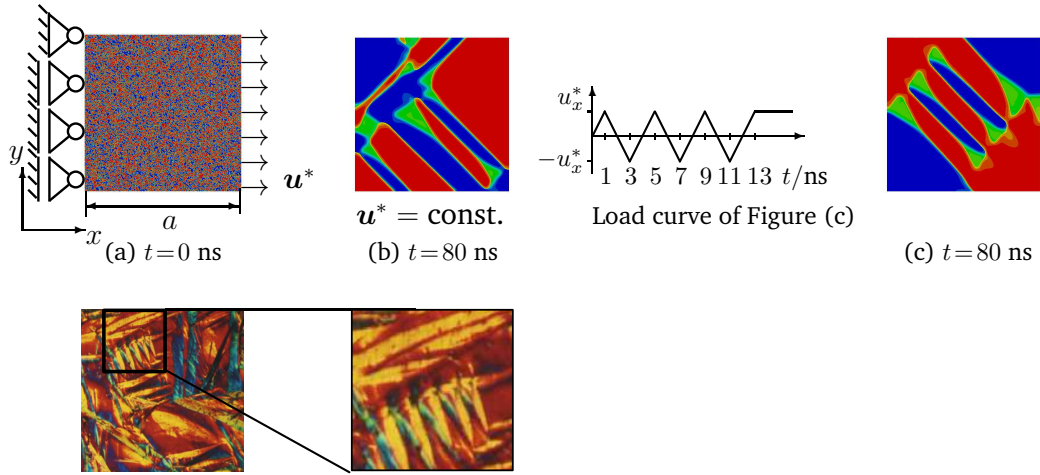


Figure 4.18: Austenitic (green) specimen with martensite 1 nucleus. Evolution of the martensitic phases (martensite 1: red, martensite 2: blue) for applying tension in vertical direction.

In Figure 4.18 the evolving phases for applying tensile stress in vertical direction can be seen. The external load supports the eigenstrain ϵ_2^0 of the second martensitic orientation variant, which corresponds to compression in horizontal direction and tension vertical direction. For a martensite 2 nucleus, in analogy to Figure 4.17, a cross-like structure of martensite 2 plates forms. For the nucleus of the 1st variant in Figure 4.18 the circular nucleus turns into a plate in accordance with the habit plane normal directions. In the remaining part of matrix martensite 2 forms almost instantaneously, except two stripes in diagonal directions, which are left austenitic, see Figure 4.18(b). Thereupon, martensite 1 evolves in the austenitic stripes from the central plate to the boundaries. The interface between martensite 1 and martensite 2 is built in diagonal direction of the matrix according to Eq. (4.84).

Starting from a single nucleus, where the martensitic phases can evolve freely within pure austenite, allows gaining a better understanding for the correlations. However, in a real microstructure there are various nucleation sites leading to complex interactions. This motivates another initial configuration shown in Figure 4.19(a). In each point the value of one (randomly chosen) order parameter is randomly chosen with $\varphi_i \in [0, 1]$ while the second order parameter is set to zero. In the following four simulations the same initial configuration is used. First, the horizontal displacement is specified where $u_x^* = 0.05a$. Using this numerical setup two different simulations are employed. Figure 4.19(b) results from a constant loading while in the second simulation u_x^* changes the sign for $t < 13$ ns and is held constant for $t > 13$ ns. In Figure 4.19(c) the load curve is depicted together with

4 An Elastic Phase Field Model for Martensitic Transformations



(d) Micrograph of a martensitic microstructure, Bhadeshia [2015]

Figure 4.19: Evolution of the martensitic phase for applying (longterm) tension in horizontal direction, starting from randomly distributed order parameters. Martensite 1: red, martensite 2: blue, austenite: green.

the resulting microstructure. Due to the load, a part of the randomly distributed nucleation sites form martensitic plates of both variants, which are arranged in a laminar-like structure. The constant load supports the eigenstrain of the first martensitic orientation variant ϵ_1^0 such that variant 1 martensite dominates. The volume fractions of the martensitic phases in Figure 4.19(b) are 52 % for martensite 1 and 38 % for martensite 2, so there is little retained austenite. The habit plane normal directions between the two martensite variants coincide with the diagonal directions of the specimen in accordance with Eq. (4.84). In Figure 4.19(c), which is the resulting microstructure of the cyclic loading, there are five martensite plates of alternating variants in diagonal directions in the center of the specimen while in the corners larger martensite areas are formed. The different microstructure compared to Figure 4.19(b) is caused by the changes in sign of the load. Each of them leads to the reformation of the phases. Finally, for $t > 13$ ns solely tension in horizontal direction is applied. The compression applied afore in horizontal direction supports the eigenstrain of martensite 2. Nevertheless, the martensite content of the phases for $t = 80$ ns in Figure 4.19(c) is the same as in Figure 4.19(b) (martensite 1 is 52 % and martensite 2 is 38 %). Furthermore, due to the more "realistic" initial configuration, the results in Figures 4.19(b), (c) resemble qualitatively the real microstructure which is depicted in the micrographs in Figure 4.19(d).

Figure 4.20(a) shows the evolution of the global total energy F as a function of the simulation time for the simulations in Figure 4.17 (black curve), Figure 4.19(b) (purple curve) and Figure 4.19(c) (orange curve). In order to obtain comparable results, the values are referred to F_0 , which is the total global energy of

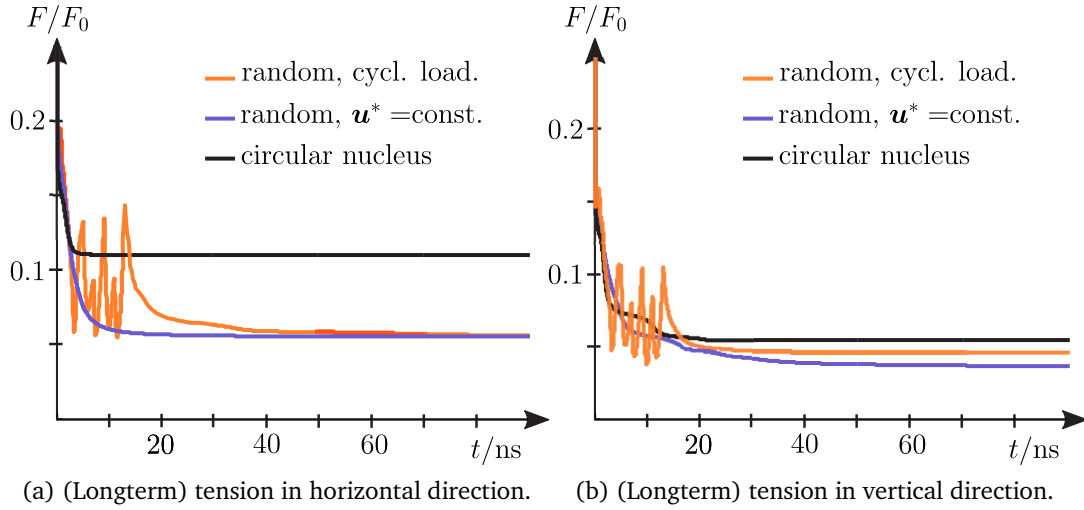


Figure 4.20: Evolution of the global total energy F , referring to the global energy of the initial configuration F_0 in Figure 4.17(a).

the initial configuration depicted in Figure 4.17(a). For all three simulations tensile stress in horizontal direction with $u_x^* = 0.05a$ is applied. Differing from the results in the previous section, where all simulations end up in a continuous martensitic matrix, here multiple martensitic plates are formed. All three simulations minimize the global energy until an equilibrium state is reached. The lower martensite content of 40 % in Figure 4.20(a) leads to a higher separation energy, such that the black curve is clearly above the other two curves. The laminate-like structures of martensitic plates in Figures 4.19(b),(c), which both have a total martensite content of 90 %, lead to a lower total energy. Since for the black and the purple curve the same load is applied, the final equilibrium state depends on the initial configuration.

Furthermore, the orange curve in Figure 4.20(a) has a zigzag profile corresponding to the load function. It can be seen that the maxima of the compression are below the maximal values of the tensile loading, which results from the volumetric part of the eigenstrain. It has a positive sign in both martensitic phases and thus reduces the compressive part of the eigenstrain. For the black and the purple curve, the same initial configuration is applied, while the load history differs. This influences the formation of the phases. Yet, the martensite content and the global total energy of the purple and the orange curve are approximately the same. In a next step tension in vertical direction is studied.

Starting from the same randomly distributed initial configuration the results for constant and cyclic loading with tensile stress in vertical direction are shown in Figures 4.21(b) and (c). Again, the volume fractions of the phases coincide for both simulations. With a martensite 1 content of 38 % and martensite 2 content of 52 % the same values as for tension in horizontal direction are obtained. In contrary to

4 An Elastic Phase Field Model for Martensitic Transformations

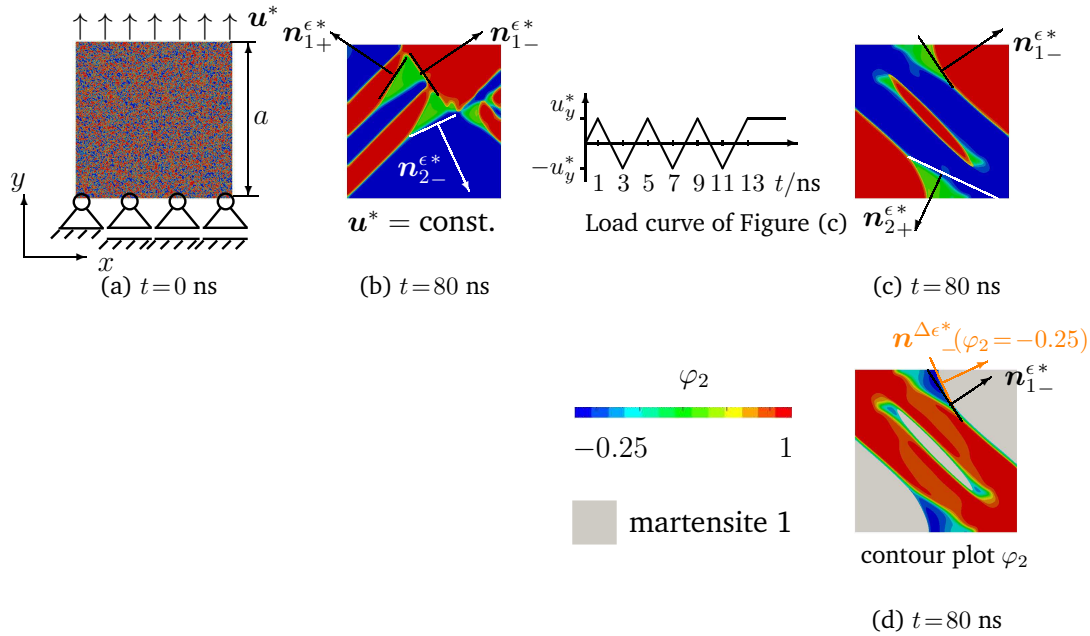


Figure 4.21: Evolution of the martensitic phase for applying (longterm) tension in vertical direction. Martensite 1: red, martensite 2: blue, austenite: green.

the above example, martensite 2 dominates since tension in horizontal direction corresponds to ϵ_2^{0*} . The evolution of the total global energy F referring to F_0 can be seen in Figure 4.20(b) (purple and orange curves) where also the simulation in Figure 4.18 (black curve) is considered. The higher martensite content of 80 % in Figure 4.18 compared to a martensite content of 40 % of the single nucleus in Figure 4.17 leads to a lower final total energy of the black curve in Figure 4.20(b) compared to the black curve in Figure 4.20(a).

Notable is the difference in energy between the orange and the purple curve despite the same martensite content. Figure 4.21(d) shows the contour plot of the order parameter φ_2 , which reveals that $\varphi_2 < 0$ in the area of the austenite at the horizontal boundaries next to the austenite-martensite-1 interface. Since the Landau polynomial of the separation potential in Eq. (4.43) is locally minimal for $\varphi_2 = 0$, f increases for $\varphi_2 < 0$. This increase causes the difference between the final value of the orange and the purple curve in Figure 4.20(b).

Concerning the microstructure in Figure 4.21(c) the curvature of the austenite-martensite-1 interface increases when it approaches the horizontal boundary. At the boundary it is parallel to the load direction. The indicated habit normal directions show that these are approximately met in some distance to the horizontal boundaries. With decreasing distance, the derivation increases until at the horizontal boundary the interface is oriented in vertical direction. This explains the negative order parameter in this region. The habit plane normal direction $n^{\Delta\epsilon*}$ of the austenite-martensite-1 interface, calculated according to Eq. (3.3) with

$\Delta\varepsilon^{0*} = \varepsilon_1^{0*} - \varepsilon^{0*}(\varphi_2 \rightarrow -1)$, approaches the horizontal direction. This is consistent with the vertically oriented interface. In Figure 4.21(d) the habit plane normal direction is exemplary indicated in orange for $\varphi_2 = -0.25$. Yet, a negative order parameter is energetically penalized by the separation potential. Additionally, $\varphi_2 < -\frac{\varepsilon_{12}^0 - \varepsilon_{\text{vol}}^0}{\varepsilon_{12}^0 + \varepsilon_{\text{vol}}^0}$ results in two positive eigenvalues of $\Delta\varepsilon^0 = \varepsilon_1^0 - \varepsilon^0(-\varphi_2)$ such that the invariant plane strain conditions in Eq. (3.2) would not be satisfied. Thus, a minimal value of $\varphi_2 \approx -0.25$ is obtained. By this way, the habit plane normal directions are met by the negative order parameter. In Section 5.2.3 it is shown, that this is also achieved less "artificially" by plastic deformations.

This mechanism applies analogously for the austenite-martensite-2 interfaces at the horizontal boundaries in Figure 4.21(c). For the other simulations of this section, where an external load is applied, the interfaces at the loaded boundaries are formed in the same way in load direction, (see e.g. the austenite-martensite-2 interface at the right-hand side of Figure 4.19(c)). However, in Figure 4.21(c) the influence of the negative order parameter is due to the two interfaces higher.

In summary, it is found that for considering the volumetric eigenstrain and more than a single martensite variant the model reflects the features of the martensitic transformation qualitatively. External loads influence the microstructure evolution depending on the eigenstrain. The martensite grows in a plate-like shape mostly in accordance with the calculated habit plane normal directions, which ensures, that the invariant plane strain condition is satisfied. The external load partially leads to deviant interface directions. This is compensated with negative order parameters by the elastic model. The related increase of the separation potential prevents the order parameters to leave the range. Thus, the model can be used to understand the interacting mechanisms on the microscale. In this context, also plastic strain induced martensite should be considered. Therefore, in the next chapter an enhanced phase field model is proposed.

4 An Elastic Phase Field Model for Martensitic Transformations

5 An Enhanced Phase Field Model for Martensitic Transformations

The microstructure of a component of austenitic steel, which is manufactured by cryogenic turning, is the result of various processes interacting on the microscale. In the following, the model introduced in Chapter 4, is enhanced to investigate the impact of plastic deformations and microcracks on the phase transformation. As this modification increases the numerical effort, in this context two variants are considered by an alternative approach in order to save computational power. However, this ansatz is also accompanied by some disadvantages. The details of this topic are discussed in Section 5.1. Building on this, a crystal plasticity scheme is included in Section 5.2, which allows accounting for the different crystal structures of the phases. Numerical simulations illustrate the importance of plastic deformations for the phase transition. Finally, in Section 5.3 the model is coupled to a phase field for fracture to study the relation between the martensitic transformations and cracks.

5.1 An Alternative Separation Potential

The findings in Section 4.3 show that two martensitic orientation variants have to be taken into account for modeling the martensitic transformation properly. So far for each variant an individual order parameter is used, leading to two additional nodal degrees of freedom for the FE-implementation, which enlarges the system of equations. For the two-dimensional case, two variants can be included numerically less costly by using the Landau polynomial proposed by Roumi [2010]

$$p(\varphi) = \frac{(3\Gamma^2 - 1 - 2\varphi^2)(1 - \varphi^2)^2}{3\Gamma^2 - 1}, \quad (5.1)$$

within the separation potential ψ^{sep} . Figure 5.1(a) shows the plot of $p(\varphi)$ with two global minima for $\varphi = \pm 1$, corresponding to two stable martensite variants. The local minimum at $\varphi = 0$ models the metastable phase austenite. Hence, with $p(\varphi)$ two variants are considered with a single order parameter $\varphi \in [-1, 1]$. The energy landscape is modified by the parameter Γ in Eq. (5.1). As the calibration constants depend on the Landau polynomial, these have to be redetermined according to Section 4.1.3 for considering $p(\varphi)$. Therefore, a standard equilibrium state of the phases $\Delta p(\varphi) = p(\varphi) - q(\varphi)$ with three equal minima is defined (see Figure 5.1(b)). The

5 An Enhanced Phase Field Model for Martensitic Transformations

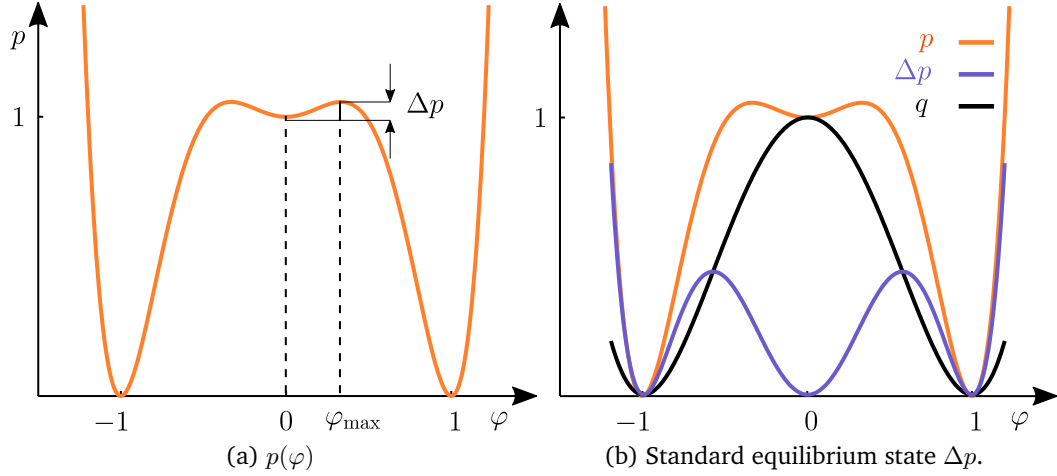


Figure 5.1: (a) Landau polynomial $p(\varphi)$. (b) For a uniquely defined Σ_{if} , a symmetric reference state Δp is necessary.

procedure following Eqs. (4.26)-(4.29) results in the calibration constants

$$\kappa_{\text{sep}} = \left(2\sqrt{\Delta p(\varphi(x_{if}))} \int_{-1}^1 \sqrt{\Delta p} \, d\varphi \right)^{-1}, \quad \kappa_{\text{grad}} = \frac{\sqrt{\Delta p(\varphi(x_{if}))}}{\int_{-1}^1 \sqrt{\Delta p} \, d\varphi}. \quad (5.2)$$

The parameter Γ of the Landau polynomial in Eq. (5.1) is set such that the energy barrier Δp coincides with the energy barrier of Section 4.3, where the material parameters of metastable austenites are assumed. This leads to $\Gamma = 0.35$ while the calibration constants result to be $\kappa_{\text{sep}} = 2.059$ and $\kappa_{\text{grad}} = 1.229$.

The change in sign of φ is exploited for describing the eigenstrain of the martensitic variants

$$\boldsymbol{\varepsilon}^0(\varphi) = \begin{bmatrix} \varphi^2 \varepsilon_{\text{vol}}^0 & \varphi \varepsilon_{12}^0 \\ \varphi \varepsilon_{12}^0 & \varphi^2 \varepsilon_{\text{vol}}^0 \end{bmatrix}. \quad (5.3)$$

The quadratic dependence on the order parameter φ results in a positive sign for the volumetric transformation strain $\varepsilon_{\text{vol}}^0$ for both orientation variants while the transformation shear part depends linearly on φ . Thus, ε_{12}^0 differs in sign for the different variants. For this definition of $\boldsymbol{\varepsilon}^0$ the coordinate system is considered in such a way that the diagonal entries of $\boldsymbol{\varepsilon}^0$ correspond to the volumetric part of the eigenstrain tensor $\boldsymbol{\varepsilon}_{\text{vol}}^0$ which is illustrated in Figure 5.2 by using Mohr's circle. For the numerical examples in Chapter 4 the principal coordinate system is used (orange line in Figure 5.2). To consider the dependence of the order parameter according to Eq. (5.3), a rotation of the coordinate system by 45° is required, which corresponds a rotation by 90° in Mohr's circle (purple line in Figure 5.2). This difference needs to be taken into account when setting up numerical simulations,

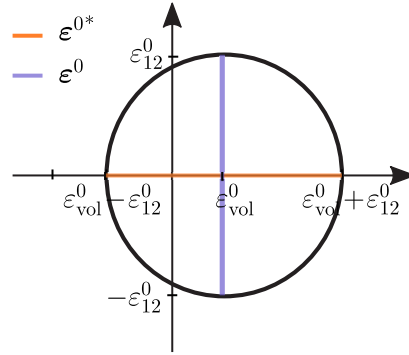


Figure 5.2: Mohr's circle for eigenstrain tensors according to Eq. (4.82) (orange) and Eq. (5.3) (purple).

that compare the two approaches.

Analogously, the elasticity tensor

$$\mathbf{C}(\varphi) = \mathbf{C}_A + \varphi^2 (\mathbf{C}_M - \mathbf{C}_A) \quad (5.4)$$

depends quadratically on the order parameter. This relation implicates the same stiffness \mathbf{C}_M for both variants. In the following, the elasticity tensors for the phases of Section 4.3 are applied. However, equivalently to the eigenstrain tensor in Eq. (5.3) the coordinate system is rotated by 45° , which yields

$$\mathbf{C}_A = \begin{bmatrix} 2.07 & 1.33 & 0 \\ 1.33 & 2.07 & 0 \\ 0 & 0 & 1.17 \end{bmatrix} 10^5 \text{ MPa}, \quad \mathbf{C}_M = 1.1 \mathbf{C}_A. \quad (5.5)$$

The further input parameters remain unchanged compared to Section 4.3 and the phase field potential reads

$$\psi = \frac{1}{2} (\boldsymbol{\varepsilon} - \boldsymbol{\varepsilon}^0) : \mathbf{C} (\boldsymbol{\varepsilon} - \boldsymbol{\varepsilon}^0) + \kappa_{\text{grad}} G L |\nabla \varphi|^2 + \kappa_{\text{sep}} \frac{G}{L} p. \quad (5.6)$$

To study the differences which arise due to applying $p(\varphi)$ according to Eq. (5.1) instead of $f(\varphi_1, \varphi_2)$ according to Eq. (4.43) some simulations are employed using both approaches. First, the two-phase beam, consisting of austenite and martensite, depicted in Figure 4.8(b), is applied. For these simulations the elastic energy density in the phase field potential is neglected to be able to analyse only the interface-related parts, the separation potential and the gradient term. In Figure 5.3(a) the evolution of $E^{\text{sep}} = \int_V \psi^{\text{sep}} dv$ and $E^{\text{grad}} = \int_V \psi^{\text{grad}} dv$ can be seen for the autocatalytic propagation of the austenite-martensite-interface (A-M-interface) where the orange curves correspond to using $p(\varphi)$ and the purple curves to using $f(\varphi_1, \varphi_2)$. All curves are referred to $E^{\text{grad}}(t = 0)$ or rather to $E^{\text{sep}}(t = 0)$ with $f(\varphi_1, \varphi_2)$ applied. Starting from the sharp interface in the initial configuration, the

5 An Enhanced Phase Field Model for Martensitic Transformations

transition zone is built, which decreases the gradient energy considerably. When the regularized interface propagates unchanged through the beam E^{grad} remains constant.

The moving interface increases the martensitic part of the beam. Since martensite corresponds to the global minimum of the Landau polynomial, E^{sep} decreases continuously. The purple E^{sep} -curve is steeper since the interface velocity $v_{\text{if}} = 1.49 \frac{\text{m}}{\text{s}}$ with using $f(\varphi_1, \varphi_2)$ is slightly above $v_{\text{if}} = 1.35 \frac{\text{m}}{\text{s}}$ of the present approach (using $p(\varphi)$). However, generally the curves of both simulations in Figure 5.3(a) fit quite well. On the other hand, Figure 5.3(b) shows the results for a

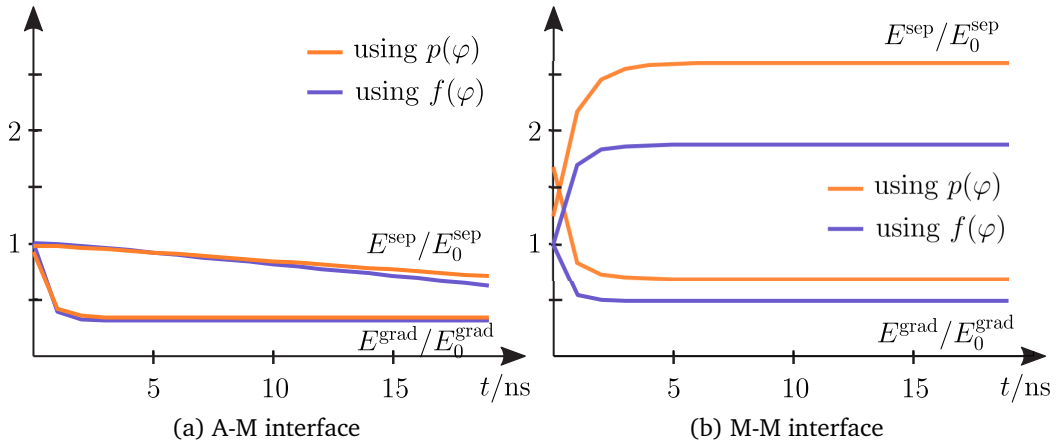


Figure 5.3: Evolution of E^{sep} and E^{grad} for a two-phase beam with (a) A-M-interface and (b) M-M-interface using $p(\varphi)$ (orange) and $f(\varphi_1, \varphi_2)$ (purple).

martensite-1-martensite-2-beam. As both phases are stable, the martensite-martensite-interface (M-M-interface) does not propagate through the beam, but the transition zone is built. Concerning the gradient energy E^{grad} the curves are qualitatively similar to those in Figure 5.3(a). Yet, the orange curve is noticeable higher than the purple curve, even though, for the purple curve the gradient parts of both order parameters have to be taken into account. This results from the range of the order parameter which is for the orange curve – using $p(\varphi)$ with $\varphi \in [-1, 1]$ – twice compared to the range of the approach applied in Section 4.3 (purple curve) with $\varphi_i \in [0, 1]$. Since the length of the transition zone, during which the order parameter changes, is the same for both simulations this leads to higher gradients for using $p(\varphi)$.

For the initial configuration – the two martensitic phases divided by a sharp interface – the Landau polynomial is minimal in all points. Thus, the formation of the transition zone increases E^{sep} , where the increase is greater for the orange curve using $p(\varphi)$. Figure 5.1(a) shows that for a M-M-transition zone the order parameter φ has to cross the local minimum at $\varphi = 0$. In contrast, the function $f(\varphi_1, \varphi_2)$ is not limited to two dimensions, thus, the system is able to choose the energetically most favorable path (cf. Figure 4.5). Since both variants are a stable state of the system the interface does not move. Therefore, the separation

5.1 An Alternative Separation Potential

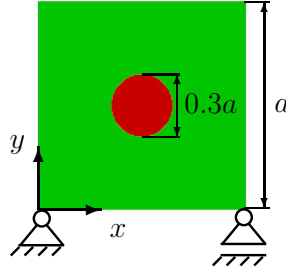


Figure 5.4: Initial configuration and boundary conditions.

energy E^{sep} remains constant after the transition zone has been built. To sum up, the two different approaches lead to similar results for A-M-interfaces. However, for the M-M-transition the Landau polynomial $p(\varphi)$ yields a higher interface energy.

In the next step the initial configuration depicted in Figure 5.4 is applied for both approaches: A quadratic austenitic specimen (edge length a) which contains a circular martensite 1 inclusion with a diameter of $0.3a$. Henceforth, the elastic energy is considered. For the single order parameter approach the coordinate system of the eigenstrain tensor and elasticity tensor are rotated by 45° compared to ε^{0*} and \mathbb{C}^* , which are used in Chapter 4. This changes the growing direction of the martensite. To ensure comparable conditions when the martensitic phase reaches the boundary of the computation domain, the matrix is rotated by 45° for the simulations where $p(\varphi)$ is used. Yet, the results in Figures 5.5 and 5.6 are shown in the same matrix orientation. Note in this regard the rotated coordinate system in Figure 5.6.

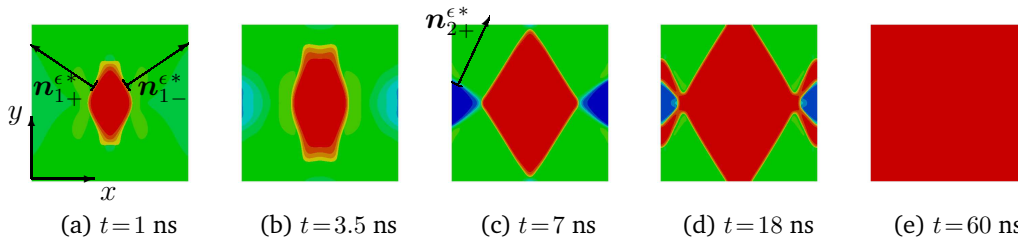


Figure 5.5: Austenitic (green) matrix with preexisting nucleus. Microstructure evolution for using $f(\varphi_1, \varphi_2)$ (martensite 1: red, martensite 2: blue).

Figure 5.5 shows the evolution of the martensitic phase for the approach proposed in Chapter 4 using $f(\varphi_1, \varphi_2)$. In Figure 4.14 the same initial configuration is applied for a smaller nucleus with a diameter of $0.2a$, which leads to a different formation of martensite. Therefore, the size of the initial nucleus influences the microstructure evolution.

In Figure 5.6 the simulation results for using the single order parameter approach with the Landau polynomial $p(\varphi)$ can be seen. The martensitic phases of

5 An Enhanced Phase Field Model for Martensitic Transformations

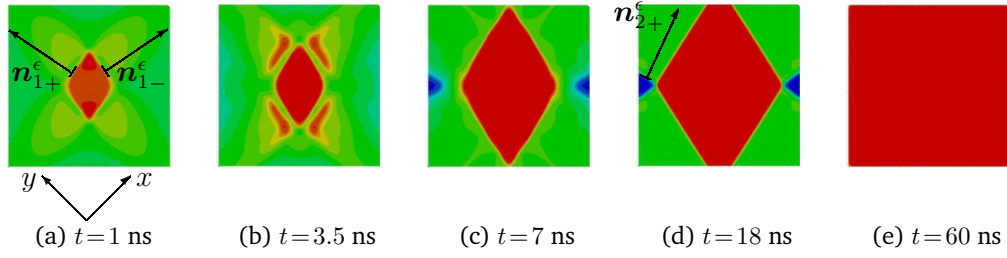


Figure 5.6: Austenitic (green) matrix with preexisting nucleus. Microstructure evolution for using $p(\varphi)$ (martensite 1: red, martensite 2: blue).

both variants form in accordance with the calculated habit plane normal directions \mathbf{n}_{1+}^ϵ , \mathbf{n}_{1-}^ϵ , \mathbf{n}_{2+}^ϵ , and \mathbf{n}_{2-}^ϵ . These are indicated in Figure 5.6 for the eigenstrain tensor in Eq. (5.3).

For both simulation results in Figure 5.5 and Figure 5.6, the circular nucleus turns initially into a plate-like shape. However, in the following, the martensite 1 plate in Figure 5.5(b) grows continuously while close-by the second variant is built. For using a single order parameter, at the same time step only martensite 1 is formed around the original plate (see Figure 5.6(b)). In Figure 5.6 the single order parameter restricts the possibilities to minimize the energy. For considering the two variants by two order parameters, each of them forms a transition zone. In each point, both order parameters can have a value between 0 and 1. By this way, the second variant is built around the growing variant 1 nucleus. On the other hand, for considering a single order parameter, the martensite 1 plate cannot evolve continuously when variant 2 is built around it. Thus, a discontinuous martensite 1 formation is observed in Figure 5.6(b). Since the growth of second variant in Figure 5.5(b) contributes to the minimization of the energy, this leads additionally to the fact, that for using the Landau polynomial $p(\varphi)$ a larger nucleus is necessary to trigger the evolution of the martensitic phase.

Some time steps later, the microstructures in Figure 5.5(c) and Figure 5.6(c) are similar. The martensite 1 plate has grown through the matrix while besides the second variant forms. However, in Figure 5.5(d), the first variant grows around the variant 2 martensite, which is not observed in Figure 5.6(d). In this context, the results in Figure 5.3(b) revealed that for using the Landau polynomial $p(\varphi)$ a M-M-interface is energetically more costly than for considering $f(\varphi_1, \varphi_2)$. Thus, the M-M-interface is not built in Figure 5.6(d). Finally, both approaches end up in a purely martensite 1 matrix.

In summary, the use of the Landau polynomial $p(\varphi)$ compared to the previous approach in Section 4 using $f(\varphi_1, \varphi_2)$ yields similar results for A-M-interfaces. However, the single order parameter restricts the possibilities of microstructure formation while the higher interface energy for the M-M-interface can lead to

different results. Additionally, the proposed ansatz entails limitations as for both martensite variants the same elasticity tensor has to be applied. Beyond that, the single order parameter approach cannot be extended to three dimensions.

On the other hand, using a single order parameter saves a lot of computational power compared to the previous approach. In this chapter the model is enhanced to consider the interactions of the phase transformation with crystal plasticity and damage, which already expands the numerical effort. Therefore, in a first step the Landau polynomial in Eq. (5.1) is used to improve the numerical efficiency. For future work, especially for an extension to three dimensions, the multiple order parameter approach should be employed. In this context the numerical performance can be improved e.g. by a GPU-accelerated implementation, which is proposed for a phase field model by Schlüter et al. [2014].

5.2 Crystal Plasticity

As discussed in Section 3.2 the martensitic transformation is accompanied by dislocation movement, which can be inherited by the martensitic phase, and thus influences the microstructure evolution. In this section dislocation movement is taken into account in the framework of crystal plasticity such that the different crystallographic structures of the phases can be included. Basic principles of crystal plasticity can be found e.g. in Schröder and Miehe [1997], Yalcinkaya [2011] while Lubliner [2008] and Simo and Hughes [1998] give a comprehensive overview concerning plasticity theory and its numerical implementation. In the context of phase field modeling of the martensitic transformation, crystal plastic deformations are taken into account e.g. by Yamanaka et al. [2009], Hildebrand and Miehe [2012], Richards et al. [2013], Schmitt et al. [2014a,c, 2015]. The numerical models allow a closer look on the relations between different phenomena interacting during the microstructure formation. For example Malik et al. [2013] use an elasto-plastic phase field model to study the effects of grain and twin boundaries on the martensitic transformation.

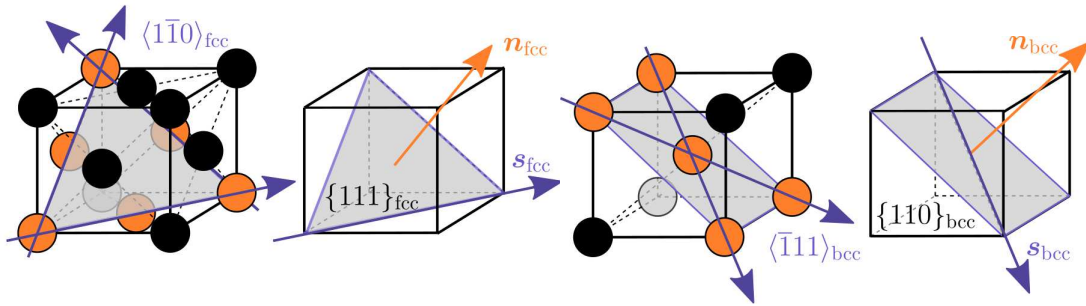
For this work a crystal plasticity setting with linear isotropic hardening is introduced which is discussed in detail in Schmitt et al. [2014a]. In this regard, Chapter 3 states that plasticity and phase transformation can interact in two ways – through kinetics and through the stresses. The former is well studied in the literature (e.g. Olson and Cohen [1972]). However, the latter is also important but often overlooked. Therefore, in the following, the first is explicitly turned off to isolate the interactions through the stresses.

With the aid of the extended model, first a basic example is considered to gain a better understanding for the correlations between the different processes on the microstructure. Subsequently, motivated by the process of cryogenic turning, the evolution of the phases is studied for a loaded surface. In this context, the impacts of the plastic deformations and the inheritance of plastic deformations between

austenite and martensite are focused. For this part the reader is referred to Schmitt et al. [2015].

5.2.1 Kinematics, Energetic Setting and Constitutive Laws

Experiments have shown that plastic deformations of metallic crystals result from a relative movement or *slip* of specific crystal planes caused by shear stress acting along the planes. These *slip planes* can be identified with those planes where the atoms are most closely packed. Analogously, the preferred *slip directions* are the directions of closest packing. A slip plane and slip direction form a *slip system*.



(a) Face centered cubic (fcc) lattice of austenite. (b) Body centered cubic (bcc) lattice of martensite.

Figure 5.7: Slip planes and slip directions of austenite (a) and martensite (b).

Using the *Miller indices*, where $\langle \dots \rangle$ denote crystallographically equivalent directions and $\{ \dots \}$ a class of equivalent planes, the planes of closest packing in the austenitic fcc lattice are the four octahedral $\{111\}$ -planes. Each has three slip directions; corresponding to the closest packed face $\langle 1\bar{1}0 \rangle$ -diagonals, see Figure 5.7(a). The six $\{110\}$ -planes are the slip planes of the bcc lattice, where each plane has two slip directions (the corresponding $\langle \bar{1}11 \rangle$ -directions). In Figure 5.7(b) one slip plane of bcc lattice is depicted exemplary. Hence, in total each of the phases has twelve primary slip systems. Regarding the notation in this work, γ_k is the plastic slip while s_k designates the slip direction and n_k the normal direction of the slip plane in the k^{th} slip system. Using these quantities, the *global plastic strain* ϵ^p is calculated by summing up over the total number of slip systems N_k

$$\epsilon^p = \sum_{k=1}^{N_k} \gamma_k \mathbf{P}_k, \quad (5.7)$$

$$\text{with } \mathbf{P}_k = \frac{1}{2} [\mathbf{s}_k \otimes \mathbf{n}_k + \mathbf{n}_k \otimes \mathbf{s}_k]. \quad (5.8)$$

In Eq. (5.7), the *projector* \mathbf{P}_k is the strain (direction) associated with the k^{th} slip system, see for example Richards et al. [2013]. Despite austenite and martensite

have different slip systems which differ in \mathbf{s}_k and \mathbf{n}_k , the evaluation of Eq. (5.8) results in identical \mathbf{P}_k for both phases. Consequently, this setting considers identical slip systems for austenite ($k = 1, 2$) and martensite ($k = 3, 4$), where slip system $k=1$ corresponds to $k=3$ and $k=2$ corresponds to $k=4$. Due to the limitation to two dimensions, the number of slip systems per phase is reduced to two. The plastic strain $\boldsymbol{\varepsilon}^p$ in Eq. (5.7) is part of the linearized total strain tensor, which is the sum of the elastic strain $\boldsymbol{\varepsilon}^e$, the transformation-induced eigenstrain $\boldsymbol{\varepsilon}^0$ and the plastic strain $\boldsymbol{\varepsilon}^p$

$$\boldsymbol{\varepsilon} = \boldsymbol{\varepsilon}^e + \boldsymbol{\varepsilon}^0 + \boldsymbol{\varepsilon}^p. \quad (5.9)$$

With the plastic deformation of the material the stress increases which is called *strain hardening* or *work hardening*. For the idealized setting in this work linear isotropic self-hardening is considered, described for each slip system k by a *hardening variable* α_k . The hardening of the material involves a plastic contribution to the total energy, the *work hardening potential*

$$W^h(\alpha_k) = \frac{1}{2} \sum_{k=1}^{N_k} H_k \alpha_k^2, \quad (5.10)$$

with the *hardening moduli* H_k . Hence, the phase field potential reads

$$\begin{aligned} \psi(\boldsymbol{\varepsilon}, \varphi, \boldsymbol{\nabla}\varphi, \gamma_k, \alpha_k) &= W(\boldsymbol{\varepsilon}^e, \varphi) + \psi^{\text{grad}}(\boldsymbol{\nabla}\varphi) + \psi^{\text{sep}}(\varphi) + W^h(\alpha_k) \\ &= \frac{1}{2} (\boldsymbol{\varepsilon} - \boldsymbol{\varepsilon}^0(\varphi) - \boldsymbol{\varepsilon}^p) : [\mathbf{C}(\varphi) (\boldsymbol{\varepsilon} - \boldsymbol{\varepsilon}^0(\varphi) - \boldsymbol{\varepsilon}^p)] \\ &\quad + \frac{1}{2} \kappa_g G L \|\boldsymbol{\nabla}\varphi\|^2 + \kappa_s \frac{G}{L} f(\varphi) + \frac{1}{2} \sum_{k=1}^{N_k} H_k \alpha_k^2. \end{aligned} \quad (5.11)$$

With the phase field potential in Eq. (5.11), the constitutive relation for the stresses results in

$$\boldsymbol{\sigma} = \frac{\partial \psi}{\partial \boldsymbol{\varepsilon}} = \mathbf{C}(\varphi) (\boldsymbol{\varepsilon} - \boldsymbol{\varepsilon}^0(\varphi) - \boldsymbol{\varepsilon}^p) \quad (5.12)$$

while analogously q_k defines the work conjugate to the hardening variable α_k

$$q_k = -\frac{\partial \psi}{\partial \alpha_k} = -\frac{\partial W^h}{\partial \alpha_k} = -H_k \alpha_k. \quad (5.13)$$

The *resolved shear stress* on a slip system, which is also called *Schmid stress*, is computed with the projector \mathbf{P}_k

$$\tau_k = \mathbf{P}_k : \boldsymbol{\sigma} = \boldsymbol{\sigma} : \mathbf{P}_k. \quad (5.14)$$

The constituted material behavior is motivated by the rheological model in Figure 5.8, consisting of an elastic crystal lattice, connected to a dashpot with the viscosity η in parallel with two slip planes of the k^{th} slip system, where slip γ_k occurs for $\tau_k > \tau_k^{\text{cr}}$. Thus, if the Schmid stress is sufficiently small, the crystal lattice is

5 An Enhanced Phase Field Model for Martensitic Transformations

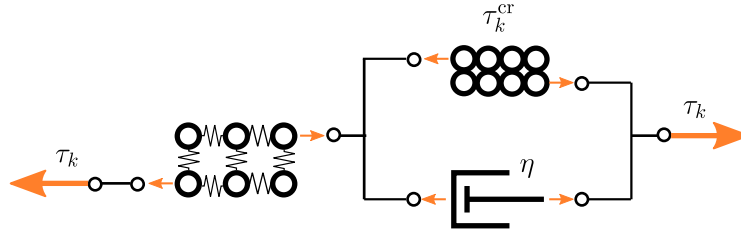


Figure 5.8: Rheological model.

deformed elastically. If the Schmid stress τ_k exceeds the critical value τ_k^{cr} , there is a relative movement of the slip planes leading to the stress $\eta \dot{\gamma}_k$ in the dashpot such that

$$\tau_k = \tau_k^{cr} + \eta \dot{\gamma}_k, \quad \text{if } \tau_k > \tau_k^{cr}. \quad (5.15)$$

From the requirement in Eq. (5.15), the yield criterion is deduced,

$$\phi_k = |\tau_k| - \tau_k^{cr} > 0. \quad (5.16)$$

If the yield criterion ϕ_k is satisfied by the Schmid stress τ_k , the k^{th} slip system is activated. Equation (5.16) considers the absolute value of τ_k since a slip system can be activated by both positive and negative τ_k . The evolution law of the slip $\dot{\gamma}_k$ in an active slip system is derived from Eq. (5.15). With introducing the *Macaulay brackets*

$$\langle x \rangle = \begin{cases} 0 & x \leq 0 \\ x & x > 0 \end{cases}, \quad (5.17)$$

it may be written compactly

$$\dot{\gamma}_k = \frac{1}{\eta} \langle |\tau_k| - \tau_k^{cr}(\varphi, q_k) \rangle \text{sgn}(\tau_k), \quad (5.18)$$

where

$$\text{sgn}(\tau_k) = \begin{cases} +1 & \text{if } \tau_k > 0 \\ -1 & \text{if } \tau_k < 0 \end{cases}. \quad (5.19)$$

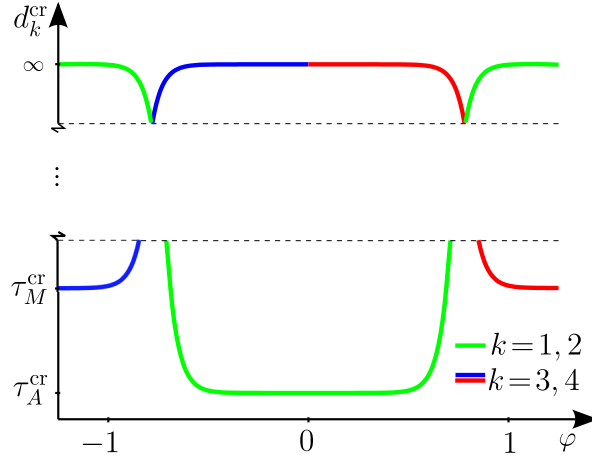
The hardening variable α_k is assumed to evolve in the same manner

$$\dot{\alpha}_k = |\dot{\gamma}_k|. \quad (5.20)$$

In Eq. (5.18), τ_k^{cr} depends on q_k and the order parameter φ . Concerning q_k , for this work a linear dependence is considered

$$\tau_k^{cr}(\varphi, q_k) = d_k^{cr}(\varphi) - q_k = d_k^{cr}(\varphi) + H_k \alpha_k. \quad (5.21)$$

The dependence of τ_k^{cr} on the order parameter φ is necessary since only the slip systems of the present phase can be activated. This is ensured by the *critical driving*

Figure 5.9: Critical driving force for plasticity $d_k^{\text{cr}}(\varphi)$.

force for plasticity $d_k^{\text{cr}}(\varphi)$. For austenitic material ($\varphi = 0$), the critical shear stress of the austenitic phase τ_A^{cr} is taken into account for the austenitic slip systems ($k = 1, 2$). The critical shear stress of the martensitic phase τ_M^{cr} is set to a sufficiently high value for the martensitic slip systems ($k = 3, 4$), so that these remain inactive. In the same manner, for $\varphi = \pm 1$, the martensitic yield strength τ_M^{cr} is taken into account for $k = 3, 4$ and τ_A^{cr} is set to a high value for $k = 1, 2$ by the following relation

$$d_k^{\text{cr}}(\varphi) = \begin{cases} a^\infty \left[\frac{\tau_A^{\text{cr}}}{a^\infty} + 1 + \tanh(a_1 \varphi - a_2) + 1 - \tanh(a_1 \varphi + a_2) \right] & k = 1, 2 \\ & (\varphi = 0) \\ a^\infty \left[\frac{\tau_M^{\text{cr}}}{a^\infty} + \tanh(a_1 \varphi + a_2) - \tanh(a_1 \varphi - a_2) \right] & k = 3, 4 \\ & (\varphi = \pm 1) \end{cases} \quad (5.22)$$

In Eq. (5.22) the coefficients a_1 and a_2 determine the shape of d_k^{cr} while a^∞ is set to a high value compared to the critical shear stresses. For this investigation the values $a_1 = 25$, $a_2 = 15$ and $a^\infty = 50000$ MPa are used.

5.2.2 Local Time Integration Scheme

In order to evaluate the evolution equations (5.18) and (5.20) of the slip and the hardening, γ_k and α_k are considered as internal history variables while a time integration scheme is applied on the element level. The algorithm for the time integration is based on an implicit Euler backward scheme, in form of a *predictor corrector method*. The time interval $[t_n, t_{n+1}]$ is considered while the variables at $t = t_n$ are known. In the first predictor step, an *elastic trial value* for the strains is given with

5 An Enhanced Phase Field Model for Martensitic Transformations

with $\underline{\varepsilon}^{\text{p, tr}} = \underline{\varepsilon}_n^{\text{p}} = \sum_{k=1}^{N_k} \gamma_{n,k} \mathbf{P}_k$, so the resolved shear stress on all slip systems k can be calculated for the trial state

$$\underline{\sigma}^{\text{tr}} = \underline{\mathbb{C}}(\varphi) \left(\underbrace{\underline{\varepsilon}_{n+1} - \underline{\varepsilon}_{n+1}^0(\varphi) - \underline{\varepsilon}_n^{\text{p}}}_{\underline{\varepsilon}^{\text{tr}}} \right), \quad (5.23)$$

$$\tau_k^{\text{tr}} = \underline{\sigma}^{\text{tr}} \cdot \underline{\mathbf{P}}_k. \quad (5.24)$$

To keep the equations simple, the time step index $n+1$ is suppressed for the trial state quantities. Furthermore, for the following relations $\text{sgn}(\tau_{k,n+1}) = \text{sgn}(\tau_k^{\text{tr}})$ is assumed, which can be shown for a single slip system. A generalization for multiple slip systems seems reasonable. With the trial state quantities, for each slip system the yield criterion is checked

$$\phi_{k,n+1}^{\text{tr}} = |\tau_k^{\text{tr}}| - \tau_k^{\text{cr, tr}}(\varphi) = |\tau_k^{\text{tr}}| - \tau_{k,n}^{\text{cr}}(\varphi), \quad (5.25)$$

where $\alpha_k^{\text{tr}} = \alpha_{k,n}$. If $\phi_k^{\text{tr}} > 0$, k is an active slip system. Applying the update formula according to the backward Euler method (cf. Eq. (4.66)) on the evolution law in Eq. (5.18) for γ_k yields the update formula for active slip systems

$$\gamma_{k,n+1} = \gamma_{k,n} + \frac{\Delta t}{\eta} \underbrace{\langle |\tau_{k,n+1}| - \tau_{k,n+1}^{\text{cr}} \rangle}_{\langle \phi_{k,n+1} \rangle} \text{sgn}(\tau_{k,n+1}) = \gamma_{k,n} + \Delta \gamma_{k,n+1} \text{sgn}(\tau_k^{\text{tr}}), \quad (5.26)$$

with

$$\Delta \gamma_{k,n+1} = \frac{\Delta t}{\eta} \langle \phi_{k,n+1} \rangle. \quad (5.27)$$

Thus, the time-discrete version of the evolution equation of the hardening variable α_k reads

$$\alpha_{k,n+1} = \alpha_{k,n} + \Delta t \dot{\alpha}_{k,n+1} = \alpha_{k,n} + \Delta t |\dot{\gamma}_{k,n+1}| = \alpha_{k,n} + \frac{\Delta t}{\eta} \Delta \gamma_{k,n+1}. \quad (5.28)$$

The unknown $\Delta \gamma_{k,n+1}$ is obtained by a set of linear equations. Therefore, the time discrete version of Eq. (5.14) is multiplied with $\text{sgn}(\tau_{k,n+1}) = \text{sgn}(\tau_k^{\text{tr}})$, which yields with using Eq. (5.23) and Eq. (5.26)

$$|\tau_{k,n+1}| = |\tau_k^{\text{tr}}| - \sum_{l=1}^{N_{\text{act}}} \left[\underbrace{\underline{\mathbf{P}}_k^T \underline{\mathbb{C}}(\varphi) \underline{\mathbf{P}}_l \text{sgn}(\tau_k^{\text{tr}}) \text{sgn}(\tau_l^{\text{tr}})}_{R_{kl}} \Delta \gamma_{l,n+1} \right], \quad (5.29)$$

where $l \in \{1, \dots, N^{\text{act}}\}$ denotes the l^{th} of N^{act} active slip systems. This is used for recasting the update formula of the yield function

$$\begin{aligned} \phi_{k,n+1} &= \underbrace{|\tau_{k,n+1}|}_{\text{with Eq. (5.29)}} - \tau_{k,n+1}^{\text{cr}} \\ &= |\tau_k^{\text{tr}}| - \sum_{l=1}^{N^{\text{act}}} R_{kl} \Delta\gamma_{l,n+1} - \left(\tau_{k,n}^{\text{cr}} + \sum_{l=1}^{N^{\text{act}}} H_{kl} \Delta\gamma_{l,n+1} \right) \\ \phi_{k,n+1} &= \phi_k^{\text{tr}} - \sum_{l=1}^{N^{\text{act}}} (R_{kl} + H_{kl}) \Delta\gamma_{l,n+1}, \end{aligned} \quad (5.30)$$

with the diagonal matrix

$$H_{kl} = \begin{bmatrix} H_1 & 0 & \dots & 0 \\ 0 & \ddots & 0 & \vdots \\ \vdots & 0 & \ddots & 0 \\ 0 & \dots & 0 & H_{N_k} \end{bmatrix} \quad (5.31)$$

Finally, Eq. (5.30) is inserted into the definition of $\Delta\gamma_k$ in Eq. (5.27). Since only active slip systems are taken into account, the Macaulay brackets in Eq. (5.27) are omitted. This results in a set of linear equations for the $\Delta\gamma_l$

$$\sum_{l=1}^{N^{\text{act}}} \underbrace{\left[\delta_{kl} + \frac{\Delta t}{\eta} (R_{kl} + H_{kl}) \right]}_{A_{kl}} \Delta\gamma_{l,n+1} = \underbrace{\frac{\Delta t}{\eta} \phi_k^{\text{tr}}}_{b_k}, \quad (5.32)$$

where δ_{kl} denotes the identity tensor. With $\Delta\gamma_k$ known, the evaluation of Eq. (5.26) yields the updated $\gamma_{k,n+1}$, which are subsequently used to compute the values for the stresses $\boldsymbol{\sigma}$ and the tangent moduli $\mathbf{C}(\varphi)$ for the time step $t = t_{n+1}$

$$\boldsymbol{\sigma}_{n+1} = \mathbf{C}(\varphi) \left[\boldsymbol{\varepsilon}_{n+1} - \sum_{k=1}^N \gamma_{k,n+1} \mathbf{P}_k \right], \quad (5.33)$$

$$\mathbf{C}_{n+1}^{\text{tan}}(\varphi) = \mathbf{C}(\varphi) - \sum_{k=1}^{N^{\text{act}}} \sum_{l=1}^{N^{\text{act}}} \left[\mathbf{C}(\varphi) \mathbf{P}_k \text{sgn}(\tau_k^{\text{tr}}) \frac{\Delta t}{\eta} (A_{kl})^{-1} \mathbf{P}_l^T \mathbf{C}(\varphi) \text{sgn}(\tau_l^{\text{tr}}) \right], \quad (5.34)$$

where the tangential stiffness $\mathbf{C}^{\text{tan}}(\varphi)$ is given by the derivative $\frac{\partial \boldsymbol{\sigma}_{n+1}}{\partial \boldsymbol{\varepsilon}_{n+1}}$. For a plastic update it is considered instead of the elasticity tensor in the element stiffness matrix $\mathbf{K}_{I,J,e}$ in Eq. (4.72). While maintaining the convergence of the FE-problem, the derivative $\frac{\partial \Delta\gamma_{k,n+1}}{\partial \varphi_{n+1}}$ could be neglected which avoids elongated terms in the stiffness matrix. The flowchart in Figure 5.10 visualizes the integration of the crystal

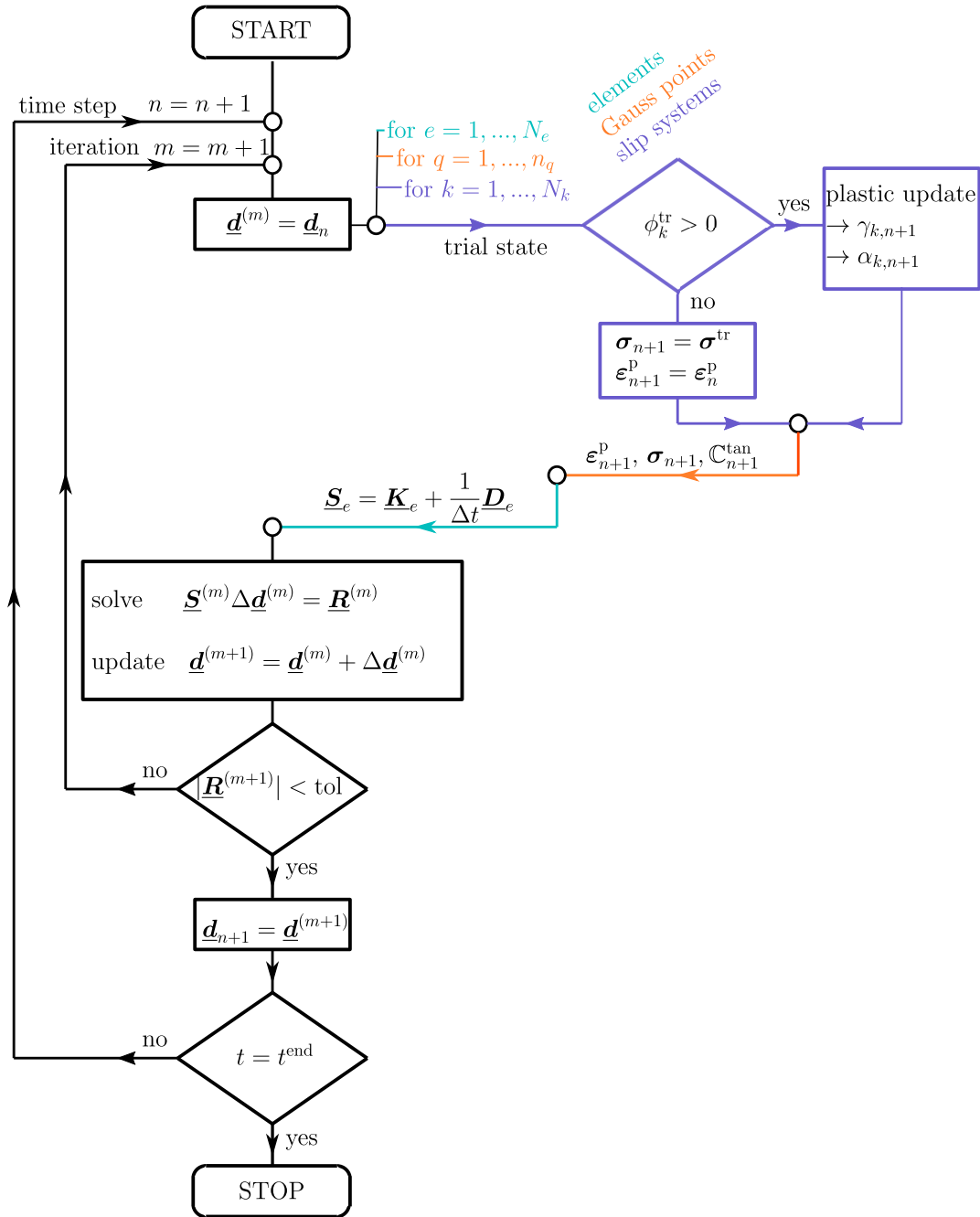


Figure 5.10: Flowchart of the FE program.

plastic material law into the overall finite element program. The history variables γ_k and α_k evolve on the element level while for the evolution of the order parameter φ the global time integration scheme is applied, which is discussed in Section 4.2.2.

5.2.3 Numerical Examples

For the numerical implementation the following slip systems are taken into account,

$$\begin{aligned} \mathbf{s}_1 = \mathbf{s}_3 &= \begin{bmatrix} 1 \\ 0 \end{bmatrix}, & \mathbf{n}_1 = \mathbf{n}_3 &= \begin{bmatrix} 0 \\ 1 \end{bmatrix}, & \Rightarrow \mathbf{P}_1 = \mathbf{P}_3 &= \frac{1}{2} \begin{bmatrix} 0 & 1 \\ 1 & 0 \end{bmatrix}, \\ \mathbf{s}_2 = \mathbf{s}_4 &= \frac{1}{\sqrt{2}} \begin{bmatrix} 1 \\ 1 \end{bmatrix}, & \mathbf{n}_2 = \mathbf{n}_4 &= \frac{1}{\sqrt{2}} \begin{bmatrix} -1 \\ 1 \end{bmatrix}, & \Rightarrow \mathbf{P}_2 = \mathbf{P}_4 &= \frac{1}{2} \begin{bmatrix} -1 & 0 \\ 0 & 1 \end{bmatrix}, \end{aligned}$$

where the corresponding slip directions and slip normals are depicted schematically in Figure 5.11. The slip systems $k = 1$ and $k = 3$ correspond to pure shear, i.e. compression and tension parallel to the diagonals of the coordinate system in Figure 5.11. The slip systems $k = 2$ and $k = 4$ are associated with simple shear, i.e. compression parallel to the x -axis and tension parallel to the y -axis of the coordinate system in Figure 5.11. Furthermore, a yield strength of $\tau_{\text{fcc}}^{\text{cr}} = 100$ MPa is considered

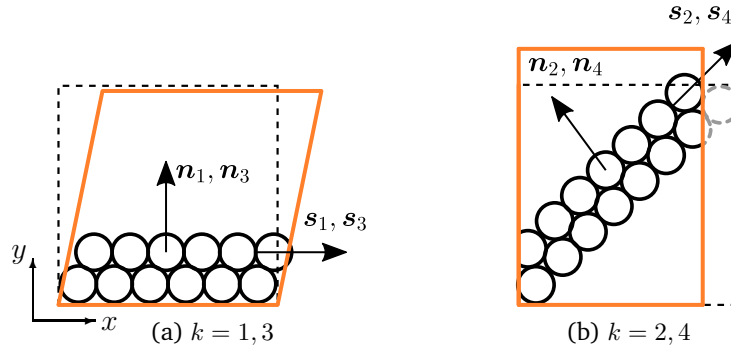


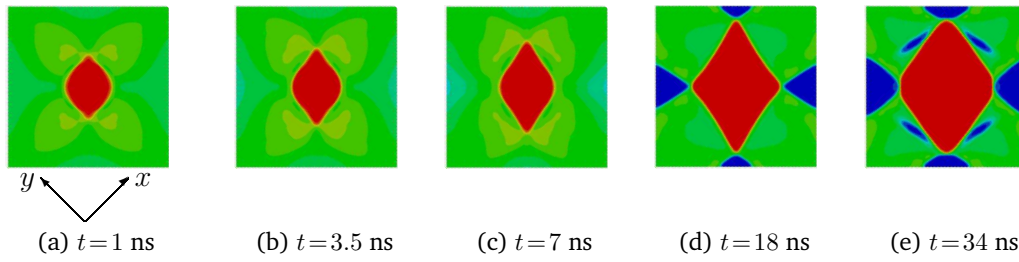
Figure 5.11: Slip normals and slip directions of the considered slip systems.

for the austenitic phase. Since the martensitic yield strength $\tau_{\text{bcc}}^{\text{cr}}$ is much higher than the austenitic one, $\tau_{\text{bcc}}^{\text{cr}}$ is set to a very high value which is not reached in the numerical simulations. In that way plastic deformations in martensite can only be caused by inheritance. The viscosity constant $\eta = 10 \frac{\text{Ns}}{\text{m}^2}$ is used.

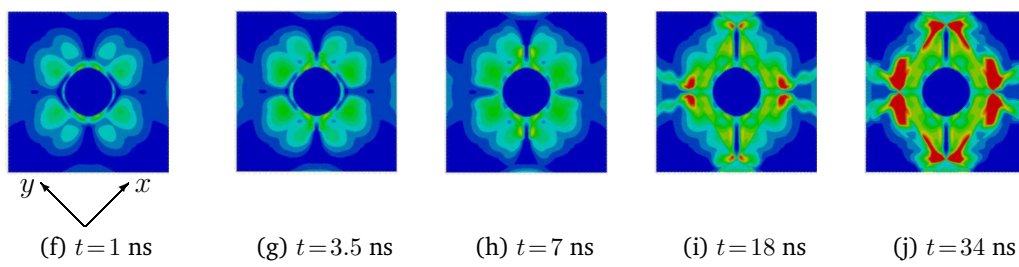
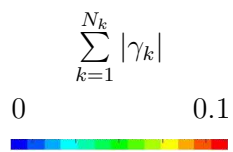
Circular Nucleus

In order to get a general idea of the impact of the plastic deformations on the phase transformation, the initial configuration in Figure 5.4 is used for a crystal plastic simulation. In Figures 5.12(a)-(e) the resulting microstructure can be seen while Figures 5.12(f)-(j) depict the accumulated slip $\sum_{k=1}^{N_k} |\gamma_k|$, which is a measure for the

5 An Enhanced Phase Field Model for Martensitic Transformations

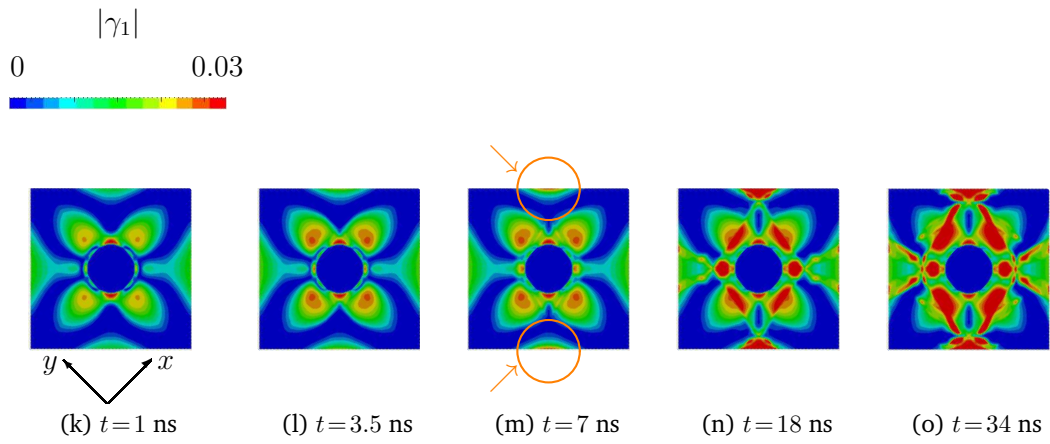


Microstructure evolution, austenite: green, martensite 1: red, martensite 2: blue.

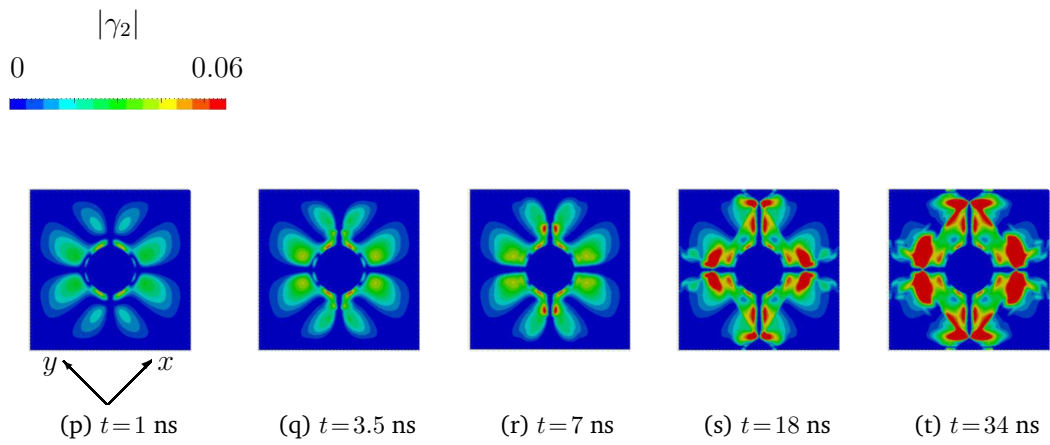


Accumulated slip $\sum_{k=1}^{N_k} |\gamma_k|$.

Figure 5.12



Absolute value of the slip of the first slip system γ_1 .



Absolute value of the slip of the second slip system γ_2 .

Figure 5.12: Simulation results for considering crystal plasticity.

plastic deformation. The comparison of the microstructures in Figures 5.12(a)-(e) with the results in Figures 5.6, where an elastic material law is applied, shows that crystal plastic deformations influence the phase transformation. Particularly the initial evolution in Figures 5.12(b)-(c) illustrates a slower growth of the martensitic phase. Figure 5.12(f) reveals a plastic zone, which has been formed around the nucleus due to the eigenstrain within the martensite. The plastic deformation seems to constrain the phase transformation. In this context, the plot of the elastic energy E^{el} as a function of simulation time in Figure 5.13 is considered. The elastic simulation corresponds to the orange curve and the crystal plastic simulation to the purple one. The plastic zone, which is built around the nucleus, dissipates energy such that the purple curve is initially clearly below the orange curve. The dissipated energy is not available for the phase transformation, which is consequently delayed. Hence, when the martensitic plate starts to evolve, the purple curve of the crystal plastic simulation increases less than the orange curve. Furthermore, the orange

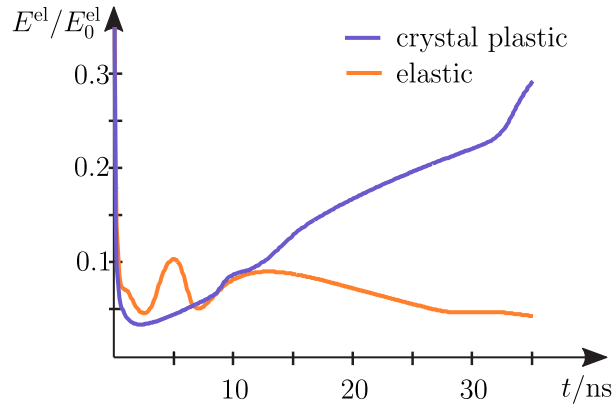


Figure 5.13: Evolution of the elastic energy for the elastic simulation in Figure 5.6 (orange curve) and the crystal plastic simulation in Figure 5.12 (purple curve).

curve of the elastic simulation has a peak when the martensite 1 plate has grown through the matrix. Subsequently, it increases again when the second variant forms (see Figure 5.6(c)). Finally, the orange curve decreases when the variant 1 plate broadens, eliminating the martensite 2 formations, until a purely martensite 1 matrix remains.

For the crystal plastic simulation the variant 1 plate does not grow through the matrix. Instead, variant 2 martensite is built around the martensite 1 plate, which leads, due to the eigenstrain, to a continuously increasing purple curve. Eventually, the variant 1 plate is framed by martensite 2.

In order to understand the mechanisms leading to the differences of the crystal plastic simulation compared to the elastic simulation in Figure 5.6, the individual slip systems are considered in Figure 5.12. In Figures 5.12(k)-(o) the absolute value of the slip of the first slip system $k=1$ is depicted which corresponds to pure shear, i.e. tension and compression parallel to the horizontal and vertical

directions, respectively. In the same way the shear part of the eigenstrain in Eq. (5.3) corresponds to a pure shear loading. Thus, Figure 5.12(k) shows that initially the highest slip arises at the tips of the martensitic plate. In the following time steps the plate evolves in vertical direction. As a result the eigenstrain within the plate activates the slip system $k = 1$ at the boundary of the matrix opposed to the plate tips. This small strip of high plastic deformation, which can be seen in Figures 5.12(m) (marked by arrows), leads to a strain-induced nucleation of variant 2 martensite, cf. Figure 5.12(d). Since the eigenstrain direction and the plastic strain direction of the slip system coincide, the growing martensite activates the slip system $k = 1$ in its surroundings. This results in a further nucleation of variant 2 martensite next to the martensite 1 plate.

The evolution of the norm of slip of the second slip system $k = 2$ can be seen in Figures 5.12(p)- (t). The slip is higher than for slip system $k = 1$. Figure 5.12(p) shows the slip system $k = 2$ activated around the martensitic nucleus. The shear part of the eigenstrain in the martensite 1 plate in Figure 5.12 corresponds to compression in the plate direction and tension perpendicular to the plate direction. The plots show the norm of the slip, thus, there is no distinction between expansion and compression visible, which explains the radial activation of slip system $k = 2$. Yet, there is less slip in plate direction. The volumetric part of the eigenstrain $\varepsilon_{\text{vol}}^0$ reduces the compression in plate direction, which results from the shear part ε_{12}^0 and analogously increases the tension perpendicular to the plate direction. Therefore, the activation of the slip system $k = 2$ in Figure 5.12(p) is not rotationally symmetric about the nucleus.

When the martensite plate starts to grow through the ring-shaped slip of system $k = 2$, the slip system is activated at the sides of the plate tip. This leads to the two lines of plasticity in direction of the growing plate which can be seen in Figures 5.12(r)-(t). The slip activated by the martensitic plate demonstrates the correlations between plasticity and the phase transformation. Additional numerical examples, e.g. the microstructure evolution for two nuclei of different martensitic variants, can be found in Schmitt et al. [2014a].

Thus, strong interactions between the martensitic transformation and crystal plasticity are observed since the phase transformation leads to slip while on the other hand martensite is triggered by plastic deformations. Furthermore, the plastic deformations influence the formation of the martensitic phase since additional energy is dissipated. In a next step the phase transformation in a crystal plastic material is studied at a loaded surface, which is motivated by the turning process.

A Loaded Surface

In Aurich et al. [2014], the surface hardening during cryogenic turning of metastable austenitic steel is investigated. Concerning the load, which is induced by the turning tool, the authors find mainly the component perpendicular to the

5 An Enhanced Phase Field Model for Martensitic Transformations

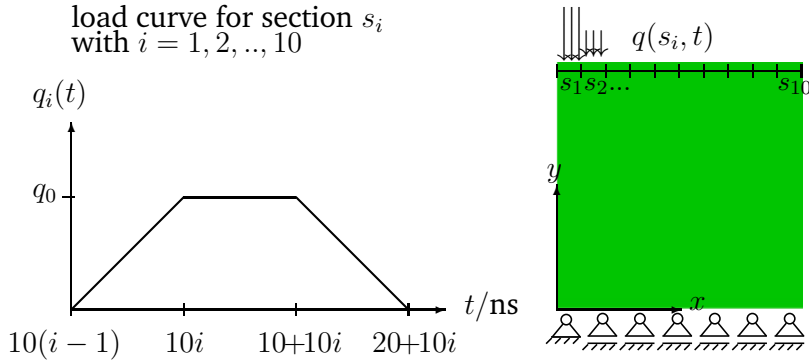


Figure 5.14: Left: Load curve of the i^{th} surface section. Right: Boundary conditions for the initially austenitic (green) workpiece.

surface to be crucial for the martensitic transformation. This motivates the numerical setup of the following examples, proposed in Schmitt et al. [2015]: On an initially purely austenitic workpiece, which is fixed at the lower boundary in vertical direction, a compressive moving surface load $q_i(t)$ is applied for $t \in [0, 120]$ ns, see Figure 5.14. Therefore, the surface is divided into ten sections s_i . The load $q_i(t)$ on the i^{th} section is plotted as a function of time in Figure 5.14 on the left-hand side. The left- and right-hand boundaries of the computation domain are stress free. For the simulations in this section, the computation domain is discretized by 300×300 uniform elements. This finer discretization is chosen to properly resolve the complex resulting microstructures.

First, for both phases elastic material behavior is assumed, without accounting for plastic deformations. The resulting evolution of the phases can be seen in Figures 5.15(a)-(e). The applied load leads to stress-assisted nucleation of martensite (since no plastic deformations are considered). The loaded part of the surface is compressed in vertical direction inducing tensile stresses in the free part of the surface. Between the compressed and the stretched part of the surface high positive shear stress arises, corresponding to the eigenshear in the first martensite variant, which is consequently built, see Figure 5.15(a). In the following, it can be observed that the formation of the first variant follows the loading. With locally decreasing compressive stress, the first variant degenerates, too. The total deformation of the specimen can be reduced by the formation of the second martensitic variant, as the eigenshear is considered with negative sign in Eq. (5.3). After the load has traveled across the entire surface at $t = 120$ ns, the workpiece is purely martensitic, where vertical plates of both variants have formed (see Figure 5.15(d)). Yet, these plates vanish subsequently and two continuous martensitic phases remain (see Figure 5.15(e)). This state is energetically favorable for the system. As there is only a single interface, the contribution of the gradient term ψ^{grad} is low and the absence of austenite yields $\psi^{\text{sep}} = 0$ for all points of the system. However, compared to the

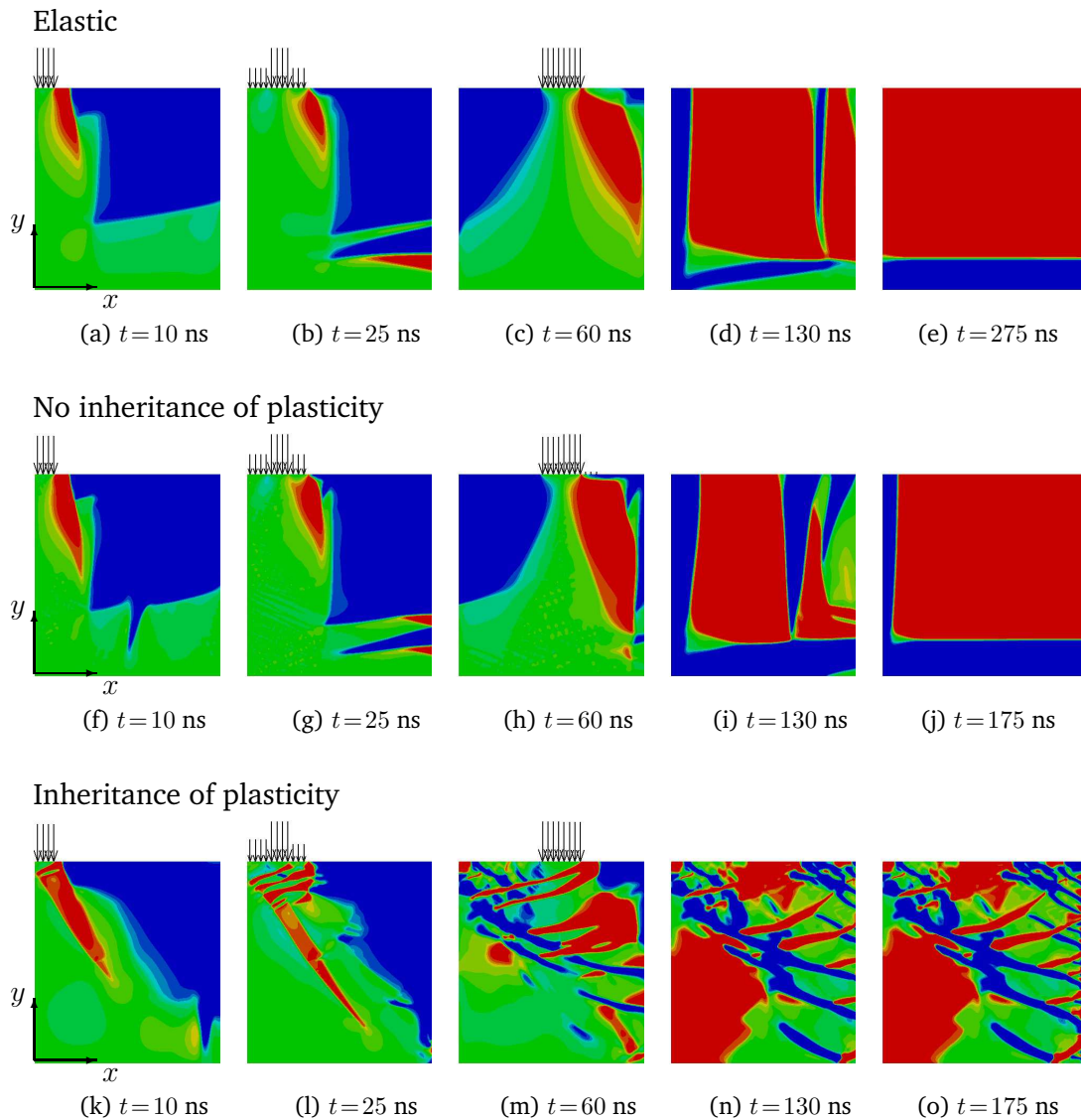


Figure 5.15: Evolution of a microstructure for a loaded surface (green: austenite, red: martensite 1, blue: martensite 2); magnitude and position of the traveling load indicated by arrows. (a)- (e): Austenite: elastic, martensite: elastic. (f)- (j): Austenite: crystal plastic, martensite: elastic. (k)- (o): Austenite: crystal plastic, martensite: elastic.

microstructures that are observed in austenitic steels, the result is far from reality.

Since the martensitic yield strength is much higher than the austenitic one, in Schmitt et al. [2013b] the authors consider plastic deformations only for austenite, while martensite is modeled as an elastic material. Here, this material behavior results in the evolution of microstructure depicted in Figures 5.15(f)- (j). The comparison with the purely elastic simulation above reveals the formation of some

5 An Enhanced Phase Field Model for Martensitic Transformations

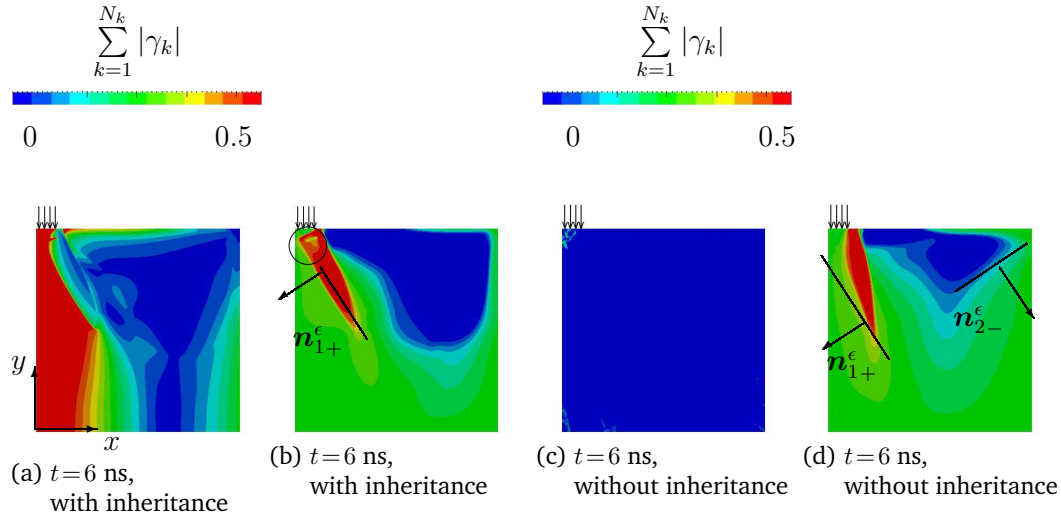


Figure 5.16: (a), (c), Accumulated slip $\sum_{k=1}^{N_k} |\gamma_k|$. (b), (d), Evolution of microstructure (green: austenite, red: martensite 1, blue: martensite 2).

additional deformation induced martensitic plates. Furthermore, on the left-hand side of the final microstructure in Figure 5.15(j), a small stripe of the second variant remains which is stabilized by the plastic deformations in the transition zone between the phases. But generally there is little difference to the purely elastic simulation. Though, plasticity is only considered for the austenitic phase, such that plastic deformations cannot be inherited to martensite. Due to the phase transition, dislocations in the austenitic phase are wiped out by this kind of material behavior.

Hence, in a next step, the inheritance of plastic deformations between austenite and martensite is taken into account. For both phases crystal plastic material behavior is considered while the martensitic yield limit is set to a very high value and the martensitic slip systems are not activated. Yet, the plastic deformations can be inherited from austenite to martensite. The approach is motivated by considering a dislocation in the austenitic phase, which is supposed to not vanish due to the transformation to martensite. This leads to a dislocation in the martensitic phase, which is inherited from the austenite. The microstructure resulting from the moving compressive surface load can be seen in Figures 5.15(k)-(o). Compared to the above simulations, additional martensitic plates are formed. These have been triggered by plastic deformations, i.e. deformation-induced martensite is built. When the load has traveled across the surface a complicated microstructure, consisting of martensitic plates of both variants and retained austenite, has been created. These results are in qualitative agreement with experimentally observed structures in metastable austenitic steels.

Focusing on the first time steps, a reason for the formation of the microstruc-

ture is revealed by comparing the crystal plastic simulations with and without the inheritance of the plastic deformation in Figure 5.16. In Figure 5.16(a), the absolute value of the slip is summed up over all slip systems for $t = 6$ ns for the purely crystal plastic simulation. Under the compressive load in vertical direction the slip systems are activated on the left edge of the workpiece, which is thus plastically deformed. Figure 5.16(b) shows, that these plastic deformations lead to a martensitic plate, growing in direction of the plastically deformed region. The continuing evolution can be seen in Figures 5.15(k) -(o). This additional plate does not appear in Figure 5.16(d), where the plastic deformation cannot be inherited to the martensitic phase. In that case the plasticity is wiped out when martensite builds. The plastic deformation is much smaller and hence the additional plate is not induced. The comparison of Figure 5.16(b) and Figure 5.16(d) shows for the same time step a higher martensite content for the purely crystal plastic simulation. The eigenstrain within a plate of martensite causes plastic deformations in the surrounding austenitic matrix. This, in turn, induces martensite leading to the autocatalytic effect, which accelerates the martensitic formation. The lower martensite content in Figure 5.16(d) results from the elimination of the plastic deformation by the martensitic evolution. Analogously, in Figures 5.15(f)-(j) the autocatalytic effect is very small. These observations clearly show that martensite is triggered by the plastic deformation, which is in good agreement with the findings in Olson and Cohen [1972].

Another fact, which is interesting to note in Figure 5.16, concerns the habit plane normal directions. The compressive surface load deforms the specimen inhomogeneously. The habit plane normal directions according to Eq. (3.2) hold for a homogeneously deformed or undeformed specimen. The blue martensite 2 structure in Figure 5.16(d), which is induced in some distance to the applied load where the local deformations are small, forms approximately in accordance with n_{2-}^{ϵ} . The red martensite 1 plate, which is built in the deformed part of the matrix, does not match the indicated habit normal direction n_{1+}^{ϵ} . There is pure austenite below the loaded surface, which contributes, due to its lower stiffness, to a locally higher deformation.

On the other hand, the martensite 1 plate of the purely crystal simulation in Figure 5.16(b) meets the habit plane normal direction. Obviously, the plastically deformed microstructure forms in such a way that in the surroundings of the plate less inhomogeneous deformations occurs. Due to the additional martensite plate, which is indicated with a circle in Figure 5.16(b), the load acts on a composite of both, martensite and austenite. Furthermore, the hardening in the austenite increases its stiffness.

The purely crystal plastic results exhibit another feature in comparison to the above simulations regarding the final equilibrium configuration of the system. For the elastic material behavior in Figures 5.15(a)- (e) and for not considering the

5 An Enhanced Phase Field Model for Martensitic Transformations

inheritance of the plastic deformations in Figures 5.15(f)–(j), the microstructures still evolve after the load is removed. Both finally end up in a purely martensitic matrix, consisting of two bulk phases. In that way the gradient and the separation part of the energy in the phase field potential ψ in Eq. (5.11) are minimal. For the crystal plastic simulation, the microstructure depicted in Figure 5.15(n) does hardly change when the load is removed. This can be seen in Figure 5.17(a) where $E^{\text{grad}} = \int_V \psi^{\text{grad}} dv$ is plotted as a function of simulation time for the three simulations in Figures 5.15(a)–(o). Since ψ^{grad} is a function of the gradient $\nabla\varphi$ of

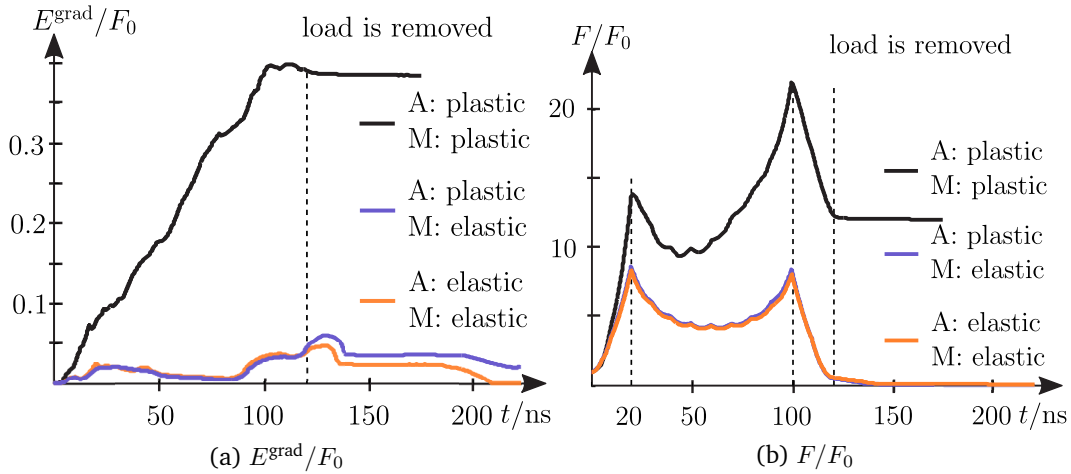


Figure 5.17: Evolution of (a) the global gradient energy E^{grad} and (b) the total global energy F referring to the global energy of the initial configuration F_0 .

the order parameter, E^{grad} is a measure for the interface regions of the system. For the elastic simulation, the evolution of E^{grad} is depicted as an orange line in Figure 5.17(a). Under the applied load the martensitic phase forms and is moving with the surface load. The maximal value of E^{grad} is reached approximately at $t = 130$ ns, in accordance with the martensitic plates appearing in Figure 5.15(d). When the plates vanish, E^{grad} decreases and the microstructure depicted Figure 5.15(j) is formed. While E^{grad} remains temporarily constant at the value related to the two interfaces, the vertical martensite 2 plate narrows. Subsequently, the vertical plate vanishes which leads to a further decrease in E^{grad} until eventually only a single M-M-interface remains (see Figure 5.15(e)).

The results in Figures 5.15(a)–(e) for the elastic simulation (orange curve in Figure 5.17(a)) and the simulation without considering the inheritance of the plastic deformation (purple curve in Figure 5.17(a)) have little differences. Hence, the orange and the purple curve in Figure 5.17(a) are similar. Due to the few plates, which are additionally induced by the plastic deformations in Figures 5.15(f)–(j) the purple curve is in parts slightly above the orange curve. The microstructures keep evolving after the load is removed at $t = 120$ ns and both end up in a purely martensitic workpiece. The additional interface in Figure 5.15(j) compared to Figure 5.15(e) leads to the purple curve lying above the orange curve for $t > 120$ ns.

Only for the black curve, which corresponds to the purely crystal plastic simulation, the interface region increases during the simulation time. The plastic deformations lead to the nucleation of deformation-induced martensite activating the autocatalytic effect. Furthermore, Figure 5.17(a) shows that for this example the plastic deformations accelerate the martensite formation as the black curve increases fast. When the load is removed at $t = 120$ ns, the energy E^{grad} remains constant at a comparably high value since the microstructure consists of several martensitic plates of both martensite variants and retained austenite. The irreversibility of the plastic deformations seems to freeze this microstructure although the global gradient energy E^{grad} remains at a high value.

This draws the attention to the evolution of the global total energy $F = \int \psi \, dv$ of the system which can be seen in Figure 5.17(b). For this example, the gradient energy and the separation energy in the total energy F are small compared to the global elastic energy and the hardening potential. Thus, for all simulations the global total energy is initially increasing, corresponding to the growing load applied at the left edge of the workpiece surface (s_1 in Figure 5.14). The local surface load leads to high deformations. The first peak in F in Figure 5.17(b) arises for $t = 20$ ns, when the sections s_1 and s_2 are fully loaded. For $20 < t < 30$ ns, the load is held constant in the second section s_2 while it is reduced in section s_1 . Thus, the workpiece is less deformed and the total energy F decreases. The second peak in F is obtained for all three curves when the traveling surface load reaches its maximal magnitude at $t = 100$ ns at the right edge of the workpiece, i.e. sections s_9 and s_{10} are fully loaded. When the load is removed at $t = 120$ ns, the global total energy F decreases for the orange and the purple curve, i.e. for the elastic and the plastic simulation without considering the inheritance of the plastic simulation. Both result in a purely martensitic workpiece. This configuration minimizes the separation part and the gradient part of the phase field potential ψ and additionally compensates the eigenstrain on the macro level.

The black curve from the purely crystal plastic simulation evolves in a different way. It initially increases under the applied load. The first peak is reached at a much higher level than for the other two simulations. This is due to the high plastic deformations, which additionally increase the hardening potential. The autocatalytic nucleation of new martensitic plates is accompanied by the transformation-induced eigenstrain, increasing the elastic part of F until the second peak is reached at an even higher level. For $100 < t < 120$ ns, the global total energy decreases with the decreasing load. Yet, when the load is completely removed at $t = 120$ ns, the microstructure and thus the total energy F remain constant. For considering plastic deformations, the moving compressive surface load leads to a complicated microstructure of different martensitic plates of both phases including retained austenite which yields a high value for the global total energy F . Due to the irreversibility of the plastic deformations, this microstructure renders stationary.

5 An Enhanced Phase Field Model for Martensitic Transformations

Compared to the other two simulations, the resulting microstructure of the purely crystal plastic simulation is more realistic for metastable austenitic steels. Thus, plastic deformations, which can be inherited between the phases, play a decisive role in the microstructure evolution.

A Loaded Surface with Fixed Vertical Boundaries

In the previous example the vertical boundaries of the specimen are stress free. However, relating the computation domain to a part of a workpiece which is surrounded by material, motivates a numerical setup where the vertical boundaries are constrained, see Figure 5.18(a) with the load function $q(s_i, t)$ given in Fig-

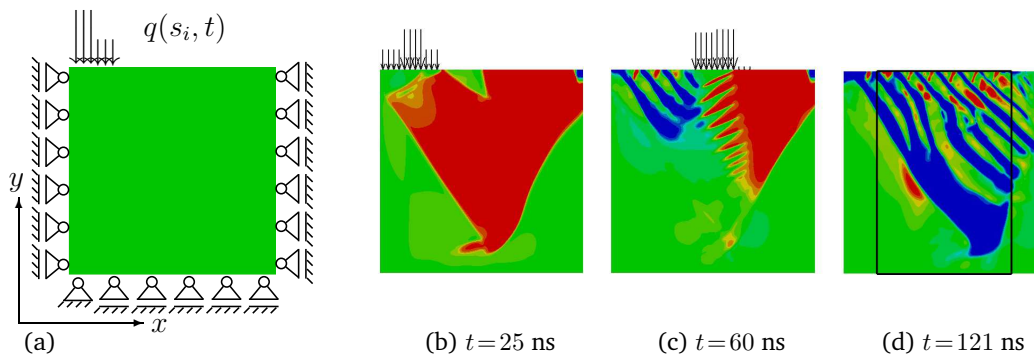


Figure 5.18: Evolution of microstructure (green: austenite, red: martensite 1, blue: martensite 2), magnitude and position of the traveling load indicated by arrows.

ure 5.14. The corresponding simulation results are shown in Figures 5.18(b)-(d). As observed in the above example, martensite 1 is formed under the load, see Figure 5.18(b). However, the fixed vertical boundaries constrain the deformations such that a different microstructure forms. For this example, negative shear stresses arise behind the load, inducing the second variant martensite in the unloaded part of the surface. This is depicted in Figure 5.18(c), where also the autocatalytic effect can be observed. Figure 5.18(d) shows the final microstructure after the load has traveled over the specimen. Compared to the microstructure of the above simulation in Figure 5.15(n), generally less martensite is built since the specimen is less deformed. Mainly variant 2 martensite is formed, where the martensite content decreases with increasing distance to the surface.

The microstructure in Figure 5.18(d) is compared to an experimentally obtained specimen. Aurich et al. [2014] investigate the volume fraction of martensite as a function of depth for a cryogenic turned (feed rate $0.35 \frac{\text{mm}}{\text{rev}}$) austenitic steel (AISI 347) using X-ray diffraction. The resulting values are depicted by the black crosses in Figure 5.19, showing the martensite content with increasing distance to the surface. Starting from the workpiece surface, the volume fraction of α' -martensite of initially 9 % increases with distance to the surface and reaches the maximal value of 37 % below the surface. Subsequently, the volume fraction of

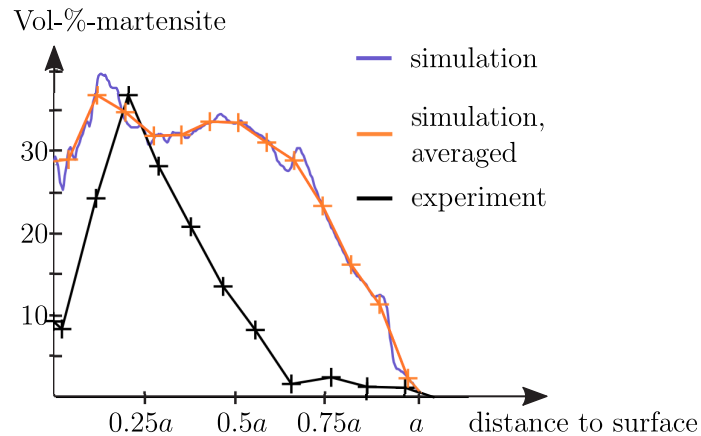


Figure 5.19: Volume fraction of martensite as a function of distance to the surface. Experimental values are taken from Aurich et al. [2014].

martensite decreases with the depth of the workpiece. This is qualitatively in accordance with Figure 5.18(d), where the considered part of the computation domain is indicated with a black box. By this way, the microstructure, which is formed under the influence of the vertical boundaries, is not taken into account. In Figure 5.19 each point of the purple curve results from the sum of both martensite variants of the corresponding row of nodes in the black box in Figure 5.18(d), divided by the number of nodes of a row in the black box. As well as the experimental values, the values of the simulation are additionally averaged height for the orange curve. In accordance with the experimentally obtained curve the martensite content of the simulated structure in Figure 5.18(d) is initially increasing with increasing distance to the workpiece surface. It attains its maximal value below the surface and decreases in the following until the martensite content equals zero in the lower part of the computation domain. Hence, the proposed model captures many features of the martensitic transformation, when plasticity is considered in the discussed way.

Concluding the results concerning a loaded surface, plastic deformations have to be taken into account to model the deformation-induced martensitic transformation. Additionally, the plastic deformations are inherited between the phases. In accordance with results from literature and experimental studies, it is observed that plastic deformations lead to the nucleation of martensite and additionally contribute to the autocatalytic formation of further martensitic plates. In this context, the microstructure, which was obtained by the crystal plastic simulation renders stationary after the load is removed. Furthermore, the results coincide qualitatively with an experimentally obtained structure.

Another feature, which is observed on the microlevel of metastable austenitic steels, are microcracks. Therefore, in the following a damage variable is taken into account.

5.3 A Combined Phase Field Approach for Martensitic Transformations and Damage Evolution

On the microscale of austenitic stainless steel, microcracks are observed, interacting with the phase transformation. In conjunction with damage and fatigue behavior, martensite mainly forms at the crack tip, see e.g. Khan and Ahmed [1996], Stolarz et al. [2001], Nebel and Eifler [2003], Roth et al. [2009], Skorupski et al. [2014]. This influences the crack propagation due to the eigenstrain acting in the martensitic phase. On the other hand, the formation of the martensitic phase is affected by crack growth. To get a deeper insight into these interactions, the model for martensitic transformations is combined with a phase field model for fracture according to Schmitt et al. [2014b]. A short introduction is given on linear elastic fracture mechanics in Section 5.3.1. After the discussion of the model equations in Section 5.3.2, the influence of the crack on the phase transition and vice versa is studied with some numerical examples in Section 5.3.3.

5.3.1 Some Comments on Linear Elastic Fracture Mechanics

Before the combined model for martensitic transformation a damage evolution is introduced, some comments on linear elastic fracture mechanics should be given. A comprehensive textbook on this topic is e.g. Gross and Seelig [2007] while the relevant information referring to the phase field model for brittle fracture, which is applied below, are summarized in Kuhn [2013]. Here only the most important issues are briefly discussed.

Concerning the crack loading, three different modes are defined and illustrated in Figure 5.20. For this work, mode I – corresponding to symmetric crack opening – is used. Mode II and mode III consider sliding and tearing of the crack faces, respectively.

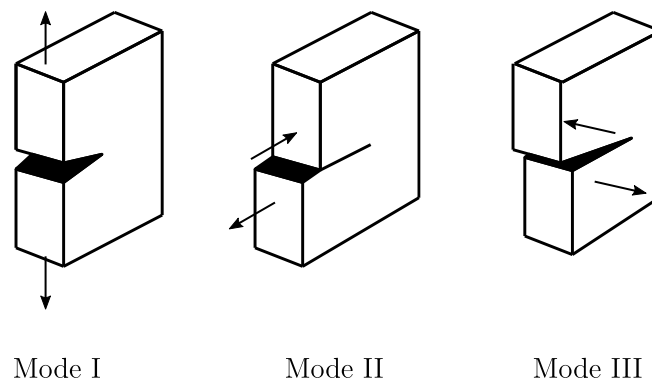


Figure 5.20: Crack opening modes.

5.3 A Combined Phase Field Approach

Close to the *crack tip*, there is the *process zone*, where the irreversible damage takes place. If the process zone is sufficiently small the cracking can be described in the context of continuum mechanics. This applies for metallic materials including metastable austenitic steels. Additionally, linear elastic material behavior is assumed. Inelastic material behavior such as plastic deformations is neglected in this context for the sake of simplicity.

5.3.2 A Combined Phase Field Model

Francfort and Marigo [1998] introduced a continuum fracture model as a variational formulation of brittle fracture, where the total energy is minimized with respect to the crack geometry and the displacement field. The regularized approximation of the model, i.e. a phase field model for fracture, facilitates the numerical implementation. In this regard, phase field models for fracture are introduced e.g. by Bourdin [2007], Bourdin et al. [2008], Kuhn and Müller [2010], Miehe et al. [2010]. An extensive overview on this topic is given in Kuhn [2013]. The consideration of crystalline damage and martensitic transformations is studied in Suiker and Turteltaub [2006]. The authors propose a thermomechanical model, where the volume fractions of the phases and the damaged volume are taken into account. In Garion and Skoczen [2003] the authors use a combined model for phase transformation and damage to examine the evolution of the volume fractions of both, martensite and damage, which are related to the plastic strain at cryogenic temperatures. Xu et al. [2010] apply a combined phase field approach, where a damage variable is coupled with a phase field for ferroelectrics.

In the following, a similar ansatz is used: A combined phase field potential is formulated, which for unbroken material resembles the phase field potential for martensitic transformations in Eq. (5.6). Since the eigenstrain in the martensitic phase induces both, compressive and tensile stresses, the sign of the local volume change is considered and the compressive part is not affected by the crack field, according to Amor et al. [2009], Kuhn and Müller [2009], Kuhn et al. [2013], Schlüter et al. [2014]. An alternative approach, which allows cracks to grow only in tension, is proposed in Hofacker and Miehe [2012], based on a spectral decomposition of the strain tensor ϵ . A further possibility proposed by Strobl and Seelig [2015] takes the direction of the crack into account.

The Combined Phase Field Potential

For the regularization of the energy of fracture, a damage variable s is introduced to describe the crack situation, where $s = 1$ indicates unbroken material, and $s = 0$

5 An Enhanced Phase Field Model for Martensitic Transformations

indicates fracture. The combined phase field energy expression π is given as follows

$$\pi = \underbrace{(s^2 + \varsigma)\psi_s + \psi_{ns}}_{\pi^{\text{bulk}}} + \underbrace{\frac{G_s}{4L_s}(1-s)^2 + G_s L_s |\nabla s|^2}_{\pi^{\text{crack}}}. \quad (5.35)$$

In Eq. (5.35), π consists of two parts, the bulk energy π^{bulk} and the fracture energy π^{crack} . In the bulk energy, ψ_s and ψ_{ns} account for the phase field potential of the undamaged solid subjected to martensitic transformations, where only ψ_s is coupled with the damage variable s . The constant ς with $0 < \varsigma \ll 1$ is introduced to retain a residual stiffness if $s = 0$. Thus, for undamaged material ($s = 1$), the bulk energy π^{bulk} equals the phase field potential for martensitic transformations $\psi = \psi_s + \psi_{ns}$. If there is a crack ($s = 0$), only the residual stiffness ς and the uncoupled part ψ_{ns} remain. The second part of Eq. (5.35) represents the fracture energy π^{crack} , which depends on the damage variable s and its gradient ∇s . Analogously to the model proposed in Chapter 4, the width of the transition zone between undamaged and broken material is controlled by the parameter L_s . The second parameter G_s stands for the crack resistance. Furthermore, the temporal evolution of the damage variable s is assumed to be proportional to the variational derivative of the combined phase field potential π with respect to s , which results in the TDGL

$$\beta_s \dot{s} = -\frac{\delta \pi}{\delta s} = -\left[2s\psi_s - \frac{G_s}{2L_s}(1-s) - 2G_s L_s \Delta s\right], \quad (5.36)$$

where the mobility parameter β_s scales the kinetics of the fracture process. The evolution equation (5.36) allows the damage variable to develop freely such that a crack is able to heal when the load decreases. Therefore, the irreversibility of a crack has to be taken into account by an additional formulation. Here, the rate of the damage variable is enforced to be non-positive, i.e. $\dot{s} \leq 0$, which is proposed e.g. by Miehe et al. [2010].

Modifications of the Phase Field Potential for Martensitic Transformations

In order to couple the phase field potential for martensitic transformations ψ in Eq. (5.6) with the regularized energy of fracture some modifications are necessary. The first point concerns the Landau polynomial $p(\varphi)$ of the separation potential in Eq. (5.1), which has unequal minima: The local minimum $p(\varphi) = 1$ for $\varphi = 0$ (austenite) and the global minima $p(\varphi) = 0$ for $\varphi = \pm 1$ (both martensite variants). This leads to difficulties for the combination with the damage model. Due to its higher separation energy, a crack in the austenitic phase would be more likely than in martensite. Therefore, the separation potential is split into

$$p(\varphi) = d(\varphi) + g(\varphi) \quad (5.37)$$

with

$$d(\varphi) = \frac{\mathcal{G}\varphi^2(1-\varphi^2)^2}{3\Gamma^2-1}, \quad \text{and} \quad g(\varphi) = p(\varphi) - d(\varphi). \quad (5.38)$$

A plot of the three functions can be seen in Figure 5.21. The parameter \mathcal{G} is determined such that the energy barrier Δe_d of $d(\varphi)$ corresponds to Δe_p of $p(\varphi)$ which leads with $\varphi_{\max_p} = \operatorname{argmax}_{\varphi \in [-1,1]} p(\varphi) = \pm\Gamma$ and $\varphi_{\max_d} = \operatorname{argmax}_{\varphi \in [-1,1]} d(\varphi) = \frac{\sqrt{3}}{3}$ to

$$\begin{aligned} \Delta e_p = p(\varphi_{\max_p}) - p(0) &\stackrel{!}{=} \Delta e_d = d(\varphi_{\max_d}) - d(0) \\ \frac{(\Gamma-1)^3}{3\Gamma^2-1} - 1 &= \frac{4\mathcal{G}}{27(3\Gamma^2-1)} - 0 \end{aligned} \quad (5.39)$$

$$\rightsquigarrow \mathcal{G} = \frac{27}{4} \left((\Gamma^2-1)^3 - (3\Gamma^2-1) \right).$$

By introducing the functions $d(\varphi)$ and $g(\varphi)$, the separation potential ψ^{sep} can be written as

$$\psi^{\text{sep}} = \psi_{\text{eq}}^{\text{sep}} + \psi_{\text{diff}}^{\text{sep}} = \kappa_{\text{sep}} \frac{G}{L} d(\varphi) + \kappa_{\text{sep}} \frac{G}{L} g(\varphi), \quad (5.40)$$

where only $\psi_{\text{eq}}^{\text{sep}}$ is coupled with the damage variable.

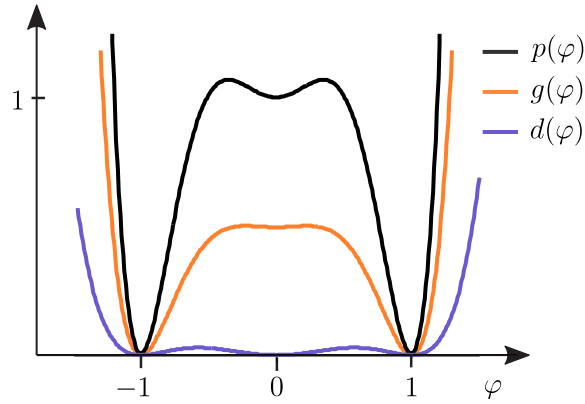


Figure 5.21: Landau polynomial $p(\varphi)$ (black curve) is split into a triple well function $d(\varphi)$ (purple curve) and the function $g(\varphi)$ (orange curve).

The second modification of ψ is related to the elastic energy density W . The martensitic eigenstrain ε^0 , which considers a positive volume change and a lattice shear, leads to both tensile and compressive stresses in the bulk material. In order to achieve realistic fracture behavior in compression, the elastic energy W is split up into a volumetric W^{vol} and a deviatoric part W^{dev} . Thus, the sign of the local volume change can be taken into account according to Amor et al. [2009], Kuhn

5 An Enhanced Phase Field Model for Martensitic Transformations

and Müller [2009], Kuhn et al. [2013], Schlüter et al. [2014],

$$W = W^{\text{vol-}} + W^{\text{vol+}} + W^{\text{dev}}. \quad (5.41)$$

With defining

$$\text{tr}^-(\boldsymbol{\varepsilon} - \boldsymbol{\varepsilon}^0(\varphi)) = \begin{cases} \text{tr}(\boldsymbol{\varepsilon} - \boldsymbol{\varepsilon}^0(\varphi)) & \text{if } \text{tr}(\boldsymbol{\varepsilon} - \boldsymbol{\varepsilon}^0(\varphi)) < 0 \\ 0 & \text{else} \end{cases}, \quad (5.42)$$

$$\text{tr}^+(\boldsymbol{\varepsilon} - \boldsymbol{\varepsilon}^0(\varphi)) = \begin{cases} \text{tr}(\boldsymbol{\varepsilon} - \boldsymbol{\varepsilon}^0(\varphi)) & \text{if } \text{tr}(\boldsymbol{\varepsilon} - \boldsymbol{\varepsilon}^0(\varphi)) \geq 0 \\ 0 & \text{else} \end{cases}, \quad (5.43)$$

the parts of the elastic energy read

$$\begin{aligned} W^{\text{vol-}} &= \frac{\overline{K}(\varphi)}{2} \text{tr}^-(\boldsymbol{\varepsilon} - \boldsymbol{\varepsilon}^0(\varphi))^2, \\ W^{\text{vol+}} &= \frac{\overline{K}(\varphi)}{2} \text{tr}^+(\boldsymbol{\varepsilon} - \boldsymbol{\varepsilon}^0(\varphi))^2 \end{aligned} \quad (5.44)$$

and

$$W^{\text{dev}} = \overline{\mu}(\varphi) [\boldsymbol{e} - \boldsymbol{e}^0(\varphi)] : [\boldsymbol{e} - \boldsymbol{e}^0(\varphi)]. \quad (5.45)$$

In Eq. (5.45), the deviatoric parts of the linearized strain tensor $\boldsymbol{\varepsilon}$ and the eigenstrain tensor $\boldsymbol{\varepsilon}^0$ are adapted for the two-dimensional problem

$$\boldsymbol{e} = \boldsymbol{\varepsilon} - \frac{\text{tr}(\boldsymbol{\varepsilon})}{2} \mathbf{1}, \quad \text{and} \quad \boldsymbol{e}^0(\varphi) = \boldsymbol{\varepsilon}^0(\varphi) - \frac{\text{tr}(\boldsymbol{\varepsilon}^0(\varphi))}{2} \mathbf{1}, \quad (5.46)$$

where $\mathbf{1}$ denotes the two-dimensional identity tensor. For the decomposition of W in Eq. (5.41) isotropic material properties are required. Therefore, starting from the effective Lamé parameters in Eq. (4.79) the effective bulk moduli \overline{K}_A , \overline{K}_M and the effective shear moduli $\overline{\mu}_A$, $\overline{\mu}_M$ of the phases are calculated from $\underline{\mathbb{C}}_A$, $\underline{\mathbb{C}}_M$. Hence, the overall moduli can be written according to Eq. (5.3) in dependence of the order parameter φ

$$\overline{K}(\varphi) = \overline{K}_A + \varphi^2 (\overline{K}_M - \overline{K}_A), \quad \text{and} \quad \overline{\mu}(\varphi) = \overline{\mu}_A + \varphi^2 (\overline{\mu}_M - \overline{\mu}_A). \quad (5.47)$$

With Eqs. (5.40), (5.41), the phase field potential for martensitic transformations ψ can be split up in the following way

$$\begin{aligned} \psi &= \psi_s + \psi_{ns}, \\ \psi_s &= W^{\text{vol+}} + W^{\text{dev}} + \psi_{\text{eq}}^{\text{sep}} + \psi^{\text{grad}}, \\ \psi_{ns} &= W^{\text{vol-}} + \psi_{\text{diff}}^{\text{sep}}. \end{aligned} \quad (5.48)$$

5.3 A Combined Phase Field Approach

In Eq. (5.35), ψ_{ns} is not coupled with the damage variable s . In that way, the elastic energy associated to the negative volume change $W^{\text{vol-}}$ cannot be minimized by creating cracks which leads to asymmetric results in tension and compression. This distinction is necessary since the eigenstrain in martensite leads to compression even if only tensile load is applied. Additionally, the interaction of the unequal minima in $\psi_{\text{diff}}^{\text{sep}}$ with the crack energy π_{crack} is prevented. A coupling of $\psi_{\text{diff}}^{\text{sep}}$ with the damage variable would lead to unphysical results.

Consequently, the evolution equation of the order parameter φ for the combined model is given by the variational derivative of the combined phase field potential π with respect to the order parameter φ , i.e.

$$\begin{aligned}
 \beta \dot{\varphi} &= -\frac{\delta \pi}{\delta \varphi} \\
 &= -(s^2 + \varsigma) \frac{\delta \psi_s}{\delta \varphi} - \frac{\delta \psi_{ns}}{\delta \varphi} \\
 &= -(s^2 + \varsigma) \left[\frac{\partial}{\partial \varphi} (W^{\text{vol+}} + W^{\text{dev}}) + \kappa_{\text{sep}} \frac{G}{L} \frac{\partial d}{\partial \varphi} - \kappa_{\text{grad}} GL \Delta \varphi \right] - \frac{\partial W^{\text{vol-}}}{\partial \varphi} - \kappa_{\text{sep}} \frac{G}{L} \frac{\partial g}{\partial \varphi}.
 \end{aligned} \tag{5.49}$$

Thus, the martensitic phase evolves in dependence of the damage variable s , considering the influence of crack propagation on the martensitic transformation.

Field Equations

The set of field equations of the combined problem is completed by the evolution equation for the damage variable s in Eq. (5.36), the evolution equation for the order parameter φ in Eq. (5.49) and the equilibrium condition in Eq. (4.45). The boundary conditions in Eqs. (4.47)- (4.49) are expanded by the relation for the damage variable s

$$\xi_s^* = 0 \quad \text{on} \quad \partial V \quad \text{with} \quad \xi_s \cdot \mathbf{n} = \xi_s^*. \tag{5.50}$$

The micro stresses ξ_s in Eq. (5.50) are defined according to Section 4.1.2 with

$$\xi_s = \frac{\partial \pi}{\partial \nabla s} = 2 G_s L_s \nabla s.$$

In the equilibrium condition, the Cauchy stress tensor σ is given by consider-

5 An Enhanced Phase Field Model for Martensitic Transformations

ing the combined phase field potential π in the constitutive relation

$$\begin{aligned}\boldsymbol{\sigma} &= \frac{\partial \pi}{\partial \boldsymbol{\varepsilon}} \\ &= \bar{K}(\varphi) \operatorname{tr}^-(\boldsymbol{\varepsilon} - \boldsymbol{\varepsilon}^0(\varphi)) \mathbf{1} + (\varsigma + s^2) \left[\bar{K}(\varphi) \operatorname{tr}^+(\boldsymbol{\varepsilon} - \boldsymbol{\varepsilon}^0(\varphi)) \mathbf{1} + 2\bar{\mu}(\varphi) (\boldsymbol{e} - \boldsymbol{e}^0(\varphi)) \right].\end{aligned}\tag{5.51}$$

As well as in Section 4.2 the coupled system of field equations is solved using finite elements.

Numerical Implementation

The combined phase field model is implemented into the finite element code FEAP where the nodal degrees of freedom are the displacements \boldsymbol{u} , the order parameter φ and the damage variable s . The numerical realization corresponds to the procedure in Section 4.2.2. Thus, here only the additional equations related to the combination with the damage model are discussed.

Starting points are the weak forms of the field equations, where Eq. (4.51) still applies. With the arbitrary test functions $\delta\varphi$ and δs , the weak forms of the evolution equations of the order parameter φ in Eq. (5.49) and the damage variable in Eq. (5.36) read

$$-\int_V \delta\varphi \beta \dot{\varphi} \, dv - \int_V (s^2 + \varsigma) \nabla \delta s \cdot \boldsymbol{\xi} \, dv - \int_V \delta\varphi \frac{\partial \pi}{\partial \varphi} \, dv = 0 \tag{5.52}$$

and

$$-\int_V \delta s \beta_s \dot{s} \, dv - \int_V \nabla \delta s \cdot \boldsymbol{\xi}_s \, dv - \int_V \delta s \frac{\partial \pi}{\partial s} \, dv = 0. \tag{5.53}$$

With the discretization concerning the damage variable s

$$s^h = \sum_{I=1}^{n_{\text{el}}} N_I \hat{s}_I, \quad \underline{\nabla s}^h = \sum_{I=1}^{n_{\text{el}}} \underline{\mathbf{B}}_I^s \hat{s}_I, \quad \text{where } \underline{\mathbf{B}}_I^s = \begin{bmatrix} N_{I,x} \\ N_{I,y} \end{bmatrix}, \tag{5.54}$$

together with Eqs. (4.53), (4.56), (4.58) inserted into the weak forms, the element residuals of node I are deduced to

$$\underline{\mathbf{R}}_{I,e}^u = - \int_{\Omega_e} (\underline{\mathbf{B}}_I^u)^T \underline{\boldsymbol{\sigma}} \, dv, \quad (5.55)$$

$$R_{I,e}^\varphi = - \int_{\Omega_e} N_I \beta \dot{\varphi} \, dv - \int_{\Omega_e} (\underline{\mathbf{B}}_I^\varphi)^T (s^2 + \varsigma) \boldsymbol{\xi} \, dv - \int_{\Omega_e} N_I \frac{\partial \pi}{\partial \varphi} \, dv, \quad (5.56)$$

$$R_{I,e}^s = - \int_{\Omega_e} N_I \beta_s \dot{s} \, dv - \int_{\Omega_e} (\underline{\mathbf{B}}_I^s)^T \boldsymbol{\xi}_s \, dv - \int_{\Omega_e} N_I \frac{\partial \pi}{\partial s} \, dv, \quad (5.57)$$

depending on the nodal degrees of freedom

$$\hat{\mathbf{d}}_J = \begin{bmatrix} \hat{\mathbf{u}}_J \\ \hat{\varphi}_J \\ \hat{s}_J \end{bmatrix}. \quad (5.58)$$

According to Section 4.2.2 the entries of the symmetric element stiffness matrix $\underline{\mathbf{K}}_{I,J,e}$ are given by

$$\underline{\mathbf{K}}_{I,J,e} = - \frac{\partial \underline{\mathbf{R}}_{I,e}}{\partial \hat{\mathbf{d}}_J} = \begin{bmatrix} \underline{\mathbf{K}}_{I,J,e}^{uu} & \underline{\mathbf{K}}_{I,J,e}^{u\varphi} & \underline{\mathbf{K}}_{I,J,e}^{us} \\ \underline{\mathbf{K}}_{I,J,e}^{\varphi u} & \underline{\mathbf{K}}_{I,J,e}^{\varphi\varphi} & \underline{\mathbf{K}}_{I,J,e}^{\varphi s} \\ \underline{\mathbf{K}}_{I,J,e}^{su} & \underline{\mathbf{K}}_{I,J,e}^{s\varphi} & \underline{\mathbf{K}}_{I,J,e}^{ss} \end{bmatrix}. \quad (5.59)$$

With using

$$\begin{aligned} \tilde{\boldsymbol{\sigma}}_s &= \frac{\partial \bar{K}}{\partial \varphi} \text{tr}^- (\boldsymbol{\varepsilon} - \boldsymbol{\varepsilon}^0(\varphi)) \mathbf{1} \\ &+ (\varsigma + s^2) \left[\frac{\partial \bar{K}}{\partial \varphi} \text{tr}^+ (\boldsymbol{\varepsilon} - \boldsymbol{\varepsilon}^0(\varphi)) \mathbf{1} + 2 \frac{\partial \bar{\mu}}{\partial \varphi} (\mathbf{e} - \mathbf{e}^0(\varphi)) \right], \end{aligned} \quad (5.60)$$

$$\begin{aligned} \boldsymbol{\sigma}_s^0 &= \bar{K}(\varphi) \frac{\partial}{\partial \varphi} [\text{tr}^- (\boldsymbol{\varepsilon} - \boldsymbol{\varepsilon}^0(\varphi))] \mathbf{1} \\ &+ (\varsigma + s^2) \left[\bar{K} \frac{\partial}{\partial \varphi} [\text{tr}^+ (\boldsymbol{\varepsilon} - \boldsymbol{\varepsilon}^0(\varphi))] \mathbf{1} + 2 \bar{\mu} \frac{\partial}{\partial \varphi} (\mathbf{e} - \mathbf{e}^0(\varphi)) \right], \end{aligned}$$

5 An Enhanced Phase Field Model for Martensitic Transformations

the entries of $\underline{\mathbf{K}}_{IJ,e}$ read

$$\begin{aligned}
\underline{\mathbf{K}}_{IJ,e}^{uu} &= \int_{\Omega_e} (\underline{\mathbf{B}}_I^u)^T \frac{\partial \boldsymbol{\sigma}}{\partial \underline{\boldsymbol{\varepsilon}}} \underline{\mathbf{B}}_J^u \, dv \\
\underline{\mathbf{K}}_{IJ,e}^{u\varphi} &= \int_{\Omega_e} (\underline{\mathbf{B}}_I^u)^T (\tilde{\boldsymbol{\sigma}}_s + \boldsymbol{\sigma}_s^0) N_J \, dv \\
\underline{\mathbf{K}}_{IJ,e}^{\varphi u} &= \int_{\Omega_e} N_J (\tilde{\boldsymbol{\sigma}}_s + \boldsymbol{\sigma}_s^0) \underline{\mathbf{B}}_I^u \, dv \\
\underline{\mathbf{K}}_{IJ,e}^{us} &= \int_{\Omega_e} (\underline{\mathbf{B}}_I^u)^T \frac{\partial \boldsymbol{\sigma}}{\partial s} N_J \, dv \\
\underline{\mathbf{K}}_{IJ,e}^{su} &= \int_{\Omega_e} N_J \frac{\partial \boldsymbol{\sigma}}{\partial s} \underline{\mathbf{B}}_I^u \, dv \\
\underline{\mathbf{K}}_{IJ,e}^{\varphi\varphi} &= \int_{\Omega_e} (s^2 + \varsigma) \kappa_{\text{grad}GL} (\underline{\mathbf{B}}_I^\varphi)^T \underline{\mathbf{B}}_J^\varphi \, dv + \int_{\Omega_e} N_I \frac{\partial^2 \pi}{\partial \varphi^2} N_J \, dv \\
\underline{\mathbf{K}}_{IJ,e}^{\varphi s} &= \underline{\mathbf{K}}_{IJ,e}^{s\varphi} = \int_{\Omega_e} N_I \frac{\partial}{\partial s} \frac{\partial \pi}{\partial \varphi} N_J + 2s (\underline{\mathbf{B}}_I^s)^T \boldsymbol{\xi} N_J \, dv \\
\underline{\mathbf{K}}_{IJ,e}^{ss} &= \int_{\Omega_e} \left[2G_s L_s (\underline{\mathbf{B}}_I^s)^T \underline{\mathbf{B}}_J^s + N_I \frac{\partial^2 \pi}{\partial s^2} N_J \right] \, dv.
\end{aligned} \tag{5.61}$$

The entries of the element damping matrix $\underline{\mathbf{D}}_{IJ,e}$ are given with

$$\underline{\mathbf{D}}_{IJ,e} = -\frac{\partial \underline{\mathbf{R}}_{IJ,e}}{\partial \hat{\underline{\mathbf{d}}}_J} = \int_{\Omega_e} \begin{bmatrix} 0 & 0 & 0 \\ 0 & \beta N_I N_J & 0 \\ 0 & 0 & \beta_s N_I N_J \end{bmatrix} \, dv. \tag{5.62}$$

The derivatives which are used in Eqs. (5.56)-(5.61) are evaluated in the appendix A.

Also, the irreversibility of cracking is implemented on the element level. As proposed in Kuhn [2013] the constraint $\dot{s} \leq 0$ is enforced numerically

$$\text{if } s_{I,n+1} \leq s_{I,n} \rightarrow s_{I,n+1} := s_{I,n} \tag{5.63}$$

by modifying the element system matrix $\underline{\mathbf{S}}_e$ and the residuals $\underline{\mathbf{R}}_e$ correspondingly.

5.3.3 Numerical Examples

For the numerical realization the mobility constant $\beta = 0.2 \frac{\text{Ns}}{\text{m}^2}$ of the phase field model for martensitic transformation in Eq. (5.36) is slightly reduced in comparison

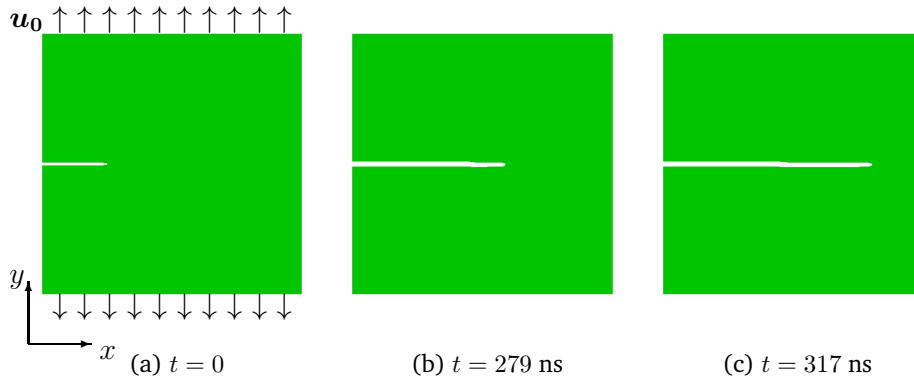


Figure 5.22: (a) Initial configuration: Austenitic (green) specimen with pre-existing crack under mode I loading. (b), (c) Crack formation for an austenitic specimen.

to the previous calculations. This value is one fifth of the mobility constant for damage $\beta_s = 1.0 \frac{\text{Ns}}{\text{m}^2}$, which is, in turn, sufficiently small to model quasi-static crack growth. Hence, the mobility constants β , β_s are chosen such that the phase transformation is five times faster than the crack velocity. Furthermore, for the crack resistance $G_s = 0.2 \frac{\text{J}}{\text{m}^2}$ and for the width of the transition zone between broken and unbroken material $L_s = 5 \text{ nm}$ are taken into account. The initial configuration for the following examples can be seen in Figure 5.22(a): An austenitic specimen with a pre-existing crack under mode I loading.

For comparison, in a first example the martensitic transformation is suppressed by imposing Dirichlet (boundary) conditions $\varphi = 0$ on the order parameter φ in the bulk. The resulting contour plots can be seen in Figures 5.22(b),(c), where in the following elements with $s < 0.1$ are suppressed. Under the applied load the crack starts to grow and propagates straight through the austenitic matrix. This result is expectable since the material of the specimen is homogeneous and the crack tip loading is of mode I type.

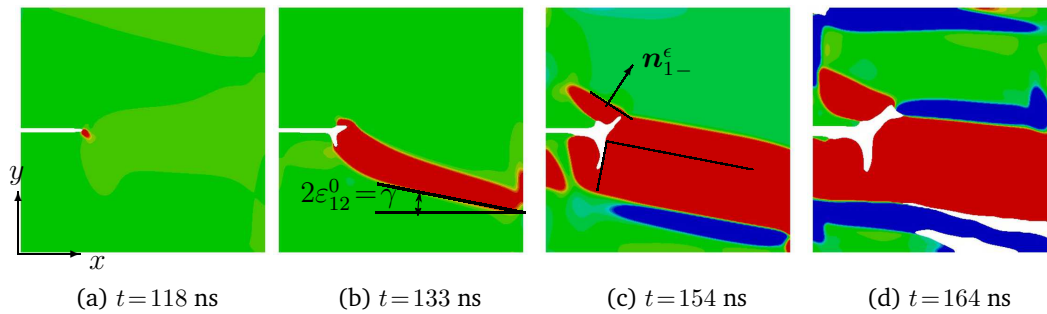


Figure 5.23: Austenitic specimen (green) with pre-existing crack under mode I loading: Evolution of the martensitic phases (martensite 1: red, martensite 2: blue).

Subsequently, an initially austenitic specimen subjected to the martensitic transfor-

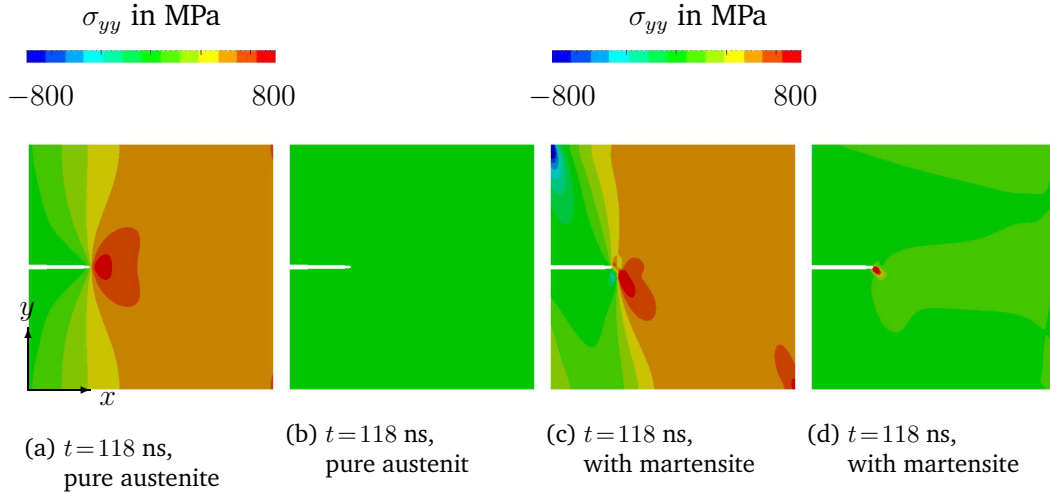


Figure 5.24: (a), (c) Contour plots of σ_{yy} -components. (b), (d) Corresponding microstructure for the austenitic specimen in Figure 5.22 and specimen subjected to phase transformation in Figure 5.23, respectively.

mation is examined. The resulting microstructure is shown in Figures 5.23(a)-(d). Under mode I loading, martensite 1 forms at the crack tip (cf. Figure 5.23(a)), in agreement with experimental studies, e.g. Khan and Ahmed [1996], Roth et al. [2009]. In the following time steps, the martensitic phase grows in a plate-like shape through the matrix, which enables the plate to be sheared according to the eigenstrain. Due to the crack at the left-hand end of the plate this deformation is hardly constrained by the surrounding matrix. Hence, the habit plane normal direction is not in accordance with \mathbf{n}_{1+}^ϵ , \mathbf{n}_{1-}^ϵ because these are calculated for a martensitic inclusion within the austenite. The direction A-M-interface rather meets the shear angle of the eigenshear $\gamma = 2\varepsilon_{12}^0 \approx 11.46^\circ$. This is indicated in Figure 5.23(b).

Concerning the damage process, a different crack pattern is observed compared to the simulation results in Figure 5.22 of the austenitic specimen. Thus, the formation of martensite influences the crack evolution. Figure 5.24(a) and Figure (c) show the distribution of the normal stress component in vertical direction σ_{yy} for both simulations after a few time steps, where tensile stresses are shown in red, compressive stresses in blue. The stress distribution for the purely austenitic specimen in Figure 5.24(a) is expected since high tensile normal stresses in vertical direction arise at the crack tip. However, the eigenstrain within the martensite at the crack tip leads to an asymmetric stress field in Figure 5.24(c). The distribution of high tensile stresses at the crack tip seems to be "sheared" which induces compressive stress in vertical direction at the upper left and tensile stresses in vertical direction at the lower right corner of the specimen. Consequentially, the crack does not propagate straight through the specimen but bifurcates. The lower crack part initially forms at the phase boundary (see Figure 5.23(b)). In experimental studies, cracks propagating along austenite-austenite grain boundaries are reported e.g.

by Stolarz et al. [2001]. For boundary orientations, which deviate strongly from the current crack propagation direction, Stolarz and coworkers find a temporal crack stopping. For this example, the interface between the phases exhibits a strong curvature. However, the expansion of the martensitic phase enables the crack to grow in the martensite without changes in direction. This explains why, the crack does not start to propagate until the martensitic phase has grown to a certain extend. In Figure 5.23(c) the martensitic plate has broadened and the lower crack branch propagates perpendicular to the plate direction. The formation of an additional plate of the first martensitic variant enables the upper crack to grow within martensite. Since this plate evolves within the austenitic phase, the habit plane normal direction n_{1-}^{ϵ} is met, leading to a kink where the two plates join. Furthermore, Figure 5.23(c) shows that the upper crack direction is perpendicular to the additional martensitic plate.

In order to separate the influence of the crack on the phase transformation, in Figure 5.25 the evolution of the phases is shown for a setup where the crack resistance G_s is set to a very high value, which prevents crack growth. In this simulation the crack does not propagate and the additional martensitic plate is not induced. Instead a single continuous martensite 1 plate forms. Thus, the crack influences the phase transformation.

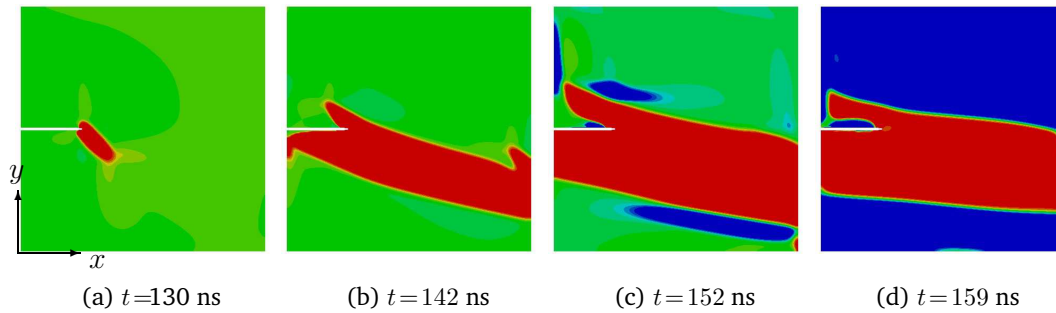


Figure 5.25: Austenitic specimen (green) with pre-existing crack under mode I loading with $G_s \rightarrow \infty$: Evolution of the martensitic phases (martensite 1: red, martensite 2: blue).

Concerning the microstructure evolution in Figure 5.23(c), the second variant builds next to the variant 1 plate. This microstructure reduces the total deformation of the specimen: The variant 1 plate is sheared according to the eigenshear ϵ_{12}^0 , which has a positive sign. This is compensated by the negative sign of ϵ_{12}^0 of the second variant. Some time steps later, in Figure 5.23(d), additional cracks arise in the transition zone of a A-M-interface and a M-M-interface. Considering the phase field potential for martensitic transformations in Eq. (5.35), the contributions of the gradient energy density ψ^{grad} and the separation energy density ψ^{sep} are high in the transition zone. These can be reduced by the crack propagating in the phase

boundary.

In summary, the martensitic formation influences the crack propagation and vice versa. The eigenstrain within the martensite strongly affects the process on the microscale. In the simulation results in Figure 5.23, the cracks appear exclusively in the martensitic phase, partially perpendicular to the plate direction and partially in the transition zones. This coincides with the features of the micrograph in Figure 3.6, which shows cracks arising in martensitic plates in an austenitic matrix; see also enlarged views in Figure 5.26. Thus, the simulation results can be related to experimental observations.

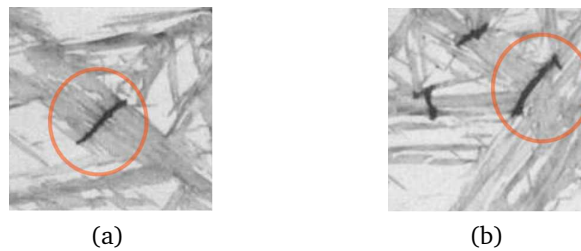


Figure 5.26: Enlarged views of Figure 3.6, Marder et al. [1970]. Cracks arise (a) perpendicular to the plate direction, (b) in the transition zone.

The model contributes to a better understanding of the complicated interactions between the phase transformation and damage. For future work, the implementation of the model with using the Landau polynomial $f(\varphi_1, \varphi_2)$ of Eq. (4.43) could be interesting. The use of $p(\varphi)$, which is considered here, leads to a higher interface energy for a M-M-interface (see Section 5.1). Considering $f(\varphi_1, \varphi_2)$ instead, may lead to different behavior concerning the crack in the M-M-transition zone.

6 Conclusion and Outlook

In order to contribute to a better understanding of the complex interactions, which take place on the microscale of metastable austenitic steels during the manufacturing process of cryogenic turning, a phase field model for martensitic transformations has been developed in this work.

6.1 Conclusion

First, a general approach to calibrate the mobility parameter by using information from atomistic simulation of pure iron was given. This scale transition allows studying the martensitic transformation on a scale, which cannot be accessed by MD simulations. In this context additionally a temperature dependent phase field potential for pure iron was introduced.

With the material properties of metastable austenites taken into account, the consideration of the volumetric eigenstrain and multiple martensitic orientation variants were found to be crucial when modeling the martensitic transformation. The simulations showed the martensite growing in a plate-like shape, which is an important – experimentally observed – feature of the martensitic transformation. Furthermore, the influence of external loads was studied and found it is strongly determined by the eigenstrain within the martensite. In this regard, investigating the habit plane normal directions was a helpful tool. When these are met, the invariant plane strain condition is satisfied.

In the second part of this thesis the elastic phase field model was enhanced by a crystal plasticity scheme and by a damage variable, increasing the computational effort. Hence, another numerically more efficient possibility to consider two martensite variants with a single order parameter was introduced. However, since the single order parameter leads to higher interface energy, the comparison of both approaches revealed different results for M-M-interfaces. Nevertheless, the computational savings are significant. Therefore, this approach was applied for the enhanced model in a first step.

By considering a crystal plasticity scheme within the phase field model, plastic deformations could be taken into account which dissipate additional energy and thus influence the martensitic transformation. The numerical simulations confirmed that the phase transformation causes slip. Also, martensite was triggered by plastic

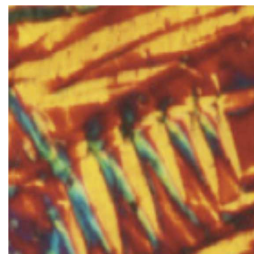
6 Conclusion and Outlook

deformations. Motivated by the turning process, the phase transformation in a crystal plastic material was studied at a loaded surface. In this context it was found that the plastic deformations are inherited from austenite to the martensite. In accordance with results from literature and experimental studies it was observed that the plastic deformations lead to an autocatalytic formation of martensitic plates. After the loading process the workpiece had a complicated microstructure, consisting of martensitic plates of both variants and retained austenite, which rendered stationary after the loading process. Furthermore, the results qualitatively and quantitatively coincided with an experimentally obtained structure.

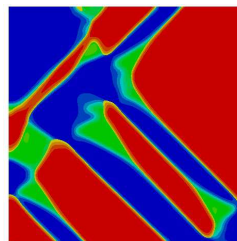
Finally, the model for martensitic transformations was combined with a phase field model for fracture, which revealed a strong influence of a crack on the phase transformation and vice versa. In accordance with the previous results the process was affected by the eigenstrain in the martensite. The features of the resulting microstructure coincided with a micrograph where the cracks arise only within the martensite – either between the plates or perpendicular to the plate direction.

Generally, the phase field model for martensitic transformations is a useful tool to understand the interacting mechanisms which take place on the microscale of metastable austenitic steels since the model reflects the physics. In summary,

- it could be understood that the *twinned plates of martensite* form in order to minimize the total deformation;

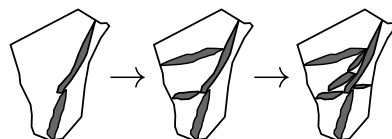


(a) Bhadeshia [2015]

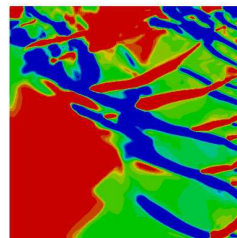


(b) Simulation results,
Chapter 4

- the *autocatalytic effect* could be related to plastic deformations;

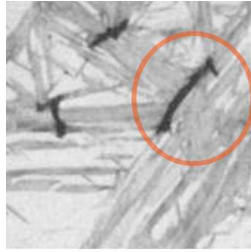


(c) Schematic representation
of the autocatalytic effect

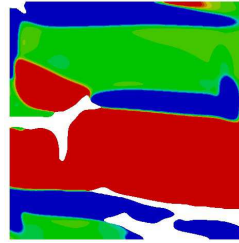


(d) Simulation results,
Section 5.2

- concerning the *interactions with microcracks* the model reflects the experimentally observed features.



(e) Marder et al. [1970]

(f) Simulation results,
Section 5.3

6.2 Outlook

For future work, the consideration of further alloying elements for the MD simulations would enable the approximation of the material parameters of steel. Furthermore, starting from the temperature dependent phase field potential, which was derived in this work, the temperature could be considered as an additional degree of freedom within the finite element scheme. Therefore, the system of coupled field equations is extended by the heat equation. This approach allows studying the influence of the temperature on the phase transition, e.g. the cooling during the cryogenic turning.

Concerning the evolution of the martensitic phase, an extension to three dimensions would provide additional insights. The limitation to two dimensions restricts the nucleation and the propagation of martensite. Moreover, three dimensional numerical results facilitate the verification with experiments. Yet, the larger computational effort should be compensated by more efficient numerical strategies, e.g. by a GPU accelerated implementation.

Since plastic deformations play a decisive role for the phase transformation the correlations between these two phenomena should be part of future work. So far, the coupling between phase transformation and plasticity is considered only through the stresses. In this regard, the interactions through the kinetics should be investigated as well.

Eventually, for the combined model, a closer look on the model parameter G_s , which stands for the crack resistance, could be beneficial. Until now, for both phases the same crack resistance is taken into account. For future work, experimentally obtained values might be used for each phase.

6 *Conclusion and Outlook*

Appendix

A Derivatives Concerning the Numerical Implementation of the Damage Model

Appendix A: Derivatives Concerning the Numerical Implementation

In the following, the derivatives which are used in Eqs. (5.56)-(5.61) are evaluated. With

$$\begin{aligned} \tilde{W} &= (s^2 + \varsigma) \left[\frac{\partial \bar{K}}{\partial \varphi} \text{tr}^+ (\boldsymbol{\varepsilon} - \boldsymbol{\varepsilon}^0(\varphi))^2 + 2 \frac{\partial \bar{\mu}}{\partial \varphi} (\mathbf{e} - \mathbf{e}^0(\varphi)) : (\mathbf{e} - \mathbf{e}^0(\varphi)) \right] \\ &\quad + \frac{\partial \bar{K}}{\partial \varphi} \text{tr}^- (\boldsymbol{\varepsilon} - \boldsymbol{\varepsilon}^0(\varphi))^2, \\ W^0 &= (s^2 + \varsigma) \left[\bar{K} \frac{\partial}{\partial \varphi} [\text{tr}^+ (\boldsymbol{\varepsilon} - \boldsymbol{\varepsilon}^0(\varphi))]^2 + 2 \bar{\mu} \frac{\partial}{\partial \varphi} (\mathbf{e} - \mathbf{e}^0(\varphi)) : (\mathbf{e} - \mathbf{e}^0(\varphi)) \right] \\ &\quad + \bar{K} \frac{\partial}{\partial \varphi} [\text{tr}^- (\boldsymbol{\varepsilon} - \boldsymbol{\varepsilon}^0(\varphi))]^2, \end{aligned} \tag{A.1}$$

$$\begin{aligned} \tilde{W}_\varphi &= (s^2 + \varsigma) \left[\frac{\partial \bar{K}}{\partial \varphi} \text{tr}^+ (\boldsymbol{\varepsilon} - \boldsymbol{\varepsilon}^0(\varphi)) \frac{\partial}{\partial \varphi} (\text{tr}^+ (\boldsymbol{\varepsilon} - \boldsymbol{\varepsilon}^0(\varphi))) \right. \\ &\quad \left. + 2 \frac{\partial \bar{\mu}}{\partial \varphi} (\mathbf{e} - \mathbf{e}^0(\varphi)) : \frac{\partial}{\partial \varphi} (\mathbf{e} - \mathbf{e}^0(\varphi)) \right] \\ &\quad + \frac{\partial \bar{K}}{\partial \varphi} \text{tr}^- (\boldsymbol{\varepsilon} - \boldsymbol{\varepsilon}^0(\varphi)) \frac{\partial}{\partial \varphi} (\text{tr}^- (\boldsymbol{\varepsilon} - \boldsymbol{\varepsilon}^0(\varphi))), \\ W_\varphi^0 &= (s^2 + \varsigma) \left[\bar{K} \left[\frac{\partial}{\partial \varphi} (\text{tr}^+ (\boldsymbol{\varepsilon} - \boldsymbol{\varepsilon}^0(\varphi))) \right]^2 + 2 \bar{\mu} \frac{\partial}{\partial \varphi} (\mathbf{e} - \mathbf{e}^0(\varphi)) : (\mathbf{e} - \mathbf{e}^0(\varphi)) \right] \\ &\quad + \bar{K} \left[\frac{\partial}{\partial \varphi} \text{tr}^- (\boldsymbol{\varepsilon} - \boldsymbol{\varepsilon}^0(\varphi)) \right]^2 \end{aligned} \tag{A.2}$$

the derivatives are given with

$$\frac{\partial^2 \pi}{\partial \varphi^2} \approx \kappa_{\text{sep}} \frac{G}{L} \left((s^2 + \varsigma) \frac{\partial^2 d}{\partial \varphi^2} + \frac{\partial^2 g}{\partial \varphi^2} \right) + 2 \tilde{W}_\varphi + W_\varphi^0 \tag{A.3}$$

$$\frac{\partial \pi}{\partial \varphi} = \kappa_{\text{sep}} \frac{G}{L} \left((s^2 + \varsigma) \frac{\partial d}{\partial \varphi} + \frac{\partial g}{\partial \varphi} \right) + \frac{1}{2} \tilde{W} + W^0 \tag{A.4}$$

$$\frac{\partial}{\partial s} \frac{\partial \pi}{\partial \varphi} = \left(\frac{1}{2} \frac{\partial \tilde{W}}{\partial s} + \frac{\partial W^0}{\partial s} \right) + 2s \kappa_{\text{sep}} \frac{G}{L} \frac{\partial d}{\partial \varphi} \tag{A.5}$$

$$\frac{\partial \pi}{\partial s} = 2s\psi^s - \frac{G_s}{2L_s} (1 - s) \tag{A.6}$$

$$\frac{\partial^2 \pi}{\partial s^2} = 2\psi^s + \frac{G_s}{2L_s} \tag{A.7}$$

$$\frac{\partial \boldsymbol{\sigma}}{\partial s} = 2s \left[\bar{K}(\varphi) \text{tr}^+ (\boldsymbol{\varepsilon} - \boldsymbol{\varepsilon}^0) + 2\mu(\mathbf{e} - \mathbf{e}^0) \right] \tag{A.8}$$

Appendix A: Derivatives Concerning the Numerical Implementation

For the evaluation of $\frac{\partial^2 \pi}{\partial \varphi^2}$ in Eq. (A.3) the second order derivatives $\frac{\partial^2}{\partial \varphi^2} \epsilon^0(\varphi)$, $\frac{\partial^2}{\partial \varphi^2} \bar{K}(\varphi)$, $\frac{\partial^2}{\partial \varphi^2} \bar{\mu}(\varphi)$ are negligibly small.

Appendix A: Derivatives Concerning the Numerical Implementation

Bibliography

- R Ahluwalia, T Lookman, A Saxena, and R. C Albers. Landau theory for shape memory polycrystals. *Acta Materialia*, 52:209–218, 2004.
- J. Altenbach and H. Altenbach. *Einführung in die Kontinuumsmechanik*. B. G. Teubner Stuttgart, 1994.
- H. Amor, J.-J. Marigo, and C. Maurini. Regularized formulation of the variational brittle fracture with unilateral contact: numerical experiments. *J. Mech. Phys. Solids*, 57:1209–1229, 2009.
- A. Artemev, Y. Wang, and A. G. Khachaturyan. Three-dimensional phase field model and simulation of martensitic transformation in multilayer systems under applied stresses. *Acta Materialia*, 48:2503–2518, 2000.
- A. Artemev, Y. Jin, and A.G. Khachaturyan. Three-dimensional phase field model of proper martensitic transformation. *Acta Materialia*, 49(7):1165 – 1177, 2001.
- J. C. Aurich, P. Mayer, B. Kirsch, D. Eifler, M. Smaga, and R. Skorupski. Characterization of deformation induced surface hardening during cryogenic turning of aisi 347. *CIRP Annals - Manufacturing Technology*, 63:65–68, 2014.
- E. C. Bain. The nature of martensite. *Transactions of the Metallurgical Society of AIME*, 70:25–46, 1924.
- T. Bartel and K. Hackl. A novel approach to the modelling of single-crystalline materials undergoing martensitic phase-transformations. *Material Science and Engineering A*, 481-482:371–375, 2008.
- T. Bartel, A. Menzel, and B. Svendsen. Thermodynamic and relaxation-based modelling of the interaction between martensitic phase transformations and plasticity. *Journal of Mechanics and Physics of Solids*, 59:1004–1019, 2011.
- W. Becker and D. Gross. *Mechanik elastischer Körper und Strukturen*. Springer Verlag, 2002.
- H. K. D. H. Bhadeshia. Interpretation of the microstructure of steels, 2015. URL http://cml.postech.ac.kr/2008/Steel_Microstructure/SM2.html.
- K. Bhattacharya. *Microstructure of martensite*. Oxford University Press, 2003.

Bibliography

- B. Bourdin. Numerical implementation of the variational formulation for quasi-static brittle fracture. *Interfaces Free Boundaries*, 9:411–430 DOI: 10.4171/IFB/171411–430, 2007.
- B. Bourdin, G.A. Francfort, and J.-J. Marigo. The variational approach to fracture. *Journal of Elasticity*, 91:5–148, 2008.
- J. S. Bowles and J. K. Mackenzie. The crystallography of martensite transformations i. *Acta Metallurgica*, 2(1):129 – 137, 1954.
- J. W. Cahn and J. E. Hilliard. Free energy of a nonuniform system. i. interfacial free energy. *The Journal of Chemical Physics*, 28:258–267, 1958.
- L.-Q. Chen, Y. Wang, and A. G. Khachaturyan. Kinetics of tweed and twin formation during an ordering transition in a substitutional solid solution. *Philosophical Magazine Letters*, 65:15–23, 1992.
- M. Cherkaoui and M. Berveiller. Micromechanical modeling of the martensitic transformation induced plasticity in steels. *Smart Mater. Struct.*, 9:592–603, 2000.
- M. Cherkaoui, M. Berveiller, and H. Sabar. Micromechanical modeling of martensitic transformation induced plasticity (triple) in austenitic single crystals. *International Journal of Plasticity*, 14:597–626, 1998.
- M. Cohen, G. B. Olson, and P. C. Clapp. On the classification of displacive phase transformations. *Proceedings of the International Conference on Martensitic Transformations ICOMAT*, 1979.
- B. Coleman and W. Noll. The thermodynamics of elastic materials with heat conduction and viscosity. *Archive for Rational Mechanics and Analysis*, 13(1):167–178, 1963.
- B. D. Coleman and M. E. Gurtin. Thermodynamics with internal state variables. *The Journal of Chemical Physics*, 2(47):597–613, 1967.
- J. D. Eshelby. The force on an elastic singularity. *Phil. Trans. Roy. Soc. Lond. A*, 877(244):87–112, 1951.
- J. D. Eshelby. The determination of the elastic field of an ellipsoidal inclusion, and related problems. *Proceedings of the Royal Society of London A: Mathematical, Physical and Engineering Sciences*, 241(1226):376–396, 1957.
- F. D. Fischer, M. Berveiller, K. Tanaka, and E. R. Oberaigner. Continuum mechanical aspects of phase transformations in solids. *Archive of Applied Mechanics*, 64:54–85, 1994.
- G.A. Francfort and J.-J. Marigo. Revisiting brittle fracture as an energy minimization problem. *J Mech Phys Solids*, 46:1319–1342, 1998.

- E. Fried and M. E. Gurtin. Continuum theory of thermally induced phase transitions based on an order parameter. *Physica D: Nonlinear Phenomena*, 68(3-4):326 – 343, 1993.
- E. Fried and M.E. Gurtin. Dynamic solid-solid transitions with phase characterized by an order parameter. *Physica D: Nonlinear Phenomena*, 72(4):287 – 308, 1994.
- C. Garion and B. Skoczen. Combined model of strain-induced phase transformation and orthotropic damage in ductile materials at cryogenic temperatures. *International Journal of Damage Mechanics*, 12:331–356, 2003.
- D. Gross and T. Seelig. *Bruchmechanik : Mit einer Einführung in die Mikromechanik*. Springer Berlin Heidelberg, 2007.
- E. A. Guggenheim. *Thermodynamics : an advanced treatment for chemists and physicists*. North-Holland Publishing Company Amsterdam, 1967.
- X. H. Guo, S.-Q. Shi, and X. Q. Ma. Elastoplastic phase field model for microstructure evolution. *Applied Physics Letters*, 87:221910, 2005.
- M. E. Gurtin. Generalized ginzburg-landau and cahn-hilliard equations based on a microforce balance. *Physica D: Nonlinear Phenomena*, 92(3-4):178 – 192, 1996.
- M. E. Gurtin, E. Fried, and L. Anand. *The Mechanics and Thermodynamics of Continua*. Cambridge University Press, 2010.
- M.E. Gurtin. *Configurational Forces as Basic Concepts of Continuum Physics*. Applied Mathematical Sciences. Springer, 2000.
- P. Haupt. *Continuum Mechanics and Theory of Materials*. Springer, 2002.
- F. Hildebrand and C. Miehe. A regularized sharp interface model for phase transformation accounting for prescribed sharp interface kinetics. *Proc. Appl. Math. Mech.*, 10:673–676, 2010.
- F. Hildebrand and C. Miehe. Variational phase field modeling of laminate deformation microstructure in finite gradient crystal plasticity. *Proceedings in Applied Mathematics and Mechanics*, 12:37–40, 2012.
- F. E. Hildebrand. *Variational Multifield Modeling of the Formation and Evolution of Laminate Microstructure*. PhD thesis, Fakultät Bau- und Umweltingenieurwissenschaften der Universität Stuttgart and Stuttgart Research Center for Simulation Technology, 2013.
- F. E. Hildebrand and C. Miehe. Comparison of two bulk energy approaches for the phasefield modeling of two-variant martensitic laminate microstructure. *Technische Mechanik*, 32:3–20, 2011.

Bibliography

- M. Hofacker and C. Miehe. Continuum phase field modeling of dynamic fracture: variational principles and staggered fe implementation. *International Journal of Fracture*, 178:113–129, 2012.
- G. A. Holzapfel. *Nonlinear Solid Mechanics : A Continuum Approach for Engineering*. John Wiley & Sons, 2000.
- S.Y. Hu and L.Q. Chen. A phase-field model for evolving microstructures with strong elastic inhomogeneity. *Acta Materialia*, 49(11):1879 – 1890, 2001.
- T. J. R. Hughes. *The Finite Element Method: Linear Static and Dynamic Finite Element Analysis*. Dover Civil and Mechanical Engineering. Dover Publications, 2000.
- Y. M. Jin, A. Artemev, and A. G. Khachaturyan. Three-dimensional phase field model of low-symmetry martensitic transformation in polycrystal: simulation of ζ'_2 -martensite in auctd alloys. *Acta Materialia*, 49:2309–2320, 2001.
- M.F. Kanninen. *Inelastic behavior of solids*. Materials Science and Engineering Series. McGraw-Hill, 1970.
- A.G. Khachaturyan. *Theory of Structural Transformations in Solids*. Dover Books on Engineering Series. Dover Publications, 2008.
- Z. Khan and M. Ahmed. Stress-induced martensitic transformation in metastable austenitic stainless steels: Effect on fatigue crack growth rate. *Journal of Materials Engineering and Performance*, 5(2):201–208, 1996.
- R. Kienzler and G. Herrmann. *Mechanics in Material Space: With Applications to Defect and Fracture Mechanics*. Engineering online library. Springer Berlin Heidelberg, 2000.
- KTH Stockholm, May 2015. URL <http://www.met.kth.se/ia>. The Image Archive.
- C. Kuhn. *Numerical and analytical investigation of a phase field model for fracture*. PhD thesis, Technische Universität Kaiserslautern, 2013.
- C. Kuhn and R. Müller. Phase field simulation of thermomechanical fracture. *Proceedings in Applied Mathematics and Mechanics*, 9:191–192, 2009.
- C. Kuhn and R. Müller. A continuum phase field model for fracture. *Engineering Fracture Mechanics*, 77:3625–3634, 2010.
- C. Kuhn, A. Schlüter, and R. Müller. A phase field approach for dynamic fracture. *Proceedings in Applied Mathematics and Mechanics*, 13:87–88, 2013.
- A. Kundin, D. Raabe, and H. Emmerich. A phase-field model for incoherent martensitic transformations including plastic accommodation process in the austenite. *Journal of Mechanics and Physics in Solids*, 59:2082–2102, 2011.

- H.M. Ledbetter. Monocrystal elastic constants in the ultrasonic study of welds. *Ultrasonics*, 23(1):9 – 13, 1985.
- V. I. Levitas, D.-W. Lee, and D. L. Preston. Interface propagation and microstructure evolution in phase field models of stress-induced martensitic phase transformations. *International Journal of Plasticity*, 26:395–422, 2010.
- V. I. Levitas, A. R. Roy, and D. L. Preston. Multiple twinning and variant-variant transformations in martensite: Phase-field approach. *Physical Review B*, 88:054113, 2013.
- J. Lubliner. *Plasticity Theory*. Dover books on engineering. Dover Publications, 2008.
- A. Malik, G. Amberg, A. Borgenstam, and J. Ågren. Phase-field modelling of martensitic transformation: the effects of grain and twin boundaries. *Modelling and Simulation in Materials Science and Engineering*, 21(8):085003, 2013.
- M. Mamivand, M. A. Zaeem, and H. El Kadiri. A review on phase field modeling of martensitic phase transformation. *Computational Materials Science*, 77(0):304 – 311, 2013.
- A.R. Marder, A.O. Bense, and G. Krauss. Microcracking sensitivity in fe-c plate martensite. *Metallurgical Transactions*, 1(6):1545–1549, 1970.
- H. Margenau and G. M. Murphy. *Die Mathematik für Physik und Chemie*. Verlag Harri Deutsch, 1965.
- G. B. McFadden, A. A. Wheeler, R. J. Braun, S. R. Coriell, and R. F. Sekerka. Phase-field models for anisotropic interfaces. *Phys. Rev. E*, 48:2016–2024, Sep 1993.
- C. Miehe, F. Welschinger, and M. Hofacker. Thermodynamically consistent phase-field models of fracture: Variational principles and multi-field fe implementations. *International Journal for Numerical Methods in Engineering*, 83(10):1273–1311, 2010. ISSN 1097-0207.
- N. Moelans, B. Blanpain, and P. Wollants. An introduction to phase-field modeling of microstructure evolution. *Computer Coupling of Phase Diagrams and Thermochemistry*, 32:268–294, 2008.
- R. Müller. Configurational forces in defect mechanics and in computational methods. Technische Universität Darmstadt, Institut für Mechanik, 2005. Habilitation thesis.
- T. Nebel and D. Eifler. Cyclic deformation behaviour of austenitic steels at ambient and elevated temperatures. *Sadhana*, 28:187–208, 2003.
- G. B. Olson and M. Cohen. A mechanism for strain-induced nucleation of martensitic transformations. *Journal of the Less-Common Metals*, 28:107–118, 1972.

Bibliography

- G. B. Olson and M. Cohen. A general mechanism of martensitic nucleation: Part ii. general concepts of the fcc \rightarrow bcc and other martensitic transformations. *Metalurgical Transactions A*, 7A:1905–1914, 1976.
- E. Pereloma and D. V. Edmonds, editors. *Phase Transformations in Steels*. Woodhead Publishing Series in Metals and Surface Engineering. Woodhead Publishing, 2012.
- A. Pimpinelli and J. Villain. *Physics of Crystal Growth*. Cambridge University Press, 1998.
- D. A. Porter and K. E. Easterling. *Phase Transformations in Metals and Alloys*. Chapman & Hall, 1992.
- G. Reisner, E.A. Werner, and F.D. Fischer. Micromechanical modeling of martensitic transformation in random microstructures. *International Journal of Solids and Structures*, 35(19):2457 – 2473, 1998.
- A. W. Richards, R. A. Lebensohn, and K. Bhattacharya. Interplay of martensitic phase transformation and plastic slip in polycrystal. *Acta Materialia*, 61:4384–4397, 2013.
- P. R. Rios and J. R. C. Guimarães. Formal analysis of isothermal martensite spread. *Materials Research*, 11:103 – 108, 03 2008.
- I. Roth, U. Krupp, H. J. Christ, M. Kübbeler, and C.-P. Fritzen. Deformation induced martensite formation in metastable austenitic steel during in situ fatigue loading in a scanning electron microscope. *ESOMAT*, 2009. Article Number 06030.
- F. Roumi. *Shape Changing Transformations: Interactions with Plasticity and Electrochemical Processes*. PhD thesis, California Institute of Technology, Pasadena, California, 2010.
- A. Schlüter, A. Willenbücher, C. Kuhn, and R. Müller. Phase field approximation of dynamic brittle fracture. *Computational Mechanics*, 54(5):1141–1161, 2014.
- S. Schmidt. A temperature dependent potential of a phase field model for martensitic transformations. Technische Universität Kaiserslautern, Lehrstuhl für Technische Mechanik, 2015. Studienarbeit.
- R. Schmitt, R. Müller, and C. Kuhn. A phase field model for martensitic transformations. *Proc. Appl. Math. Mech.*, 12(1):261–262, 2012.
- R. Schmitt, R. Müller, C. Kuhn, and H. M. Urbassek. A phase field approach for multivariant martensitic transformations of stable and metastable phases. *Archive of Applied Mechanics*, 83:849–859, 2013a.
- R. Schmitt, R. Müller, R. Skorupski, M. Smaga, and D. Eifler. A phase field approach for martensitic transformations in elastoplastic materials. *Proc. Appl. Math. Mech.*, 13:213–214, 2013b.

- R. Schmitt, B. Wang, H. M. Urbassek, and R. Müller. Modeling of martensitic transformations in pure iron by a phase field approach using information from atomistic simulation. *Technische Mechanik*, 33:119–130, 2013c.
- R. Schmitt, C. Kuhn, R. Müller, and K. Bhattacharya. Crystal plasticity and martensitic transformations - a phase field approach. *Technische Mechanik*, 34:23–38, 2014a.
- R. Schmitt, C. Kuhn, R. Skorupski, M. Smaga, D. Eifler, and R. Müller. A combined phase field approach for martensitic transformations and damage. *Archive of Applied Mechanics*, pages 1–10, 2014b.
- R. Schmitt, P. Mayer, B. Kirsch, J. Aurich, C. Kuhn, R. Müller, and K. Bhattacharya. A phase field approach for martensitic transformations and crystal plasticity. *PAMM*, 14(1):383–384, 2014c.
- R. Schmitt, C. Kuhn, and R. Müller. On a phase field approach for martensitic transformations in a crystal plastic material at a loaded surface. *Continuum Mechanics and Thermodynamics*, pages 1–12, 2015. doi: 10.1007/s00161-015-0446-1.
- D. Schrade, B. X. Xu, R. Müller, and D. Gross. On phase field modeling of ferroelectrics: parameter identification and verification. *SMASIS*, 1:299–306, 2008.
- D. Schrade, R. Müller, and D. Gross. Parameter identification in phase field models for ferroelectrics. *Proc. Appl. Math. Mech.*, 9:369–370, 2009.
- D. Schrade, R. Müller, and D. Gross. On the physical interpretation of material parameters in phase field models for ferroelectrics. *Archive of Applied Mechanics*, 83:1393–1413, 2013.
- J. Schröder and C. Miehe. Aspects of computational rate-independent crystal plasticity. *Computational Material Science*, 9:168–176, 1997.
- J. C. Simo and T. J. R. Hughes. *Computational Inelasticity*. Springer-Verlag, New-York, 1998.
- R. Skorupski, M. Smaga, D. Eifler, R. Schmitt, and R. Müller. Influence of morphology of deformation induced α' -martensite on stress-strain response in a two phase austenitic-martensitic-steel. *Key Engineering Materials*, 592-593:582–585, 2014.
- J. Stolarz, N. Baffie, and T. Magnin. Fatigue short crack behaviour in metastable austenitic stainless steels with different grain sizes. *Materials Science & Engineering A*, 319-321:521–526, 2001.
- M. Strobl and T. Seelig. A novel treatment of crack boundary conditions in phase field models of fracture. *PAMM*, submitted 2015.

Bibliography

- A. J. S. Suiker and S. Turteltaub. Crystalline damage development during martensitic transformations. In *ECOMAS CFD*, 2006.
- I. Tamura. Deformation-induced martensitic transformation and transformation-induced plasticity in steels. *Metal Science*, 16:245–253, 1982.
- R. L. Taylor. FEAP - finite element analysis program, 2014. URL <http://www.ce.berkeley/feap>.
- B. Wang and H. M. Urbassek. Phase transitions in an fe system containing a bcc/fcc phase boundary: An atomistic study. *Phys. Rev. B*, 87:104108, 2013.
- Y. Wang and A. G. Khachaturyan. Three-dimensional field model and computer modeling of martensitic transformations. *Acta Materialia*, 2:759–773, 1997.
- Y. Wang and A. G. Khachaturyan. Multi-scale phase field approach to martensitic transformations. *Materials Science and Engineering: A*, 438-440:55 – 63, 2006. Proceedings of the International Conference on Martensitic Transformations.
- M. S. Wechsler, D. S. Lieberman, and T. A. Read. On the theory of the formation of martensite. *Journal of Metals*, November:1503–1515, 1953.
- P. Wriggers. *Nichtlineare Finite-Element-Methoden*. Springer Berlin Heidelberg, 2001.
- B.-X. Xu, D. Schrade, D. Gross, and R. Mueller. Fracture simulation of ferroelectrics based on the phase field continuum and a damage variable. *International Journal of Fracture*, 166:163–172, 2010.
- T. Yalcinkaya. *Microstructure evolution in crystal plasticity: strain path effects and dislocation slip patterning*. PhD thesis, Eindhoven University of Technology, 2011.
- A. Yamanaka, T. Takaki, and Y. Tomita. Elastoplastic phase-field simulation of self- and plastic accommodations in cubic \rightarrow tetragonal martensitic transformation. *Material Science and Engineering A*, 491:378–384, 2008.
- A. Yamanaka, T. Takaki, Y. Tomita, and M. Yoshino. Crystal plasticity phase-field simulation of deformation behavior and microstructure evolution in polycrystalline material. *Proceedings of X International Conference on Computational Plasticity - COMPLAS X*, 2009.
- H. K. Yeddu, A. Malik, J. Ågren, G. Amberg, and A. Borgenstam. Three-dimensional phase-field modeling of martensitic microstructure evolution in steels. *Acta Materialia*, 60(4):1538 – 1547, 2012.
- M.-X. Zhang and P. M. Kelly. Crystallographic features of phase transformations in solids. *Progress in Materials Science*, 54(8):1101 – 1170, 2009.

Bibliography

- W. Zhang, Y. M. Jin, and A. G. Khachaturyan. Phase field microelasticity modeling of heterogeneous nucleation and growth in martensitic alloys. *Acta Materialia*, 55:565–574, 2007.
- Y. Zhong and T. Zhu. Phase-field modeling of martensitic microstructure in NiTi shape memory alloys. *Acta Materialia*, 75:337 – 347, 2014.
- O. C. Zienkiewicz and R. L. Taylor. *The Finite Element Method: The Basis*. Refereex Engineering. Butterworth-Heinemann, 2000.

Curriculum Vitae

Name: Regina Ulrike Müller (geb. Schmitt)

Nationalität: deutsch

10.2005 – 05.2011 Studium Maschinenbau und Verfahrenstechnik
Technische Universität Kaiserslautern

Diplomarbeit:
*Finite Element Implementation of a
Model for Antarctic Ice Shelves*

Abschluss: Diplom

05.2011 – 09.2015 Wissenschaftliche Mitarbeiterin,
Lehrstuhl für Technische Mechanik
Fachbereich Maschinenbau und Verfahrenstechnik
Technische Universität Kaiserslautern